Universität Hamburg
DER FORSCHUNG | DER LEHRE | DER BILDUNG

A phase microscope for ultra-cold quantum gases

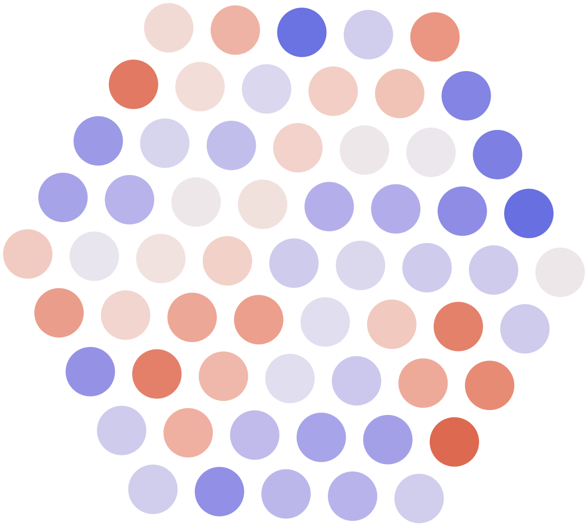

Dissertation zur Erlangung des Doktorgrades
an der Fakultät für Mathematik, Informatik und Naturwissenschaften
Fachbereich Physik der Universität Hamburg

vorgelegt von
Justus Christopher Brüggenjürgen
aus Hannover

Hamburg
2024

Gutachter

Gutachter der Dissertation:	Prof. Dr. Henning Moritz Prof. Dr. Christof Weitenberg
Zusammensetzung der Prüfungskomission:	Prof. Dr. Henning Moritz Prof. Dr. Christof Weitenberg Prof. Dr. Klaus Sengstock Prof. Dr. Ludwig Mathey Prof. Dr. Roman Schnabel
Vorsitzender der Prüfungskommission:	Prof. Dr. Roman Schnabel
Datum der Disputation:	19.12.2024
Vorsitzender Fach-Promotionsausschuss PHYSIK:	Prof. Dr. Markus Drescher
Leiter des Fachbereichs PHYSIK:	Prof. Dr. Markus Drescher
Dekan der Fakultät MIN:	Prof. Dr.-Ing. Norbert Ritter

Eidesstattliche Versicherung

Hiermit versichere ich an Eides statt, die vorliegende Dissertationsschrift selbst verfasst und keine anderen als die angegebenen Hilfsmittel und Quellen benutzt zu haben.

Sofern im Zuge der Erstellung der vorliegenden Dissertationsschrift generative Künstliche Intelligenz (gKI) basierte elektronische Hilfsmittel verwendet wurden, versichere ich, dass meine eigene Leistung im Vordergrund stand und dass eine vollständige Dokumentation aller verwendeten Hilfsmittel gemäß der Guten wissenschaftlichen Praxis vorliegt. Ich trage die Verantwortung für eventuell durch die gKI generierte fehlerhafte oder verzerrte Inhalte, fehlerhafte Referenzen, Verstöße gegen das Datenschutz- und Urheberrecht oder Plagiate.

Ort, Datum	Justus C. Brüggenjürgen

Ich versichere, dass dieses gebundene Exemplar der Dissertation und das in elektronischer Form eingereichte Dissertationsexemplar (über den Docata-Upload) und das bei der Fakultät (zuständiges Studienbüro bzw. Promotionsbüro Physik) zur Archivierung eingereichte gedruckte gebundene Exemplar der Dissertationsschrift identisch sind.

Ort, Datum	Justus C. Brüggenjürgen

Abstract

Coherence properties play a central role in quantum systems and are fundamental to phenomena such as superfluidity and superconductivity. Ultracold gases in optical lattices provide an versatile platform for quantum simulation, allowing precise control to explore coherence properties that underlie complex quantum phenomena.

In this thesis, we investigate the coherence properties of an ultra cold Bose gas in a two-dimensional optical lattice, focusing on phase coherence and fluctuations across the Berezinskii-Kosterlitz-Thouless (BKT) phase transition. We utilize matter-wave microscopy with an optical matter-wave lens to magnify the atomic wavefunction, enabling us to image the density distribution with single-site resolution. The ability to turn off interaction allows us to measure a coherent wavefunction released from a lattice. This reveals the two-dimensional Talbot effect, where the periodic density modulations from the lattice is self-imaged and we capture in-situ images of these periodic revivals. The strength of the revivals are a direct measure for the spatial coherence of the system. Furthermore, we present the implementation of a phase microscope for ultra cold quantum gases. The phase microscope enables us to extract the relative phases on single lattice sites. We measure the phase correlation towards the BKT phase transition and obtain a critical exponent for the algebraic decay in our system. The matter-wave and phase microscopy techniques presented here offer an approach towards exploring coherence in strongly correlated quantum systems, providing full spatial resolution and potential insights into phase transitions and novel quantum phases.

Zusammenfassung

Kohärenzeigenschaften spielen eine zentrale Rolle in Quantensystemen und sind grundlegend für Phänomene wie Supraleitung und Suprafluidität. Ultrakalte Gase in optischen Gittern bieten eine vielseitige Plattform für die Quantensimulation, die präzise Kontrolle ermöglicht, um die Kohärenzeigenschaften komplexer Quantenphänomene zu untersuchen.

In dieser Dissertation untersuchen wir die Kohärenzeigenschaften eines ultrakalten Bose-Gases in einem zweidimensionalen optischen Gitter, wobei der Schwerpunkt auf Phasenkohärenz und -fluktuationen über den Berezinskii-Kosterlitz-Thouless (BKT)-Phasenübergang hinweg liegt. Wir nutzen Materiewellenmikroskopie mit einer optischen Materiewellenlinse, um die atomare Wellenfunktion zu vergrößern, was uns die Abbildung der Dichteverteilung mit Einzelplatzauflösung ermöglicht. Die Fähigkeit, Wechselwirkungen abzuschalten, erlaubt uns die Messung einer kohärenten Wellenfunktion, die aus dem Gitter freigesetzt wird. Dies offenbart den zweidimensionalen Talbot-Effekt, bei dem die periodischen Dichtemodulationen des Gitters sich selbst abbilden und wir in-situ-Bilder dieser periodischen Revivals erfassen können. Die Stärke dieser Revivals liefert eine direkte Messung der räumlichen Kohärenz des Systems. Darüber hinaus stellen wir die Implementierung eines Phasenmikroskops für ultrakalte Quantengase vor. Das Phasenmikroskop ermöglicht es uns, die relativen Phasen auf einzelnen Gitterplätzen zu extrahieren. Wir messen die Phasenkorrelation unterhalb des BKT-Phasenübergangs und bestimmen einen kritischen Exponenten für den algebraischen Zerfall in unserem System. Die hier vorgestellten Techniken der Materiewellen- und Phasenmikroskopie bieten einen Ansatz zur Untersuchung der Kohärenz in stark korrelierten Quantensystemen und ermöglichen vollständige räumliche Auflösung sowie potenzielle Einblicke in Phasenübergänge und neue Quantenzustände.

Publications

During this thesis we published the following paper:

[1] J. C. Brüggenjürgen, M. S. Fischer, and C. Weitenberg. "A phase microscope for quantum gases". In: *arXiv* (2024). eprint: `2410.10611`.

Contents

CHAPTER 1

Introduction

Quantum simulation is by now a well-established concept since Richard Feynman proposed his idea to utilize nature's intrinsic principles to tackle quantum mechanical problems[1]. Today, we can distinguish between two types of quantum simulators: digital simulators, commonly known as quantum computers, and analog simulators, which replicate Hamiltonians directly. With a quantum simulator, it is possible to gain insights into observables that are challenging or inaccessible in the system of interest. Additionally, novel systems can be engineered, further expanding the scope of physical inquiry.

Quantum simulation is possible on various platforms where high control of the system and direct measurement of observables are achieved. One such platform involves cold atoms[2]. Cold atoms have become an ideal platform for both analog and digital quantum simulations.

With the first Bose-Einstein condensate of cold atoms[3], the platform was established in quantum simulation. From here, the toolbox of cold atoms was expanded, from bulk physics to lattice physics emulating solid-state physics to tweezer systems enabling quantum computing with cold atoms. Besides preparing quantum systems, various tools have been developed for probing their properties. The primary method of measurement involves capturing light emitted or absorbed by the atoms. Absorption imaging allows to probe the system's density on a macroscopic scale and with a free expansion prior to imaging, the momentum distribution is detected.

The goal to measure the density and the dynamics of the system on a microscopic scale was achieved with the advent of quantum gas microscopes, for bosons[4, 5] and fermions[6–11]. Quantum gas microscopes enable imaging and manipulating single atoms with a resolution of a single lattice site[12]. This allowed, for example, the microscopic observation of the superfluid-to-Mott insulator transition in the Bose-Hubbard model[13]. With fine potential engineering, major advances were possible towards the suspected d-wave superconducting phase in the Fermi-Hubbard model, e.g. the observation of the anti-ferromagnet[14]. The addition of spin-resolution enabled the detection of spin dynamics[15–19]. Recent measurements extended the capabilities to the detection of additional observables like the current between lattice sites[20].

Quantum gas microscopy relies on high-resolution optics, which are demanding to implement. Recent advances with matter-wave optics allowed the quantum wave function to be expanded prior to imaging[21–23], allowing imaging at resolutions below the lattice spacing and making matter-wave microscopy an essential complement to traditional quantum gas microscopy.

Matter-wave microscopy enhances resolution and introduces new opportunities to measure coherence in quantum systems. The coherence properties of ultra-cold atomic gases were first shown in [24], where two BECs overlapped and showed interference fringes. In lattice experiments, the coherence between lattice sites is a common tool for observing the lattice in momentum space[25]. Coherent waves passing through a lattice exhibit the Talbot effect[26], which is well known in optics, but also in matter-waves[27–31].

The interference between two-dimensional Bose gases was utilized to probe the Berezinskii-Kosterlitz-Thouless (BKT) phase transition. Although true long-range order is forbidden in two-dimensional systems (Mermin-Wagner theorem), interference remains observable[32]. The BKT theory[33, 34] describes the existence of quasi long-range order, which, eventually, as temperature is increased, will vanish due to the unbinding of vortex-anti-vortex pairs. The BKT phase transition is highly intriguing for quantum simulation, as it is closely connected to two-dimensional superfluidity[35].

In this thesis, we extend the toolbox for quantum simulation with quantum gases. We introduce matter-wave microscopy with an optical potential enabling us to measure a coherent wavefunction. With the system still coherent, we are able to observe the two-dimensional matter-wave Talbot effect in situ for the first time. We use the Talbot effect to probe the coherence properties of the system across the BKT phase transition. Finally, we present the phase microscope, resolving the increasing phase fluctuations towards the BKT transition with single-site resolution. With this new tool, we are able to extract the correlation between lattice sites and obtain a critical exponent of the algebraic decay.

1.1 | Thesis Outline

The thesis is structured in the following manner:

In chapter 2, I give an overview of the ^{7}Li quantum gas machine we finished building during this thesis. I recapitulate shortly the relevant atomic properties of ^{7}Li. The setup and the cooling stages are presented. The chapter concludes with measurements characterizing the evaporation process into degeneracy.

In chapter 3, I present the versatile lattice setup. I highlight the static and dynamical configurations possible, which include a static triangular lattice, an averaged optical potential used for evaporation and matter-wave magnification, a multi-frequency setup allowing for fast dynamical change of geometry and moving lattices. The core parts of the setup are the combination of a double-pass AOM and an EOM on each path.

In chapter 4, I introduce our implementation of matter-wave microscope based on the optical potential created by the dipole trap configuration of the versatile lattice setup. We use matter-wave microscopy to measure the matter-wave Talbot effect as well as the optical Talbot effect arising from the diffraction of coherent light on the magnified lattice. With the matter-wave Talbot effect, we measure the coherence of the system across the BKT phase transition and determining the correlation length.

In chapter 5, I present the phase microscope. I give a short recap of BKT physics in quantum gases and bring our system of tubes into context. I discuss the aberrations present in the optical matter-wave lens created by Gaussian beams. Analytical estimates for the accumulated phase over a quarter period oscillation in the anharmonic potential are discussed and I back them with numerical simulations. This results in a conversion factor from density deviation in respect to a mean distribution on a single lattice site to the phase on a single lattice site. With this conversion, I present measurements of magnified in-situ images from which the phase can be extracted on a single lattice site. The conversion factor is determined via phase thermometry. I close with the extraction of the phase correlations, from which we obtain the exponent of the algebraic decay below the phase transition.

The results in chapter 4 and chapter 5 are published in [23] and figures in these chapters are closely adapted. The work leading to the presented results in this thesis has been performed in close collaboration with Mathis Fischer, whose thesis gives a detailed account of the experimental setup, and under supervision of Christof Weitenberg.

CHAPTER 2

Lithium quantum gas machine

This chapter provides an overview of the experimental setup and methods used to achieve Bose-Einstein condensation with Lithium-7 atoms, focusing on laser cooling and evaporative techniques. A detailed accord on our preparation of Bose-Einstein condensates with Lithium-7 and its relevant properties can be found in the thesis of Mathis Fischer [36]. Our experimental setup employs a compact design with an oven placed below a two-dimensional magneto-optical trap (2D-MOT) followed by a three-dimensional MOT (3D-MOT) for laser cooling. Following the laser-cooling stage, we employ a magnetic trap for initial evaporative cooling, transitioning to an optical dipole trap for the final evaporation. The scattering length is tuned via a Feshbach resonance allowing for fast rethermalization with strong interactions.

2.1 | Lithium-7

Lithium is the lightest alkali atom, excluding hydrogen, and this property gives it intriguing potential for quantum simulation. Both isotopes, fermionic ^{6}Li and bosonic ^{7}Li, are stable and have favorable scattering properties. Laser-cooling and degeneracy has been achieved for the bosonic and fermionic isotope[37, 38]. Our main motivation to work with ^{7}Li is to study the coherence properties of Bose-Einstein condensates (BECs) with the aid of a matter-wave microscopy [21, 23]. The matter-wave microscope enables us to probe the system down to the single-site level. By switching off the contact interaction during magnification of the wavefunction, we can probe the coherence of the system with the same spatial resolution. ^{7}Li as well as ^{6}Li feature a broad Feshbach resonance aiding the control over interactions. In figure 2.1 both the intra- and inter-spin resonances of ^{7}Li are plotted for the singlet-states of the 2S$_{1/2}$, $F = 1$ [39, 40]. The triplet, $F = 2$, manifold doesn't exhibit any Feshbach resonances to our knowledge. The scattering lengthas a function of the magnetic field in the vicinity of a Feshbach resonance is described by the following relation:

$$a(B) = a_{BG}\left(1 - \frac{\Delta B}{B - B_0}\right), \tag{2.1}$$

where a_{BG} is the background scattering length at $|B - B_0| \gg \Delta B$, B_0 is the location of the Feshbach resonance and ΔB is the width of the resonance. For the singlet state, the scattering length at zero magnetic field is $a(0) = 33(2)a_0$ and for the triplet state it is $a(0) = -27.6(5)a_0$ [41]. The scattering lengths are given in Bohr radii $a_0 = 5.29 \times 10^{-11}\,\mathrm{m}$. The intra-spin resonance for the hyperfine state

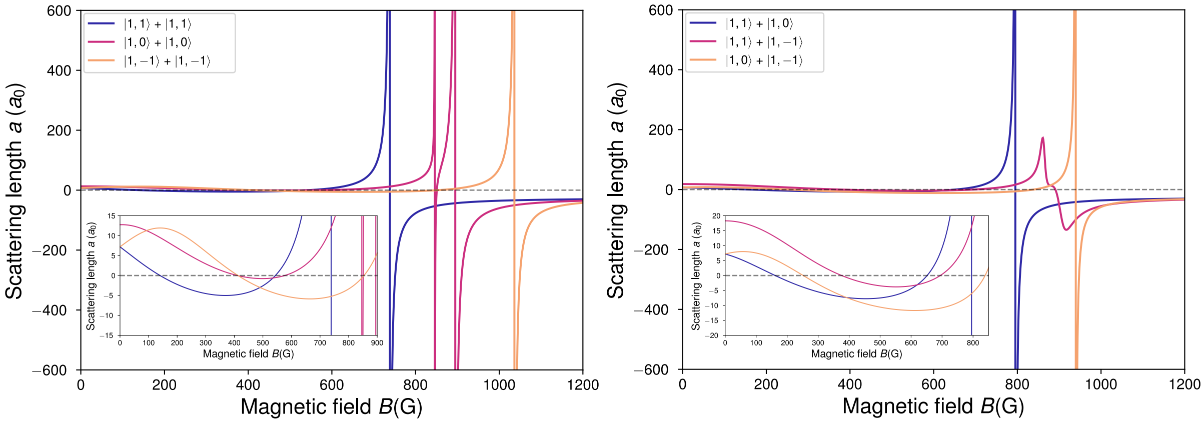

Figure 2.1: Feshbach resonances of ^{7}Li. The left panel shows the intra-species resonances; in this work, we use the resonance of the $(1,1)$ state (blue). The inset shows a zoom too visualize the zero-crossing of the scattering length, which we use to turn of the interactions. The right panel shows the inter-species resonances with the respective inset as on the left. The data were provided by Randy Hulet [40].

$F = 1$, $m_F = 1$ (referred to as the (1,1) state) lies at $B_0 = 738.3\,\mathrm{G}$ with a width of $\Delta B = 194.7\,\mathrm{G}$. In contrast to general description of the Feshbach resonance above, the intra-spin scattering length of (1,1) dips below zero for values $B < B_0$ before it reaches the background scattering length of the singlet-state. The zero-crossing closer to the resonance lies at $543.6\,\mathrm{G}$, which will allow us to turn off the interaction almost entirely.

The two most important transitions for laser cooling in Lithium, as well as other alkali atoms, are the so-called D1- and D2-transitions. For ^{7}Li these are the transition from 2 ^{2}S$_{1/2}$ to 2 ^{2}P$_{1/2}$ and 2 ^{2}P$_{3/2}$, respectively. The level scheme is shown in 2.2 with the relevant wavelengths used in the experiment. For both isotopes, the transitions are spaced by $10.5\,\mathrm{GHz}$. The transitions are resonantly driven with wavelengths $\lambda_{D1} = 670.977\,\mathrm{nm}$ and $\lambda_{D2} = 670.962\,\mathrm{nm}$. Both transitions have a natural linewidth of $\Gamma = 2\pi \times 5.87\,\mathrm{MHz}$. The D2-transition is used for initial cooling with magneto-optical traps and for imaging the atoms. On the D1-transition, we perform a Λ-enhanced gray-molasses cooling scheme and optically pump the atoms into the (2,2)-state. The ground state 2 ^{2}S$_{1/2}$ hyperfine splitting is $803.5\,\mathrm{MHz}$.

As our particles are Bosons, this allows for three-body scattering events. These events can result in high kinetic energies which will cause the atoms to heat up and/or leave the trap. For ^{7}Li the three-body loss rate is exceptionally high. With $1 \times 10^{-27}\,\mathrm{cm}^6/\mathrm{s}$ [42] it is orders of magnitudes larger than in Rubidium, $4.3 \times 10^{-29}\,\mathrm{cm}^6/\mathrm{s}$ [43], or Sodium, $1.1 \times 10^{-30}\,\mathrm{cm}^6/\mathrm{s}$ [44]. The three-body collision rate also has to be compared to the elastic two-body collision rate, which drives the rethermalization of the system. The two-body collision rate can be tuned via the Feshbach resonance, but the three-body collision rate also increases with the two-body scattering length, see [39, 40]. The high three-body loss complicates the evaporation process for ^{7}Li, but does not render it unfeasible.

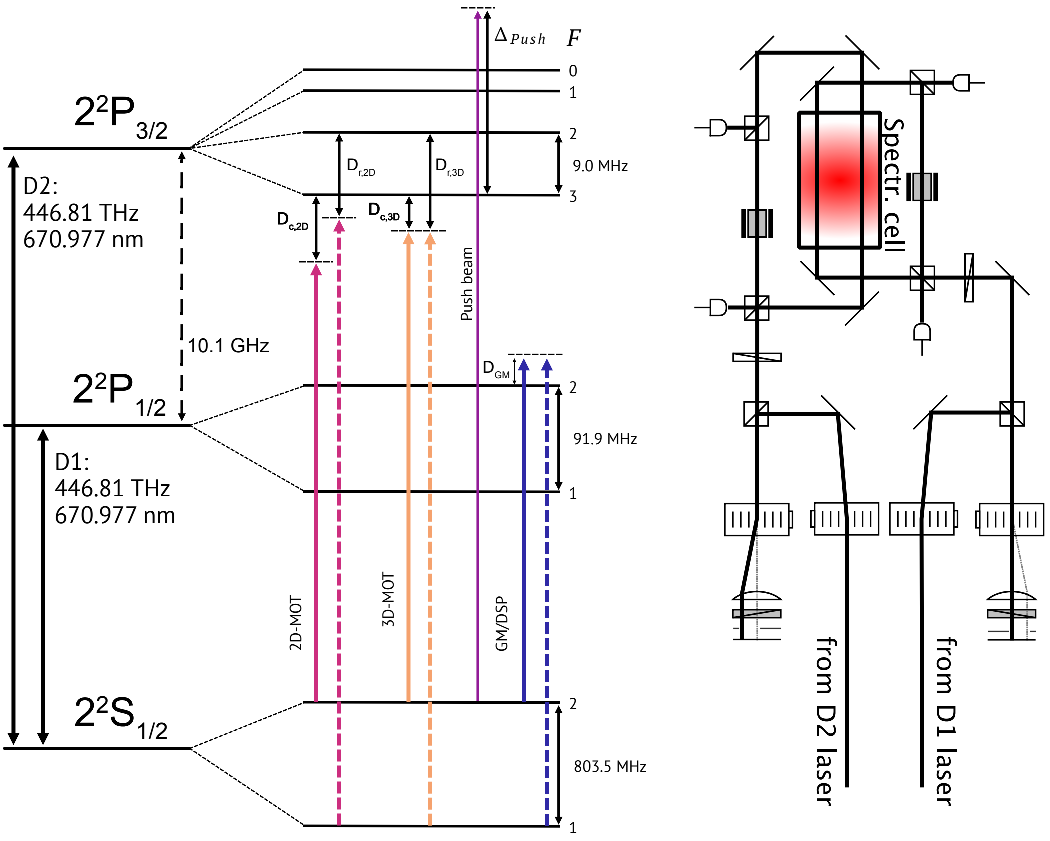

Figure 2.2: Level diagram, Feshbach resonances and spectroscopy setup. (Left) Energy level diagram of ^{7}Li. The red and orange lines show the transitions to the D2 line for the 2D and 3D MOTs, with the 'cooler' from $F = 2$ as solid lines and the 'repumper' from $F = 1$ as dashed lines. In blue, the transition to the D1-line, used for gray molasses and optical pumping, is shown (solid and dashed as before). The purple line represents the transition for the push-beam, which is blue-detuned to the D2-line. (Middle) Feshbach resonances of ^{7}Li. The top panel shows the intra-species resonances; in this work, we use the resonance of the $(1, 1)$ state (blue). The lower panel shows the inter-species resonances. (Right) Sketch of the spectroscopy setup. The setup enables laser locking to the respective transition and allows the choice between two different spectroscopy methods, FMS and MTS. Spectroscopy of the fermionic isotope is also possible by switching the double-pass AOM configuration. (Figure adapted from [36].)

2.2 | Experimental apparatus

Vacuum chamber Ultra-cold quantum gas experiments are only possible in well-controlled environments. One key part of this is an ultra-high vacuum. Any collision with background gases reduces the lifetime of the quantum gas, thereby limiting both the experimental possibilities and the accuracy of the results. The chamber's compact design allows for short cycle times, which are essential for modern quantum gas experiments (Fig. 2.3). More details about the design of the vacuum chamber can be found in previous theses [36, 45, 46]. The chamber is separated into two parts by a differential pumping tube to maintain ultra-high vacuum necessary for state-of-the-art quantum gas experiments in the science region. The science region (also referred to as the 3D-MOT region) exhibits pressures down to $1 \times 10^{-11}\,\mathrm{mbar}$. Values below $1 \times 10^{-11}\,\mathrm{mbar}$ cannot be measured with the installed probes. The loading region (also referred to as the 2D-MOT region), which contains a Lithium evaporating oven, has a pressure on the order of $1 \times 10^{-10}\,\mathrm{mbar}$. In the loading region, we prepare an initially hot gas of Lithium atoms with a simple oven design and capture the atoms with a 2D-MOT. In this setup, there is no line-of-sight from the oven to the ultra-cold cloud, as would be the case in a setup using a Zeeman slower. With a Zeeman slower, additional atom transport would be necessary. On the high-pressure side, a glass cell is attached to the stainless-steel chamber. The glass cell provides high optical access and is broadband coated for the wavelengths used in the experiment, as well as for potential future wavelengths [47]. The small diameter of $26\,\mathrm{mm}$ makes high-NA imaging possible, which would allow for quantum gas microscopy[4, 5]. In the glass cell, all further cooling mechanisms are implemented. The experiments with the ultra-cold quantum gas are performed at the same location as all cooling mechanism besides the 2D-MOT. This allows for high repetition rates, as (almost) no further transport is needed.

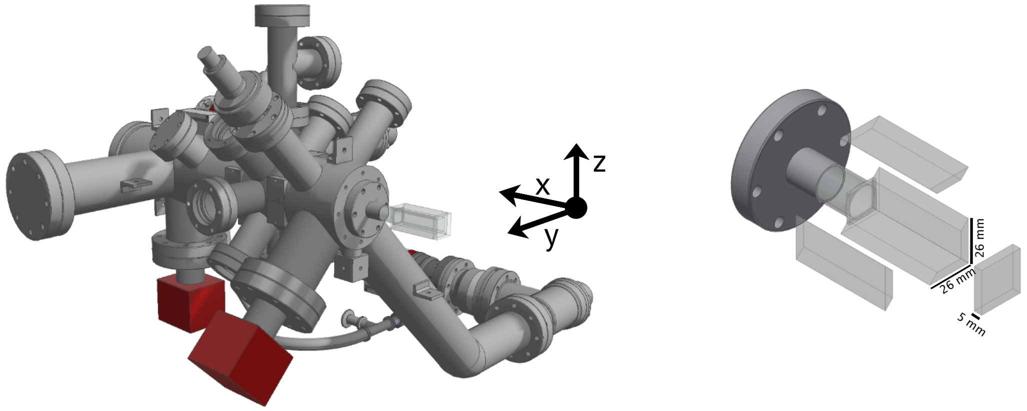

Figure 2.3: Vacuum setup of the lithium machine.. (Left) CAD drawing of the vacuum chamber used in the experiment. The chamber is designed to enable loading a 2D-MOT in high vacuum and to perform quantum simulation in ultra-high vacuum within the glass cell. Initial evacuation is performed by a pre-pump (detached after closing the connecting valve) and turbo pumps (barely visible in the back). The red cubes represent ion-getter pumps, which maintain the ultra-high vacuum. The pressure is monitored with gauges (one visible in the front up-going arm). (Right) Exploded view of the glass cell. The thickness and extent of the glass cell allow for high-resolution microscopy. (Drawings adapted from [36].)

Laser setups The laser setups for cooling, trapping and manipulating the atoms are all fiber-coupled and prepared on the same and a separate optical table. On the second table, all near-resonant light is prepared, e.g., the MOT light and imaging light. For the near-resonant light, we use a combination of external cavity diode lasers (ECDL) and tapered amplifiers to provide enough power. Two of the lasers are locked to a lithium spectroscopy. The overlap of the ^{6}Li D2-line and the ^{7}Li D1-line creates a double feature in the Doppler-free spectroscopy. We lock the D1 light to the more prominent ^{6}Li D2-line feature. For light on the D2-line, we use the respective feature. For both ^{6}Li and ^{7}Li D2-lines, we lock the lasers to the crossover between the two hyperfine ground states. We use two types of Doppler-free spectroscopy. For the D1 light, we use frequency modulation spectroscopy (FMS) and for the D2-line, we use modulation transfer spectroscopy (MTS). A third laser is offset-locked to the D2 laser within a range of $\Delta = \pm 2\,\mathrm{GHz}$. This enables us to image the atoms in distinct states and at particular magnetic fields. Besides ensuring the correct frequency by spectroscopy, we use single- and double-pass acousto-optical modulators (AOMs) as well as electro-optical modulators (EOMs) to shift the frequency of the light to the desired values. Additionally, AOMs are used to switch the light on and off in time-critical cases. For less critical timings we use mechanical shutters to ensure complete blocking of the light path. Preparation also includes beam shaping, directing and splitting/combining. We use lenses, (polarizing) beam splitters, half and quarter waveplates and mirrors extensively to create the needed output. Finally, the light is coupled into polarization-maintaining (PM) optical fibers and transferred to the experiment. With the PM fibers, we are able to supply a stable polarization and intensity to the experiment with only a few tweaks to the intensity required on a more-than-monthly basis.

Two further laser systems are set up on the experiment table. One is the plug laser system at $660\,\mathrm{nm}$; the other, the heart of the experiment, is our versatile lattice setup at $1064\,\mathrm{nm}$. The plug laser is a solid-state laser, which is broadband but supplies up to $1\,\mathrm{W}$ of power. The setup includes an AOM for fast switching and a shutter for blocking the light entirely. Without the shutter and without keeping the AOM active, we observe cooling and heating cycles of the AOM, which lead to pointing issues. Due to this pointing, the fiber coupling efficiency fluctuates substantially when switching on. As soon as the shutter is closed the AOM is turned back on, i.e. it is always at its high temperature state and the pointing issues are eliminated. To position the laser beam precisely on the center of the magnetic trap, we use a mirror mount with piezo actuators. A more detailed account of how we position and optimize the plug laser can also be found in [36].

The laser setup for the lattice will be described in more detail in Chapter 3. We use a fiber laser with $50\,\mathrm{W}$ output at $1064\,\mathrm{nm}$ as a light source. The fiber laser is single-mode and has very low relative intensity noise (RIN), which is of high importance for cold atom lattice experiments.

Magnetic fields The main magnetic fields are provided by two sets of water-cooled coil pairs[46]. Both pairs can be used in Helmholtz and anti-Helmholtz configurations. Switching between the two configurations is realized with high-power insulated gate bipolar transistors (IGBT) in an H-bridge configuration. The coils are supplied by Delta Electronica power supplies with up to $200\,\mathrm{A}$ of current. With the combination of both coil pairs, we are able to create offset fields of up to $1500\,\mathrm{G}$ and magnetic-field gradients of up to $520\,\mathrm{G/cm}$ (both in Helmholtz and anti-Helmholtz, respectively). This covers the ranges needed for the following experiments well. In addition to the main coils we have three sets of compensation coils in Helmholtz configuration placed around the glass cell. Enabling us to compensate for stray fields and reposition the center of the quadrupole field at small gradients in the x-, y- and z- direction separately.

2.3 | Hot to ultra-cold

2.3.1 Oven and 2D-MOT

The oven sits at the bottom of the vacuum chamber, see figure .2.4. It is a cup of $83\,\mathrm{mm}$ length and $40\,\mathrm{mm}$ diameter designed to have high output flux [45]. The oven is heated by wires usually up to $700\,\mathrm{K}$. As Andreas Kerkmann pointed out in his thesis, the added $20\,\mathrm{g}$ of lithium should last for a long period. While writing this thesis, this period seems to be coming to an end. In the last year, we observed multiple "blobs," named after the signature spike in pressure preceding the loss of atoms. After a "blob," we lose the fluorescence signal of the 2D-MOT, and no atoms are loaded into the 3D-MOT. We attribute this loss of signal to an actual loss of atoms in the hottest part of the oven. As Andreas Kerkmann also described, vaporization in ultra-high vacuum is complex. Previously heated atoms may have cooled down and condensed further up the oven. We find that heating the system from the typical $420\,^{\circ}\mathrm{C}$ up to $500\,^{\circ}\mathrm{C}$ brings back the signal, melting some of the condensed atoms back into the hottest part of the oven.

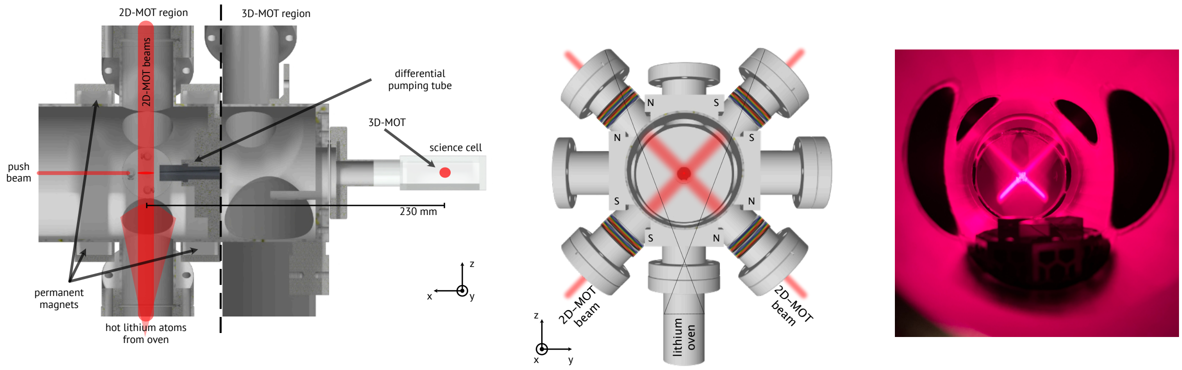

Figure 2.4: Vacuum setup cut and 2D-MOT. (Left) A cut through the CAD model of the vacuum chamber viewed from the side. The left part of the chamber is the high-pressure section, also referred to as the 2D-MOT region. From below, atoms are ejected from the oven and captured by the 2D-MOT beams. The permanent magnets are mounted to the left and right of the oven/2D-MOT plane. Perpendicular to that plane, the push beam pushes the atoms through the differential pumping tube into the science/glass cell on the right. The 3D-MOT region is the low-pressure section. In the science cell, the location of the 3D-MOT is depicted, where all further cooling stages and experiments take place. (Middle) View from the front of the experiment showing the $\pm 45^{\circ}$ angle of the 2D-MOT beams with respect to the oven axis. The fine black lines indicate the maximum ballistic angle exiting the oven. This design ensures that the viewports for the 2D-MOT do not get coated with lithium. (Right) Photograph of the 2D-MOT from the same view as in (b). CAD figures adapted from [36].

To initially cool and trap the hot atoms, we use a 2D-MOT. The atoms are confined to the axis connecting the centers of the 2D- and 3D-MOT, defined as the x-axis of the experiment, see figure 2.4. The directional and velocity-dependent force is created by a combination of a magnetic field gradient and laser light. The magnetic field gradient is generated by eight sets of stacked permanent magnets mounted to the vacuum chamber. The stacks of neodymium magnets create an octopole field with a magnetic field zero along the x-axis and a gradient of $56\,\mathrm{G/cm}$ in the perpendicular plane.

We use the D2 transition to slow down the atoms. Two sets of counter-propagating laser beams with the same circular polarization are crossed at 90° in front of the differentialw pumping tube. With respect to the oven axis, the beams are shone in through the viewports at $\pm 45^{\circ}$. The light is red-detuned from the D2 line by $\Delta_c = 12.42\,\Gamma$ and $\Delta_r = 5.86\,\Gamma$, with the natural linewidth $\Gamma = 2\pi \times 5.87\,\mathrm{MHz}$. These detunings are larger than the commonly used values [48] due to our multi-frequency approach. We use two EOMs: one imprints the sideband for the repumper, and the second one broadens the line by adding sidebands in multiples of $2\pi \times 12.5\,\mathrm{MHz} \approx 2.13\,\Gamma$, see also

[49, 50]. This broadening significantly enhances our loading rate in the 3D-MOT. The retro-reflected beams have a $1/e^2$-width of $6\,\mathrm{mm}$ and an intensity of $I_c = 211.8 I_{\mathrm{sat}}$ and $I_r = 82.1\,\mathrm{I}_{\mathrm{sat}}$, where $I_{\mathrm{sat}} = 2.54\,\mathrm{mW/cm^2}$ is the saturation intensity of lithium.

During optimization of the loading rate, we experimented with using just a single beam for the 2D-MOT and folding it back completely. This resulted in similar performance when looking at the loading rate of the 3D-MOT. We achieved better beam balancing with the two separate beams and proceed with this approach. During the course of this thesis, we also added offset coils around the tubing of the 2D-MOT beams. These offset coils allow us to manipulate the position of the magnetic field zero, optimizing it to be in front of the differential pumping tube. With an estimate of the offset field created by the coils of $1.7\,\mathrm{G/A}$, we get a repositioning of the trap $300\,\mathrm{\mu m/A}$ considering the magnetic field gradient of $56\,\mathrm{G/cm}$.

The radially confined atoms are pushed towards the 3D-MOT side with an additional laser beam along the x-axis, which is blue-detuned from the D2 transition by $\Delta_{push} = 5.28\,\Gamma$. The beam has a $1/e^2$-diameter of $1.45\,\mathrm{mm}$ and is slightly tilted upwards, so it does not pierce the 3D-MOT directly. With this detuning, a power of $1.9\,\mathrm{I}_{\mathrm{sat}}$ gives optimal performance of the 3D-MOT loading.

2.3.2 3D-MOT, cMOT and gray molasses

In the science cell, the atoms are captured by a 3D-MOT. Similar to the 2D-MOT case, we use light that is red-detuned from the D2 transition. We also use an EOM to imprint sidebands, one of which has the correct frequency for the repumper. In particular, the cooler and repumper are detuned by $\Delta_c = 6.64\Gamma$ and $\Delta_r = 8.16\,\Gamma$. The beams have a $1/e^2$-width of $10\,\mathrm{mm}$ and an intensity of $I_c = 21.8\,I_{\mathrm{sat}}$ and $I_r = 10.1\,I_{\mathrm{sat}}$. The two in-plane beams are rotated $\pm 45^\circ$ with respect to the x-axis and are retro-reflected after passing through the glass. The two out-of-plane beams propagate along the z-direction in opposite directions. They are all circularly polarized at the atoms. With a magnetic-field gradient of $25\,\mathrm{G/cm}$, created by the inner coil pair, the atoms are confined and cooled toward the magnetic field zero in the center of the science cell. Over the course of this thesis, we optimized the loading rate and the final number of atoms by an order of magnitude. The initial work was done in [45, 46] and the optimization was performed in close collaboration with Mathis Fischer, where a detailed account can be found on changes made [36]. We are now able to load 3×10^8 atoms in $3\,\mathrm{s}$, which is sufficient to reach degeneracy in the end. In contrast to the 2D-MOT, we find no enhancement in loading rate when we employ the multi-frequency approach in the 3D-MOT. We attribute this to the already reduced velocity distribution, such that additional frequencies only lower the intensity at the optimal one.

After loading the 3D-MOT for a particular time, we switch off all light in the 2D-MOT, including the light for the push beam. For the compressed MOT (cMOT), we ramp up the magnetic field to $100\,\mathrm{G/cm}$, lower the intensity of the beams to $0.41\,I_{\mathrm{sat}}$ and $0.19\,I_{\mathrm{sat}}$ and reduce the detunings to $5.62\,\Gamma$ and $7.14\,\Gamma$ over a total time of $40\,\mathrm{ms}$. These changes result in compression and further cooling of the cloud by approaching the theoretical temperature minimum ($\Delta = \Gamma/2$ and $I = 0$). The temperature is reduced from about $3.3\,\mathrm{mK}$ to $800\,\mathrm{\mu K}$ during this cooling step.

The last laser cooling step is the gray molasses (GM) [51–53]. The GM works best at zero magnetic field. Following the compression, the magnetic field gradients are switched off. To ensure zero magnetic field, we use the compensation coils to counter any remaining fields at the atoms. For the gray molasses, blue-detuned light is required. In contrast to the previous steps, we use the D1 line in this step. On the D1 line, the level structure supports a Λ-like system which enhances the performance of the gray molasses scheme [52]. The optimal cooling is reached with zero two-photon detuning $\Delta_{\mathrm{two}} = \Delta_r - \Delta_c$. The single-photon detunings of the cooler and repumper are at $\Delta_c = \Delta_r = 6.81\,\Gamma$. After applying the gray molasses for $5\,\mu\mathrm{s}$, we reach the final laser cooling temperature of $T = {\sim}35\,\mu\mathrm{K}$ and a peak phase-space density (PSD) of $\sim 3 \times 10^{-5}$.

2.3.3 Magnetic trap

Due to the high three-body loss rate of ^{7}Li, we cannot directly load into a deep optical dipole trap as is done for ^{6}Li. To our knowledge, there is only one instance where an all-optical approach has worked, and this only with a few hundred atoms in the BEC [54]. Other state-of-the-art ^{7}Li experiments rely on an evaporative cooling step in a magnetic trap [55–57].

To load the magnetic trap, we transfer all the atoms into a magnetically trappable state. As we are working with a static magnetic field, this has to be a low-field-seeking state. The low-field seekers minimize their energy with decreasing magnetic fields. In the Zeeman regime, these are the states $F = 1$, $m_F = -1$ and $F = 2$, $m_F = 1$ and 2. The energy landscape, and thereby the confining potential, is given by

$$\Delta E(r) = m_F g_F \mu_B |B(r)| \,, \tag{2.2}$$

with m_F the magnetic quantum number, g_F the Landé factor, and μ_B the Bohr magneton. From this equation, it is already evident that a larger m_F results in a stronger trapping potential. The Landé-factors have an almost equal absolute value but with an opposite sign, $g_F(F = 1) \approx -0.5021$ and $g_F(F = 2) \approx +0.4997$ (footnote[1]). We will work with the extremal state $F = 2$, $m_F = 2$. This choice is also beneficial for the transfer into that state. The $F = 2$, $m_F = 2$-state is dark for σ_+-transitions to the $F' = 2$-state on the D1-line. We apply a small magnetic bias field of $1\,\mathrm{G}$ to define a quantization axis. The atoms are illuminated from above and below to minimize the transferred momentum. We reuse the light from the gray molasses step, but we switch the polarization on the lower beam. The detunings are changed to $\Delta_c = 8.5\Gamma$ and $\Delta_r = 10.2\Gamma$. The two-photon detuning ensures that there are minimal Raman-transitions from one hyperfine ground state to the other. The intensities of the two frequencies are $12.4 I_{\mathrm{sat}}$ and $8.6 I_{\mathrm{sat}}$. The atoms are cycled through the m_F-state until they end up in $F = 2$, $m_F = 2$. On average, three absorbed photons are needed to transfer the atoms. To reduce the expansion of the cloud, we turn off the light after $150\,\mu\mathrm{s}$. After this time, we have transferred almost all atoms into $F = 2$, $m_F = 2$. The short time and only a few scattered photons, result in no significant heating of the cloud.

The magnetic trap is created by the combination of both coil pairs in an anti-Helmholtz configuration. This quadrupole configuration has a linear slope to the center. With both coil pairs, we can reach a

---

[1] The Landé-factors are calculated with $g_J(2\,{}^2\mathrm{S}_{1/2}) = 2.0024010(7)$ [58] and $g_I(2\,{}^2\mathrm{S}_{1/2}) = -0.0011822130(3)$[59].

maximum field gradient of $522\,\mathrm{G/cm}$ in the axial direction. The trap volume essentially extends over the central part of the science cell. This enables us to trap all atoms in the $F = 2$, $m_F = 2$-state. The magnetic trap is loaded by turning on a gradient of $18\,\mathrm{G/cm}$ linearly in $10\,\mathrm{ms}$. This value is mode-matched to the final extension of the cloud after laser cooling. The extent is primarily given by the cMOT-parameters. Mode-matching in this context optimizes the overlap of the gaussian density from laser cooling and the equilibrium density in the quadrupole trap, while ensuring the smallest possible heating and no atom loss[60]. As a result, there is almost no reduction in the phase-space density (PSD).

The quadrupole field has a true magnetic zero, i.e. the direction of the magnetic field lines point always away from this zero. For a particle passing through this point, this is an instantaneous flip of the direction of the magnetic field. The spin of atoms usually aligns with the slowly varying field direction. On a trajectory close to the zero-field point, the spin cannot follow the field direction adiabatically anymore, and an effective spin flip occurs. In our case, the spin is flipped from $m_F = 2$ to $m_F = -2$, which is an anti-confined state, and the atom is lost from the trap. This process is called Majorana loss[3, 61]. The effective radius at which the atoms are lost is given by $\sqrt{2\hbar\nu/\pi\mu_m B'}$ [62]. While lowering the temperature, this radius will decrease, but at the same time, the density in the trap will increase even faster. This leads to an increasing loss rate with decreasing temperature T as T^{-2} and renders the goal of the evaporation, which is increasing the PSD, unfeasible. To eliminate this loss mechanism, there are multiple possibilities: a few are mentioned here. A change in magnetic field configuration to either a Ioffe-Pritchard trap or clover-leaf trap, both of which have a non-zero trap floor; a time-orbiting potential (TOP) trap[63], in which the zero point is rotated around the cloud; or an additional repulsive potential in the center, which repels the atom out of the loss radius[3]. We use the latter option to prevent Majorana losses, as the other two are not feasible for our setup. The repulsive potential is created by a blue-detuned laser beam with a wavelength of $660\,\mathrm{nm}$. This is rather close to the D-lines compared to other experiments[55–57]. Moving closer to resonance reduces the intensity needed to form the repelling potential, but also comes with a higher scattering rate. With the low occupation in the high-power region, we see no heating of the cloud. The beam has a $1/e^2$ beam waist radius of $18\,\mu\mathrm{m}$. A power of $P = 700\,\mathrm{mW}$ on the atoms creates a potential barrier of more than $1\,\mathrm{mK}$.

During evaporation in the magnetic trap, we have to balance the thermalizing two-body collisions and the lossy and heating three-body collisions. The two-body cross-section scales linearly with the density $\sigma_2 \sim n$, while the three-body cross-section scales quadratically with the density $\sigma_2 \sim n^2$. The upper limit given by the high three-body loss rate is a density of $1 \times 10^{13}\,\mathrm{cm}^{-3}$. The scattering rate of the elastic collisions scales as $\Gamma_{el} \propto (B')^{4/3}$ in a quadrupole trap, with (B') the magnetic field gradient[36]. With the small scattering length in the $F = 2$-manifold of $a_s = -27a_0$, the atoms would take a rather long time to thermalize. To speed up the process, the magnetic field gradient is increased to its maximum value, ensuring that the upper limit in density is not reached. The compression from $18\,\mathrm{G/cm}$ to $533\,\mathrm{G/cm}$ is done adiabatically; i.e., no PSD is lost during the process. The temperature is increased significantly, but so is the density of the cloud. The higher density kickstarts the thermalization process.

We perform forced evaporation with a so-called RF-knife. We use the radio-frequency transition from the trapped state $F = 2$, $m_F = 2$ to the untrapped state $F = 1$, $m_F = 1$. At zero magnetic field, the frequency of that transition is the hyperfine splitting of the two ground state manifolds of $\Delta E = h \times 803.5\,\mathrm{MHz}$, where h is the Planck constant. For increasing magnetic fields, the gap between the two states increases with $\Delta E(|B|) \sim \frac{3}{2}|B|$. Only the hottest atoms are able to probe the full extent of the cloud's density, due to energy conservation. This allows us to select only those atoms at the edge of the cloud, where the magnetic field is highest. We use a home-built radio-frequency antenna optimized for $800\,\mathrm{MHz}$ to $1000\,\mathrm{MHz}$ to flip the spin of the atoms. During the adiabatic compression, we already apply a radio-frequency of $950\,\mathrm{MHz}$ to remove exceptionally hot atoms from the cloud. We now reduce the radio-frequency, thereby removing the hottest atoms from the cloud. The cloud rethermalizes via elastic collisions. While the overall temperature is reduced, the density increases and, if unchecked, would lead to exceeding the upper density limit of $1 \times 10^{13}\,\mathrm{cm}^{-3}$. Above that limit, the lossy three-body collision will dominate the thermalizing two-body collisions, especially in the coldest part of the cloud where the density is highest. This would counteract the evaporation process and fail to increase PSD. To circumvent this effect, we decompress the cloud by lowering the magnetic field gradient simultaneously. The frequency and magnetic field gradient are reduced linearly in three consecutive ramps, which are each optimized experimentally for maximum final PSD and short duration. The final frequency is $807.475\,\mathrm{MHz}$ at a field gradient of $208\,\mathrm{G/cm}$. The whole magnetic field evaporation takes $7.3\,\mathrm{s}$ with a PSD gain of almost three orders of magnitude up to 9×10^{-2}.

2.3.4 Optical dipole trap

Reaching degeneracy with a negative scattering length is possible, but only for a small number of atoms in the condensate [64]. In our magnetic trap configuration, we are bound to the background scattering length of the singlet and triplet states, which are both rather small. In an optical dipole trap (ODT), we can utilize an offset magnetic field to increase the scattering length via the broad Feshbach resonance, and thereby increase the two-body elastic scattering rate. This results in fast thermalization and reduces the time of the final evaporation step. To prepare the atoms for evaporation in the ODT, we perform a tiny magnetic transport of approximately $200\,\mathrm{\mu m}$, load the atoms from the magnetic trap into the ODT, perform a Landau-Zeener sweep, and ramp up the offset field. Finally, we lower the depth of the ODT and eventually reach degeneracy. The steps will be described in the following.

Starting from the field minimum of the anti-Helmholtz configuration, we have to perform a very short transport of the cloud. In the Helmholtz configuration, there remains a residual field curvature in the center of the two coils, creating a radially confining potential for low-field seekers and an anti-confinement in the axial direction. This curvature is minimal and centered in the optimal Helmholtz configuration; see also [46] for our setup. The machining and wiring cause deviations from the perfect case, leading to an offset of the symmetry points for each of the coil pairs and configurations. Unfortunately, this prevents us from reducing the curvature and eliminating it completely[65]. The zero-field points of the anti-Helmholtz configuration are measured by evaporating deep into the magnetic trap and imaging there. For the zero-crossing of the first derivative in the Helmholtz configuration, we have to jump ahead and utilize the BEC. With the BEC, we are able to perform oscillation measurements in a single beam and detect the slope minima in the radial plane. The zero-field point of the combined coils in the anti-Helmholtz configuration is about $400\,\mu\mathrm{m}$ away from the outer-coil Helmholtz coil slope minimum. The distance to the slope minimum of the combined-Helmholtz configuration is smaller, about $200\,\mu\mathrm{m}$, and lies along one of the dipole trap laser beams. The importance of working at the minimum of the slope stems from the features of the matter-wave magnifier, which will be discussed in the following chapter. We choose to work in the combined Helmholtz configuration. We ramp up the intensity of the optical dipole trap and by adjusting the current in the horizontal compensation coil, we move the zero-field center of the quadrupole field along the x-axis towards the new position: the slope minimum of the combined-Helmholtz configuration and the crossing point of the three laser beams.

The optical potential is created by three laser beams intersecting with $120°$ between each pair. The crossing point is located approximately $100\,\mu\mathrm{m}$ below the magnetic trap center. With a bias field of $0.1\,\mathrm{G}$ to ensure spin polarization, we lower the trap field and spill the atoms into the optical potential. The bias field is directed so that the zero-field point is pulled away from the ODT. The atoms are captured in an optical potential with a depth of approximately $U(0) = -240\,\mu\mathrm{K}$. We are able to transfer about $30\,\%$ of the atoms from the magnetic trap to the dipole trap with a slight loss of PSD. After the transfer of the atoms, the PSD is 9.7×10^{-3} at a temperature of $24.4\,\mu\mathrm{K}$.

With the quadrupole field turned off, we increase the bias field to $4.8\,\mathrm{G}$ and perform a Landau-Zeener sweep. We couple the states $|F = 2, m_F = 2\rangle$ and $|F = 1, m_F = 1\rangle$ with a radio-frequency at $813.6\,\mathrm{MHz}$. This is blue-detuned to the bare hyperfine splitting of $F = 1$ and $F = 2$ and to the Zeeman-splitting at the current field. In this way, we ensure that we only couple the desired extremal states. By increasing the magnetic field, the radio frequency is brought to resonance and then out of it again, thereby transferring the atoms adiabatically from one state to the other. We increase the magnetic bias field to $9.5\,\mathrm{G}$ in 40 ms and reach near to unity transfer.

In $100\,\mathrm{ms}$, we ramp up the Feshbach field, a bias field created by both coil pairs, now in Helmholtz configuration. The field is ramped up to $702\,\mathrm{G}$, which is close to the inter-spin Feshbach resonance of the $|F = 1, m_F = 1\rangle$ state. The scattering length here is $a_s = 76a_0$. At this field, we start the forced evaporation process again by lowering the optical power exponentially, thus reducing the depth of the potential U as

$$U(t) = U_0 \exp\left(-\frac{t}{\tau}\right) \,. \tag{2.3}$$

We experimentally find $\tau = 0.2\,\mathrm{s}$.

We take time-of-flight (TOF) measurements and analyze the resulting density (Fig. 2.5). Usually, one extracts the condensate fraction and the temperature from a bimodal distribution consisting of a Thomas-Fermi profile for the condensed part and a Bose-enhanced Gaussian [62] for the thermal distribution. The bi-modal function has the following form:

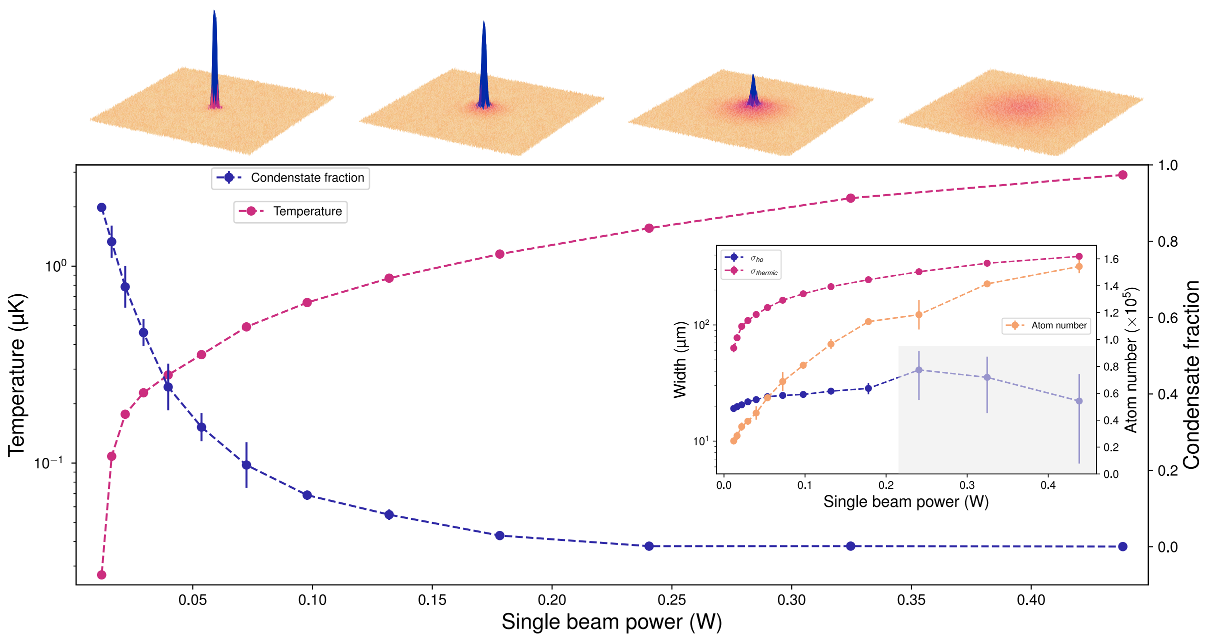

Figure 2.5: Formation of the Bose-Einstein Condensate. (Top) Formation of a the BEC. From right to left the atomic cloud is evaporated by lowering the dipole potential and the ground state is macroscopically populated, visible in the sharp peak in the center of the broad thermal cloud. From right to left the single-beam final power is $438\,\mathrm{mW}$, $132\,\mathrm{mW}$, $40\,\mathrm{mW}$ and $12\,\mathrm{mW}$ at a ToF-duration of $4.5\,\mathrm{\mu s}$.(Bottom) Condensate fraction and temperature of the cloud. In blue the condensate fraction of atoms in the ground state is shown with the temperature in red. The inset shows the width of the thermal and condensate part after $4.5\,\mathrm{ms}$ time-of-flight as well as the total atom number. The gray shaded area corresponds to the part where no significant condensate fraction could be extracted.

$$n_{tot}(\boldsymbol{r}) = n_{th} Li_{3/2}\left(\prod_{i=1}^{3} \exp\left(-\frac{x_i^2}{x_{i,th,0}^2}\right)\right) + n_c \max\left(1 - \sum_{i=1}^{3} \frac{x_i^2}{x_{i,c}^2}\right) \quad , \tag{2.4}$$

where n_{th} is the peak density of the thermal atoms and n_c is the peak density of the condensate, $x_{i,th,0}$ is the width if the thermal Bose-enhanced gaussian and x_i, c is the Thomas-Fermi radius. $Li_\alpha(z)$ is the polylogarithm. The Thomas-Fermi profile here is based on a harmonic potential. However, the Thomas-Fermi approximation does not fit well for the tight confinement created by the small waist of $w_0 = 41\mu m$. The bare ground state of the harmonic oscillator works better, so we assume the following three-dimensional density profile:

$$n_{tot}(\boldsymbol{r}) = n_{th} Li_{3/2}\left(\prod_{i=1}^{3} \exp\left(-\frac{x_i^2}{x_{i,th,0}^2}\right)\right) + n_c \prod_{i=1}^{3} \frac{1}{x_{i,c,0}} \exp\left(-\frac{x_i^2}{x_{i,c,0}^2}\right) \quad . \tag{2.5}$$

and fit the column density of the above as

$$\tilde{n}_{tot}(x,y) = \frac{\tilde{n}_{th,0}}{Li_2(1)} Li_2\left(\exp\left(1 - \frac{x^2}{x_{th,0}^2} - \frac{y^2}{y_{th,0}^2}\right)\right) + \frac{\tilde{n}_{c,0}}{x_{c,0} y_{c,0}} \exp\left(-\frac{x^2}{x_{c,0}^2} - \frac{y^2}{y_{c,0}^2}\right) \tag{2.6}$$

where we integrated out the z-direction. We perform the fit of the bimodal distribution stepwise: first we roughly fit the distribution to get the center and a rough estimate for the cloud width. We then fit the thermal fraction excluding the central region, followed by a fit to the condensate fraction only. The final fit uses both distributions with the optimal initial fits found from the previous fits. In figure 2.5, we show the extracted temperature and condensate fraction. A first onset of condensation is at $P_i = 200\,\mathrm{mW}$ per beam, corresponding to an approximate depth of $U = 13.7\,\mu\mathrm{K}$ and an almost pure condensate at $P_i = 9\,\mathrm{mW}$ per beam, with about 3×10^4 atoms and a temperature below $50\,\mathrm{nK}$. At these low temperatures, it becomes difficult to extract the temperature as the thermal part gets lost in the background signal.

When we estimate the critical temperature T_c by calculating the geometric mean trap frequency $\bar{\omega} = (\omega_r^2 \omega_z)^{1/3}$ via the final power in the dipole trap,

$$\left(\frac{T}{T_c}\right) = \frac{k_\mathrm{B} T}{\hbar \bar{\omega}} \left(\frac{Li_3(1)}{N}\right)^{1/3}, \tag{2.7}$$

with $Li_3(1) \approx 1.2$. The trap frequencies range from $2\pi \times 1.16\,\mathrm{kHz}$ to $2\pi \times 0.16\,\mathrm{kHz}$. With the measured total atom numbers, N, the condensate fractions are plotted against the reduced temperature, T/T_c, in figure 2.6, which matches the expectation for a finite system[66]. From a few repeated measurements at a time-of-flight between $t_\mathrm{ToF} = [4, 4.5, 5, 5.5]\,\mu\mathrm{s}$ (in total, 20 repeats per data point), we can reproduce the number fluctuation in the condensate fraction, as in [67, 68]; but note that we expect systematic errors on the critical temperature. A more precise calibration of the trap frequencies would be needed, as well as better atomic number detection calibration. It remains remarkable what can be learned from a simple calibration measurement, and opens up the possibility to investigate these phenomena in more depth using this machine.

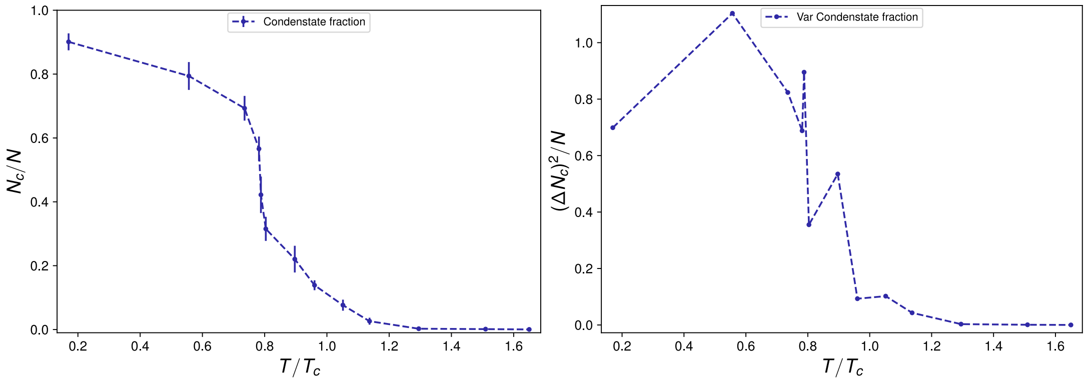

Figure 2.6: Condensate fraction vs. reduced temperature. (Left) The condensate fraction is plotted against the reduced temperature T/T_c. (Right) Variance of the number of atoms in the condensate normalized by the total atom number.

Conclusion & Outlook

In this chapter, we introduced our machine producing BECs of ^{7}Li with up to 3×10^4 atoms. Each experimental cycle has a duration of $13\,\mathrm{s}$, i.e. a repetition rate of about $77\,\mathrm{mHz}$. We note the long stability of the whole system over a duration of multiple months. All cooling stages, including the MOT, GM, magnetic trap, and ODT, are optimized by natural intelligence, but this comes with limitations on time and multi- dimensional processing capabilities. We assume that artificial intelligence, in particular machine learning, will be impactful in increasing the repetition rate towards the $1\,\mathrm{Hz}$ regime and in improving the number of atoms in the condensate. This would allow for more statistics to be gathered and enable quantum phenomena to be probed in more detail. As of writing this thesis, first results toward this direction are being achieved with a new experiment control with direct machine learning capabilities[69].

CHAPTER 3

A versatile optical trap setup

The heart of the experiment is our three-beam versatile lattice/ODT setup. For one thing, the optical dipole trap used to prepare the BEC in the previous section is one configuration of it. Another use case is the hexagonal lattice with tunable geometry. During this thesis, we rebuild the lattice setup of the experiment. The new setup combines those and more features into one. Essentially, starting from the evaporation in the ODT over the optical lattice up to the matter-wave lens can be realized with a single setup of three intercepting beams. A single feature can be achieved by carefully selecting the appropiate frequencies of the light in each beam path. This approach follows innovative work in [70] and adds more tunability. The setup will be described in the following, see also [36].

3.1 | Setup

The lattice and trap potential is created by three intercepting laser beams with an angle of 120° between each pair. We use a single Coherent Mephisto Mopa at $1064\,\mathrm{nm}$ as the light source for all beams. The maximal output power is about $50\,\mathrm{W}$. The output power can be tuned, but to keep a consistent beam shape, we always run it at a constant value, in particular at almost maximum power. High power light beams cause thermal lensing in optical elements. A careful choice of elements can reduce it and at a constant power this effect can be compensated, adequately. A sketch of the setup is depicted in figure 3.1. The setup is described following the laser beam propagation from the laser head. To protect the laser, we first pass the beam through a high-power optical isolator with a backwards suppression of approximately $55\,\mathrm{dB}$. Here we deemed a single isolator sufficient as we are not reflecting the beam back into itself, so only minor reflection could be coupled back into the laser. We use a $\lambda/2$-waveplate and a Glan-Laser polarizer to clean the polarization and set the power for the preparation setup. The light is split into three paths with equal power by three consecutive $\lambda/2$-waveplate and polarizing beam splitter (PBS) cube combinations. Each path is a copy of the other two regarding beam shape and length, as well as used devices and optics. A lens before the splitting of the beam focuses the beam into the acousto-optical modulators (AOM). The AOMs, A1, A2 and A3, are set up in a double-pass configuration. The s-polarization from the splitting output is reflected at the following PBS cube and passed through the AOM. With a combination of a $150\,\mathrm{mm}$ lens, a quarter-waveplate, and a mirror under 0°, the light is retro-reflected and passed a second time through the AOM. All diffraction orders except for the first positive one are dumped

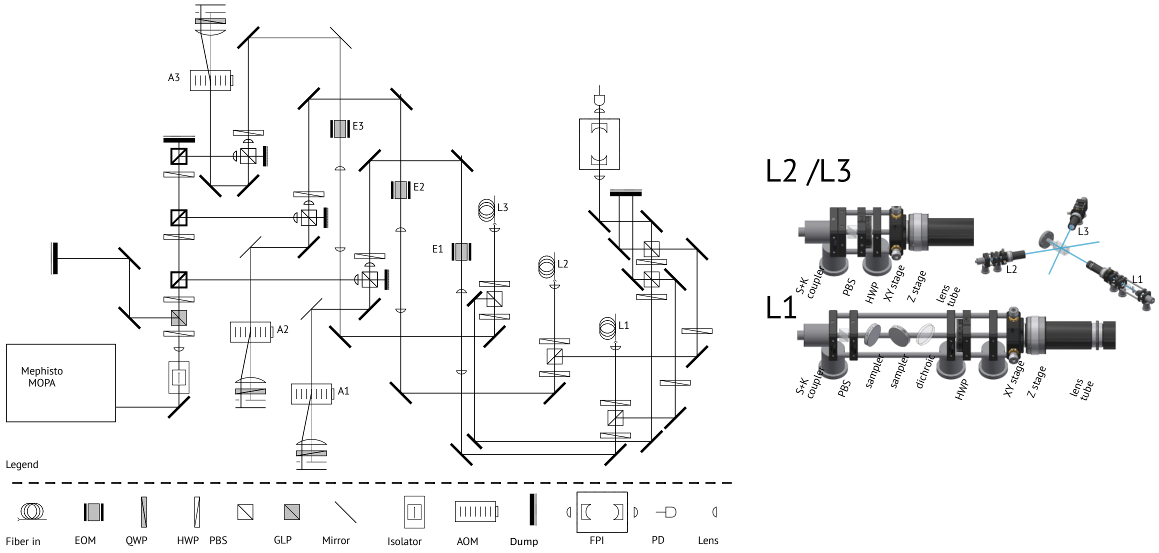

Figure 3.1: Lattice laser setup and fiber out-couplers. (Left) The lattice setup before the optical fibers. As described in the text, each path includes a double-pass AOM and an EOM to realize the various potential configurations. Also shown is a Fabry-Perot cavity, which we use to monitor the carrier and the sidebands created by the EOMs. (Right) CAD-drawing of the fiber out-couplers. The compact mounting increases stability further. The x-y-translation stage, to which the final lens is mounted, is used for precise radial positioning of the focus. In the propagation direction, a non-rotating z-translation is used for precise axial positioning of the focus. The upper right shows the CAD-drawing of the configuration around the science cell with the beams visualized in blue. (Figure adapted from [36].)

after each pass through the AOM. The light is now p-polarized and is transmitted through the cube. The transmission through the PBS in the end is essential for a stable polarization over a large dynamical range of power. The beam is now collimated with a diameter optimized for the following electro-optical modulator (EOM). The three EOMs, E1-E3, differ in their resonant frequency. The frequencies are $\nu_{0,E1} = 10\,\mathrm{MHz}$, $\nu_{0,E2} = 35\,\mathrm{MHz}$, and $\nu_{0,E3} = 45\,\mathrm{MHz}$. The values are engineered for the multi-frequency approach as well as to avoid excitations and heating in the different trap setups. Behind the EOMs, the size of the beam is shaped with a telescope for optimal fiber coupling. In front of the fiber coupler, a half-waveplate-PBS-half-waveplate combination is placed. The first waveplate is mainly there for maintenance, where the power on the fiber can be reduced for fiber coupling, while having full power up to the cube. With this, we can ensure that thermal lensing does not affect the coupling efficiency when using full power on the fiber coupler. During runtime, the waveplate is positioned such that maximal power is transmitted. The PBS cube ensures that we have a clean polarization in front of the fiber. The second waveplate is used to match either the slow or fast axis of the high-power polarization-maintaining (PM) photonic crystal fiber. A misalignment of the polarization will cause stress-dependent polarization fluctuation during transmission through the fiber and with the PBS behind the fiber, transform those into intensity fluctuations. Intensity fluctuations are a known heating source for the ultra-cold atoms and are reduced to a minimum with optimal polarization coupling.

With the fibers, the light is transferred to the experiment. The use of fibers limits the total power usable per beam path. The upper limit here is $15\,\mathrm{W}$ of power in front of the fiber, which is sufficient for the planned experiments. Currently, $5.3\,\mathrm{W}$ are used in front of the fiber, which results in a maximum of power of $3.7\,\mathrm{W}$ on the atoms per beam. The fiber highly enhances the beam quality and pointing stability, which are essential for the lattice potential and the matter-wave magnification. One of the benefits of using fibers is the modularity, essentially decoupling work on the preparation side and experiment side. The light is coupled out of the fiber, passed through a PBS cube for polarization cleaning, followed by a half-waveplate to set the final polarization and focused onto the atoms (Figs. 3.2 and 3.2). A lens with a focal length of $f = 150\,\mathrm{mm}$ creates a beam waist with a $1/e^2$-radius of $w_0 = 41\,\mu\mathrm{m}$. The setup is the same for beams L2 and L3. The laser beam going along the glass cell, L1, has no exit on the other side and is dumped onto the steel chamber. To actually hit the steel chamber and not the graphite differential tube, the propagation axis is tilted by about 2° with respect to the normal of the glass-cell's front. Because the beam is not exiting the chamber, the setup in front of the glass differs from the other two described below. Two beam samplers follow the cube, and one is used for intensity monitoring. A low-pass dichroic mirror allows imaging the atoms from the other side along this axis by reflecting light at $671\,\mathrm{nm}$.

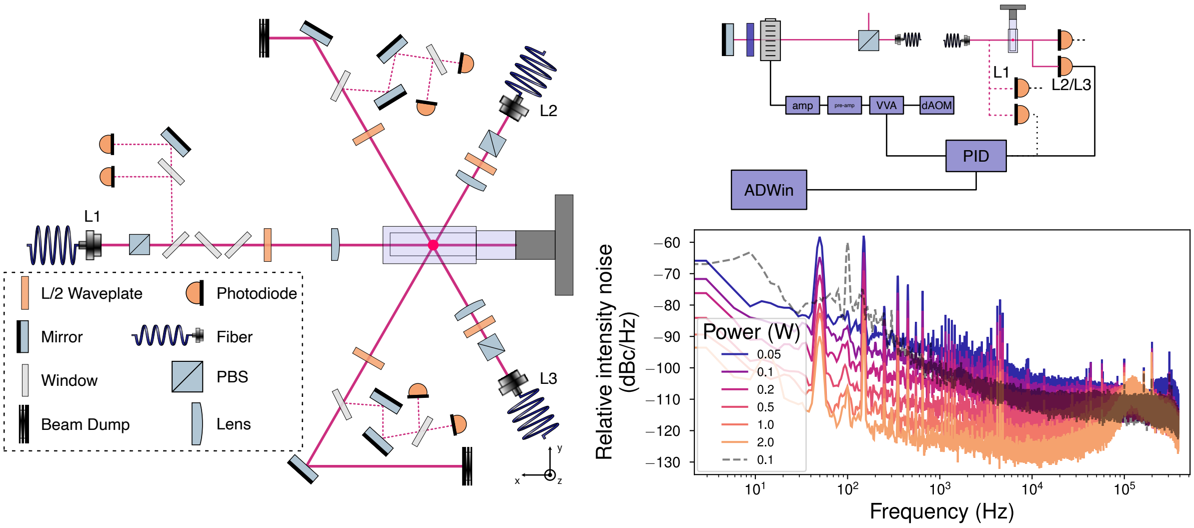

Figure 3.2: Lattice setup around the glass cell and intensity-lock. (Left) Sketch of the lattice setup around the science cell. (Upper right) Sketch of the intensity-lock setup. (Lower right) Relative intensity noise of the L1 axis. We see a reduction of the RIN when we activate the lock. The intensity lock is less efficient for lower powers, but still reduces the noise compared to the unregulated case. The dashed, half-transparent line is with the lock deactivated.

To control and monitor the power, we use an in-loop photodiode (PD) and an out-of-loop PD, respectively. The in-loop PD is part of the control circuit in figure 3.2 and directly connected to the intensity regulator. The set voltage for the intensity regulation is given by a designated analog output of the ADWin-controller. The base, constant RF-power supplied by a home-built digital AOM driver is regulated via a variable voltage attenuator (VVA). The RF-power is doubly amplified with a low-power followed by a high-power amplifier. The maximum RF-power is set such that the AOM is driven in the optimal range, just below its maximum diffraction efficiency. The intensity-controlled power of the light is passed through the fibers and measured by the in-loop PD closes the control circuit. With the out-of-loop PD, we are able to monitor the intensity without affecting the control circuit.

With the out-of-loop PD, we measure the relative intensity noise (RIN). In figure 3.2, the RIN for one of the beams is given. The other two can be found in appendix B. The servo-bump for these settings is located above $100\,\mathrm{kHz}$. We see the RIN increasing for lower power settings by about $20\,\mathrm{dB}$ at the minimal RIN of the $2.5\,\mathrm{W}$-power setting on the atoms with the laser always at maximum output power. This still gives a reduction in RIN compared to the unregulated case.

3.2 | Three "non-interfering" beams

The intensity field of the red-detuned laser beams forms an attractive potential for the atoms which is proportional to the intensity of the light field [71]. The oscillating electric field E induces an oscillating dipole moment $d = \alpha(\omega)E$ with complex polarizability α of the atom and ω the frequency of the light. The resulting potential is given by averaging the oscillations in time as $U_{dip} = -\frac{1}{2} < dE >= -\frac{1}{2\epsilon_0 c}Re(\alpha)I$ with $I = \frac{1}{2}\epsilon_0 c|E|^2$, where ϵ_0 is the vacuum permittivity and c the sped of light. While the real part of α is related to the potential the atoms experience, the imaginary part is related to the probability that a trap photon scatters from the atoms as $\Gamma_{sc} = -\frac{dE}{\hbar\omega} = -\frac{1}{\hbar\epsilon_0 c}Im(\alpha)I$, with $\hbar$ the reduced Plank constant. For large detunings $\Delta = \omega - \omega_0$ to the atomic resonance ω_0, the scattering rate $\Gamma_{sc}(r)$ and the dipole potential $U_{dip}(r)$ can be approximated as

$$U_{dip}(r) = -\frac{3\pi c^2}{2\omega_0^3}\left(\frac{\Gamma}{\omega_0 - \omega} - \frac{\Gamma}{\omega_0 + \omega}\right) I(r) \tag{3.1}$$

$$\Gamma_{sc}(r) = \frac{3\pi c^2}{2\hbar\omega_0^3}\left(\frac{\omega}{\omega_0}\right)^3 \left(\frac{\Gamma}{\omega_0 - \omega} - \frac{\Gamma}{\omega_0 + \omega}\right)^2 I(r)\ . \tag{3.2}$$

With the double-pass AOMs, we are able to detune the frequencies of the three beams far enough from each other to create a running wave pattern with frequencies much higher than any relevant energy scale in the traps used. This results in a time-averaged potential for the atoms, and the three beams can be considered essentially non-interfering. The potential is then given by the sum of the intensities of the three single beams: $U_{\mathrm{avg}}(r) = \sum_{i=1}^{3} I_i(r)$. The electric field of the laser beam is described by a Gaussian beam distribution of the form

$$\boldsymbol{E}(r,z) = E_0 \boldsymbol{x} \frac{w_0}{w(z)} \exp\left(\frac{-r^2}{w(z)^2}\right) \exp\left(-i\left(kz + k\frac{r^2}{2R(z)^2} - \psi(z)\right)\right)\ , \tag{3.3}$$

where E_0 is the amplitude of the electric field, $\boldsymbol{x}$ is the polarization direction, $w(z)$ is the $1/e^2$-radius of the intensity in the radial direction with w_0 its minimum, k is the absolute value of the wavevector, $R(z)$ is the curvature radius, and $\psi(z)$ is the Gouy-phase [72]. Note that z and r are used as scalar values. For each beam, z_i and r_i are defined as the scalar projection $z = \frac{\boldsymbol{r}\cdot\boldsymbol{k}}{||\boldsymbol{k}||}$ and scalar rejection $r = (\boldsymbol{r} - \boldsymbol{z})\hat{\boldsymbol{k}}$ onto the wavevector $\boldsymbol{k}$ with the vector rejection $\boldsymbol{z}$. The vector $\boldsymbol{r}$ is the vector pointing from the waist location $\boldsymbol{z_0}$ to an arbitrary position $\boldsymbol{r'}$ such that $\boldsymbol{r} = \boldsymbol{r'} - \boldsymbol{z_0}$. Around the crossing point, $\boldsymbol{z_0} = \boldsymbol{z_{0,i}}$, the potential is approximately harmonic and isotropic. The expansion of a single beam gives

$$V(r,z) \approx -V_0 \left(1 - 2\left(\frac{r}{w_0}\right)^2 - \left(\frac{z}{z_R}\right)^2\right) , \tag{3.4}$$

with the Rayleigh range z_R. The potential depth is given by $V_0 = \kappa_{\text{dip}} I_0$, with the peak intensity of the Gaussian beam $I_0 = 2P/\pi w_0^2$ and κ_{dip} defined as the pre-factor to the intensity from eq. 3.1. This results in trap frequencies $\omega_{sb,\perp} = \sqrt{4V_0/mw_0^2}$ and $\omega_{sb,\parallel} = \sqrt{2V_0/mz_R^2}$. The latter will be negligible as $w_0 \ll z_R$. For the three-beam setup, the trap frequencies add up in the axial direction to $\omega_z = \sum \omega_i = 3\omega_{sb,\perp}$ with $\omega_i = \omega_{sb,\perp}$. In the radial direction, the frequencies are added up taking into account their relative angles, resulting in

$$\omega_r = \sqrt{\sum \cos(\theta_i)^2 \omega_i^2} = \sqrt{\frac{3}{2}}\omega_{sb,\perp} \tag{3.5}$$

with $\theta_i = [0, 2/3\pi, 4/3\pi]$ and $\omega_i = \omega_{sb,\perp}$. This gives a fixed aspect ratio of $\omega_z = \sqrt{2}\omega_r$ in our setup.

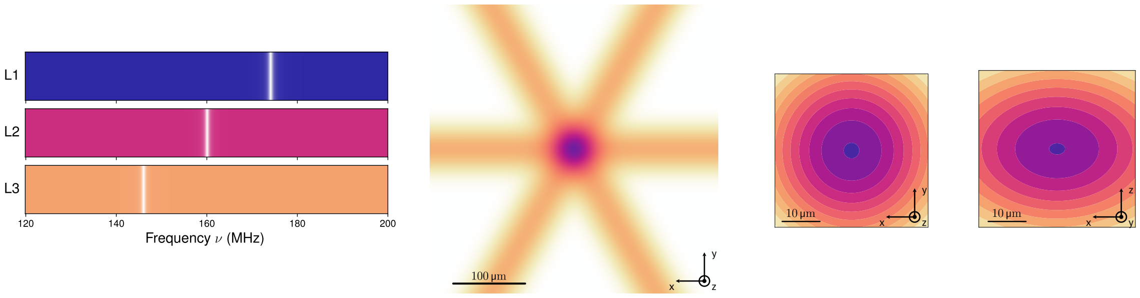

Figure 3.3: Non-interfering frequencies and averaged potential. (Left) The three panels visualize the frequencies used for this setup on each of the three axes. Color represents no intensity, white shows relative maximal intensity. For the non-interfering setup, e.g. the ODT, the double-pass AOMs are set to $87\,\mathrm{MHz}$, $80\,\mathrm{MHz}$ and $73\,\mathrm{MHz}$ resulting in an added frequency of $174\,\mathrm{MHz}$, $160\,\mathrm{MHz}$ and $146\,\mathrm{MHz}$ to the frequency of the laser. (Middle) The resulting potential for the time-averaged case, i.e. the non-interfering setting. (Right) Zoom into the center of the potential. On the left, the top view is depicted showing the radial isotropic potential around the crossing point. On the right, a side view is shown visualizing the aspect ratio of the trap, $w_z = \sqrt{2}w_r$.

With the non-interfering beams, we are able to perform forced evaporation by lowering the power of the beams and thereby reducing the potential depth. We are able to load the atoms into this optical potential, hold them there, and finally evaporate the cloud to degeneracy. This is only possible with sufficient detuning of the three laser beams. If the light of the three beams is too close in frequency, we observe substantial atom loss. The detuning needed is correlated to the maximal used onsite trap frequency, and we determine it experimentally for our initial potential depth with $P = 3.5\,\mathrm{W}$ per beam. For a triangular lattice, this gives an onsite trap frequency of approximately $\omega_{\text{onsite}} = 2\pi \times 0.9\,\mathrm{MHz}$, estimated from the trap geometry. In figure 3.4, we measure the atom number only $1\,\mathrm{ms}$ after loading from the magnetic trap for different detunings between L1 and L2. We observe a drastic drop as the detuning is reduced below $4\,\mathrm{MHz}$ towards $2\,\mathrm{MHz}$, where the atoms are lost completely. This corresponds to approximately a factor of four to the onsite trap frequency. We attribute this loss to a heating mechanism due to the running waves and possible atom transport. Setting the two frequencies to resonance, we regain some atomic signal as we essentially load directly into a lattice with no running waves. The AOMs have a resonance frequency of $\nu_0 = 80\,\mathrm{MHz}$, so we add a frequency of $2\nu_0 = 160\,\mathrm{MHz}$ to the bare laser frequency. The detuning in figure 3.4 is in reference to the added $2\nu_0$. We usually work with a minimal $\Delta\nu = 14\,\mathrm{MHz}$ during evaporation to suppress any heating mechanism while maintaining sufficient power behind the AOM. Larger detunings to the resonance of the AOM would lead to significant power loss in the first diffraction order.

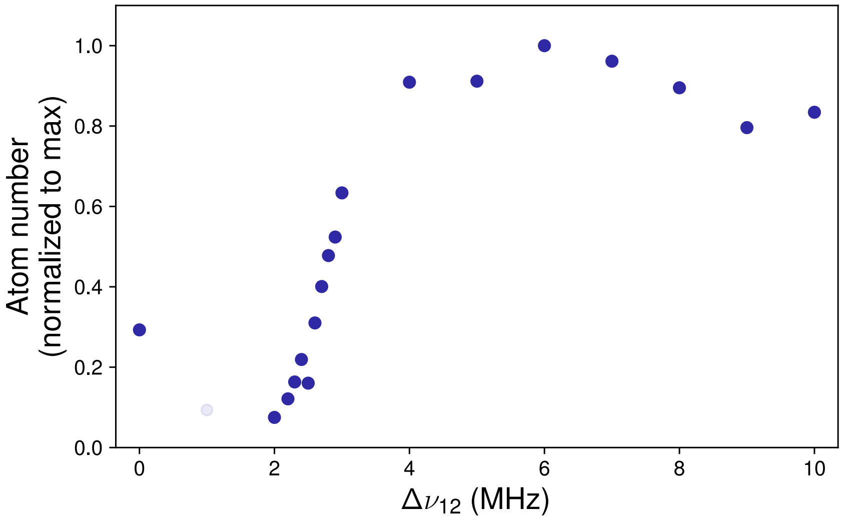

Figure 3.4: Heating effect for close detuning. The atom number in the ODT after a short hold time and directly after it has been loaded from the magnetic trap. The slight rise at 1 MHz is a fit error due to the background and is grayed out. The power per beam is $P = 3.5\,\mathrm{W}$, which gives an onsite trap frequency of $\omega_{\mathrm{onsite}} = 2\pi \times 0.9\,\mathrm{MHz}$. A detuning with $\Delta > 4\omega_{\mathrm{onsite}}$ seems to be critical to reduce heating.

With the cloud evaporated down to degeneracy, we are able to further optimize the overlap of the three beams. A perfect overlap will be crucial for the matter-wave microscope, where the non-interfering setup is used to create a strong harmonic confinement as the matter-wave lens. We start with aligning the beams in the out-of-plane direction. The atoms are therefore imaged from the side. First, we prepare a BEC only with two beams. Prior to imaging, one beam is turned off instantly and the oscillation mapped out by holding the cloud for different times in the single beam. From the fitted amplitude and the free-expansion duration, we can determine the distance between the two beams. The final focusing lens of the out-coupler setup is set in an x-y translation stage, which we use to carefully adjust to reduce the amplitude of the oscillation. At some point, the resolution and signal-to-noise of imaging from the side don't allow a more precise fit, but with the last reasonable oscillation, we can set an upper limit on the distance between the two beams of less than a micrometer. We repeat the process with a BEC in all three beams and successively turning off the third beam. With all beams overlapped in the axial direction, we proceed with overlapping them in-plane. Here we repeat the process starting directly with a three-beam BEC and turning off the third again, because the first two beams are crossed optimally already by the initial step. Due to the coupled degrees of freedom of the translation stage, the whole process has to be iterated a few times to reach the sub-micrometer overlap.

3.3 | Triangular lattice

If we set the AOMs to resonance $\Delta\nu_i = 0$, the resulting potential becomes periodic with a hexagonal basis. With the polarization pointing out of the intercepting plane, one gets a triangular lattice structure as visualized in figure 3.5. In contrast to the above, the beams cannot be treated separately, but the full interference has to be taken into account. The resulting intensity is given by

$$\boldsymbol{I}(\boldsymbol{r}) = \frac{c\epsilon_0}{2} \left|\boldsymbol{E_1}(\boldsymbol{r}) + \boldsymbol{E_2}(\boldsymbol{r}) + \boldsymbol{E_3}(\boldsymbol{r})\right|^2 \tag{3.6}$$

$$= \frac{c\epsilon_0}{2} \left(\sum_{i=1}^{3} |E_i(\boldsymbol{r})|^2 + \sum_{<i,j>}^{3} \left(E_i(\boldsymbol{r})^* E_j(\boldsymbol{r}) + c.c\right) \right) \ . \tag{3.7}$$

With the Gaussian beam profile (eq. 3.3), the first sum will result in a slowly varying Gaussian envelope. The second sum gives rise to a periodic potential, the optical lattice. A simplified version of the optical lattice can be reached by using plane waves propagating along the wavevectors $\boldsymbol{k}_i$ for the light field, following [73] loosely. The electric field is described by

$$\boldsymbol{E_i}(\boldsymbol{r}, t) = \sqrt{\frac{2I_i}{c\epsilon_0}} \boldsymbol{e}_{s,i} \exp\left(i(\boldsymbol{k_i} \cdot \boldsymbol{r} - \omega t - \phi_i)\right) \ , \tag{3.8}$$

where $\omega = 2\pi\lambda/c$ is the laser frequency, ϕ_i a phase delay for each beam, and $\boldsymbol{e}_i$ the polarization of the light. The angle of $120°$ between pairs of the three wavevectors $\boldsymbol{k}_i$, depicted in figure 3.5, gives the following orientations in our setup

$$\boldsymbol{k_1} = k_L(1, 0, 0), \qquad \boldsymbol{k_2} = k_L(-1/2, -\sqrt{3}/2, 0) \qquad \text{and} \qquad \boldsymbol{k_2} = k_L(-1/2, \sqrt{3}/2, 0), \tag{3.9}$$

with $|\boldsymbol{k}| = k_L = 2\pi/\lambda$. The polarization is pointing along the z-direction $\boldsymbol{e_s} = (0, 0, 1)$. Solving the spatially varying part with the plane waves

$$\frac{c\epsilon_0}{2} \left(\sum_{<i,j>}^{3} \left(E_i(\boldsymbol{r})^* E_j(\boldsymbol{r}) + c.c.\right) \right) \tag{3.10}$$

$$= \frac{c\epsilon_0}{2} \sum_{<i,j>}^{3} E_i E_j \cdot 2\cos\Big((k_j - k_i) \cdot \boldsymbol{r} + (\phi_j - \phi_i)]\Big) \tag{3.11}$$

$$= \sum_{<i,j>}^{3} \sqrt{4 I_i I_j} \cos\Big((k_j - k_i) \cdot \boldsymbol{r} + (\phi_j - \phi_i)]\Big) \tag{3.12}$$

we can define the lattice potential as the sum of three 1D-lattices of the form

$$V_{ij}(\boldsymbol{r}) = \sqrt{V_i V_j} \cos(\boldsymbol{b}_{ij} \cdot \boldsymbol{r} - \Delta\phi_{ij}) \tag{3.13}$$

with $V_i = -\kappa_{\text{dip}} 2 I_i$, $\Delta\boldsymbol{k_{ij}} = \boldsymbol{k_i} - \boldsymbol{k_j} = \boldsymbol{b_{ij}}$ and $\Delta\phi_{ij} = \phi_i - \phi_j$. Because the $\Delta\phi_{ij} = 0$ are defined cyclic the sum $\sum \Delta\phi_{ij} = 0$. A change in one ϕ_i will only result in a positional change of the lattice

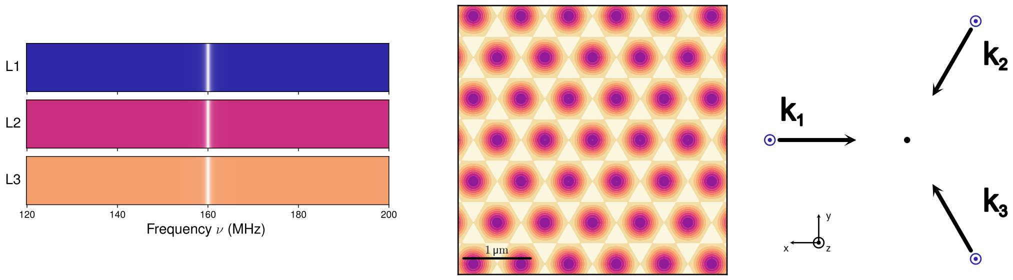

Figure 3.5: Interfering frequencies and triangular lattice potential. (Left) Same as in Fig. 3.3. For the triangular lattice setup, the double-pass AOMs are set to resonance at $160\,\mathrm{MHz}$ with respect to the frequency of the laser. (Middle) The resulting triangular lattice potential has a lattice spacing of $a_{\mathrm{lat}} = 709\,\mathrm{nm}$. (Right) The sketch shows the direction of the lattice beams with $\boldsymbol{k}_i$. At the crossing point in the center, the lattice is formed. All beams are s-polarized as indicated by the blue out-of-plane arrowhead at each beam.

in its 2D-plane, which will be visible in shot-to-shot fluctuations of the lattice position. This could be controlled by a phase lock between the three lattice beams.

If we set all beams to the same intensity, we get with $V_i = V_{\mathrm{lat}}$ the triangular lattice potential

$$V(\boldsymbol{r}) = 2V_{\mathrm{lat}} \sum_{i=1}^{3} \cos(\boldsymbol{b}_i \cdot \boldsymbol{r}) \ , \tag{3.14}$$

where we discarded the translating phase shifts. The reciprocal lattice vectors are given by

$$\begin{aligned} \boldsymbol{b_1} &= \boldsymbol{k_1} - \boldsymbol{k_2} = \sqrt{3}k_L(\sqrt{3}/2, 1/2, 0), \\ \boldsymbol{b_2} &= \boldsymbol{k_2} - \boldsymbol{k_3} = \sqrt{3}k_L(0, -1, 0) \text{ and} \\ \boldsymbol{b_3} &= \boldsymbol{k_3} - \boldsymbol{k_1} = \sqrt{3}k_L(-\sqrt{3}/2, 1/2, 0). \end{aligned}$$

The lattice depth will be given in units of the recoil energy $E_{\mathrm{rec}} = \hbar^2 k_L^2/2m = h \times 25.18\,\mathrm{kHz}$ of a laser photon at $\lambda = 1064\,\mathrm{nm}$. Another relevant energy scale will be the 1D lattice recoil energy, which will be noted as $E_{\mathrm{rec,\,lat}} = \hbar^2|\boldsymbol{b_i}|^2/2m = h \times 75.53\,\mathrm{kHz}$. The lattice constant for the two-dimensional hexagonal lattice is $a_{\mathrm{lat}} = 2/3 \times \lambda = 709\,\mathrm{nm}$. We also note the 1D lattice constant $a_{\mathrm{1D}} = \lambda/\sqrt{3} = 614\,\mathrm{nm}$, if only two of the beams interfere. With this, the absolute value of the reciprocal lattice vectors is given by $|\boldsymbol{b}_i| = 2\pi/a_{1D}$.

In addition to the bare interference of the three beams, our setup allows us to push intensity from the interfering part into non-interfering sidebands via the EOMs. The sidebands at $\Delta\nu_{\mathrm{EOM}} = \pm 10\,\mathrm{MHz}$, $35\,\mathrm{MHz}$ and $45\,\mathrm{MHz}$ will have no resonance with another direction and only contribute to the envelope potential as $V_{sb,i}(\boldsymbol{r}) \propto 2I_{sb,i}(\boldsymbol{r})$, where the factor two accounts for both positive and negative sidebands. The intensity per beam I_i is kept constant and is distributed between carrier and sidebands. The intensity is split like $I = I_c + 2\sum I_{sb,i}$ with $I_c = J_0(\alpha)I$ and $I_{sb,i} = 1/2 \cdot J_i(\alpha)I$. Here $J_i(\alpha)$ is the Bessel function of the first kind and α is the modulation index, which is tuned via the RF-power at the EOM. By keeping the overall intensity constant and only changing the modulation index of the EOM, we are able to keep the envelope potential almost the same while tuning the lattice modulation depth. Ensuring that the carrier intensities are equal, we can write the optical potential as

$$V(\boldsymbol{r}) = V_{\mathrm{trap}}(\boldsymbol{r}) + 2V_{\mathrm{lat}}(\boldsymbol{r},\alpha)\sum_{i}^{3}\cos(\boldsymbol{b}_i\cdot\boldsymbol{r}) \ . \tag{3.15}$$

Lattice loading The key components for the preparations of the lattice are the power of the three beams, the frequency of the AOMs and the modulation depth of the EOMs. In order to load the atoms into the lattice, we have to jump the frequencies of the AOMs to the resonance. To minimize the hard projection into a deep lattice, we use the EOMs to minimize the intensity at the carrier frequencies. During evaporation, we set the frequency difference to a conservative minimum of $\Delta\nu = 14\,\mathrm{MHz}$. This would enclose the sideband of the EOM with the lowest resonance frequency. To avoid jumping over this sideband and therefore being resonant for some finite time, we jump to an intermediate detuning of $8\,\mathrm{MHz}$, while the sidebands are still off. At the intermediate detuning, we increase the modulation index in $10\,\mathrm{ms}$ up to the zero-crossing of $J_0(\alpha_0) = 0$. At α_0, the carrier intensity is sufficiently suppressed, see figure 3.6. With almost no intensity in the carrier, we jump the frequencies to resonance. We now can choose a final trap frequency of the envelope potential by ramping up the overall power in the lattice beams. This seemingly acts as lattice loading, and we take care to be adiabatic, minimizing excitations. To reach a desired lattice depth the EOM modulation is reduced. The increased lattice modulation slightly increases the harmonic confinement, because the increasing modulation is proportional to the local intensity. An exemplary loading procedure is depicted in figure 3.6.

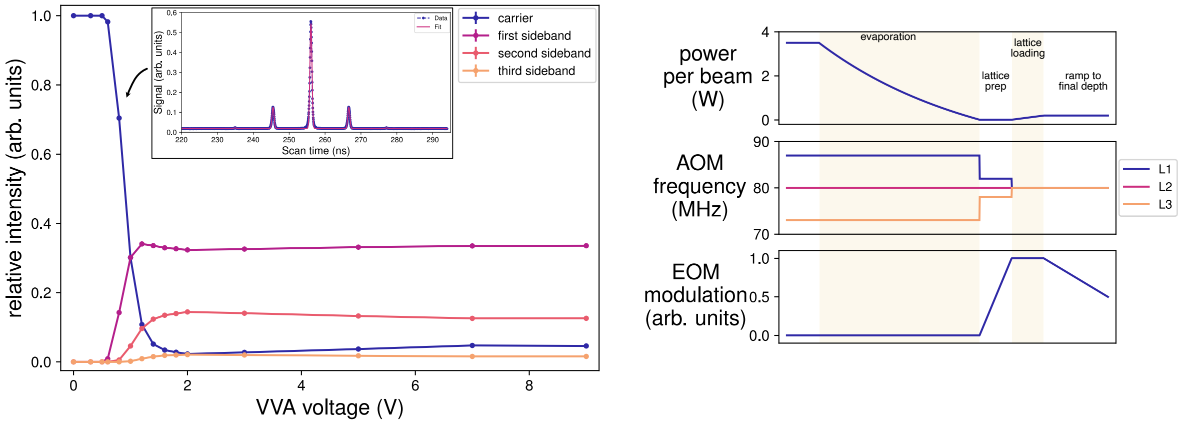

Figure 3.6: EOM sideband power and lattice loading sequence. (Left) Carrier-to-sideband ratios. The plot shows the measured ratios of the carrier and sideband after passing through the EOM. The EOM modulation is non-linear with voltage as well as the VVA. These data are for the L1 arm. The relative powers are extracted from a fit to Fabry-Perot cavity scans as shown in the inset. (Right) The lattice loading sequence. The EOM modulation is given from zero modulation to the modulation value, where the carrier is suppressed sufficiently. With the final value of the EOM modulation, the lattice depth is set. With a power of about $200\,\mathrm{mW}$ per beam, lattice depths of $V_{\mathrm{lat}} = 1.7\,E_{\mathrm{rec}}$ to $3.7\,E_{\mathrm{rec}}$ are typically realized.

We calibrate the lattice depth using Kapitza-Dirac measurements[74, 75]. Here we jump the AOM frequencies to the intermediate case, set the EOM modulation to its desired value, and ramp up the power of the dipole trap to a particular harmonic confinement and then instantly project onto the

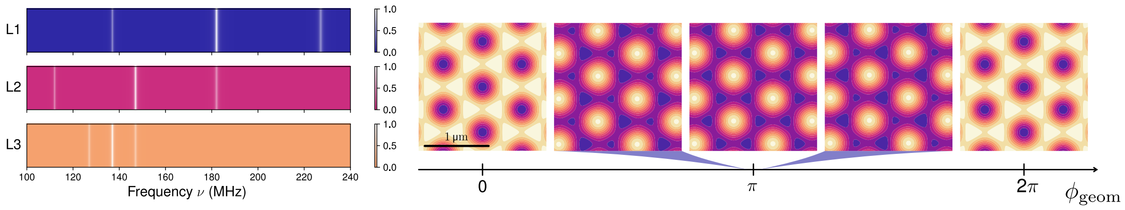

Figure 3.7: MFL frequencies and tunable geometry potential. (Left) Same as in Fig. 3.3. For the MFL lattice setup, the double-pass AOMs are set to $183\,\mathrm{MHz}$, $148\,\mathrm{MHz}$ and $138\,\mathrm{MHz}$ with respect to the frequency of the laser (brightest lines). The sidebands created by the EOMs are shown symmetrically around the carrier. One of them matches with the carrier of a different arm creating the 1D lattices. Note that the frequencies are selected such that no additional frequency is placed inside the range of the carriers. (Right) The resulting lattice potential when all three 1D lattices are enabled. By changing the RF-phase on the EOMs, the geometry of the lattice is changed. At $\phi_{\text{geom}} = 0$ and $\phi_{\text{geom}} = 2\pi$, a triangular lattice is created, whereas at $\phi_{\text{geom}} = \pi$, it is a honeycomb lattice. In the vicinity of the honeycomb lattice, a bi-partite lattice is realized with a potential offset between the two lattice sites, resembling a Boron-Nitride-like lattice.

lattice by switching the AOMs to resonance. Here we hold for up to a few microseconds before taking a time-of-flight image. During the short evolution in the lattice potential, the wavefunction of the BEC acquires local phases depending on the local potential depth and the duration of the pulse[76]. We perform this measurement for each 1D pair independently to ensure that the directions have the same lattice depth. With the oscillations of the Bragg peak intensities equalized for all beams, we take a final measurement to get the lattice depth in the triangular case. The EOMs are controlled via the VVA, and we find a functional dependence experimentally between control voltage and 1D-lattice depth.

Loading into the lattice potential can easily result in heating the cloud. We ramp adiabatically into the lattice in $10\,\mathrm{ms}$ and hold there for $5\,\mathrm{ms}$. By ramping into the lattice and back out again, we check that we do not excessively heat the sample. This confirms a good adiabatic loading of the lattice. The temperature at the end of the evaporation is at $108\,\mathrm{nK}$ (final power $16\,\mathrm{mW}$) and after ramping in and out we are in the same range or even colder. Note that due to three-body losses we cannot extend the duration in the lattice for much longer as we lose too many atoms, especially for deeper lattices.

We also ensure adiabaticity for ramping from the shallow lattice into the deep and back again with a similar procedure. We load the lattice to its initial depth of $1.7E_R$ and then ramp into deeper and deeper lattices. While increasing lattice depth we see the Bragg peak at $\hbar k_{\text{lat}}$ intensify first and then the whole distribution becomes Gaussian-like. The check for adiabaticity is that after ramping back out we again have a coherent sample, which is observed by the reappearing Bragg peaks and no significantly stronger thermal portion around zero momentum.

3.4 | Multi-frequency lattice

With the above, we are limited to a single geometry, although this in itself is highly interesting. We build the setup with more options in mind, namely the multi-frequency lattice, pioneered in [70]. This technique allows us to change the geometry even during the experimental cycle by only changing the phase of the EOMs RF source. The principle and the implementation of the multi-frequency lattice will be explained in the following.

From the equation 3.14, we know that three 1D lattices under $120°$ form a triangular lattice. This is already a special case of the more general hexagonal basis created by this geometry. The triangular lattice is the single-atomic basis. With the multi-frequency setup, we are able to change the geometry to a honeycomb lattice and intermediate geometries. In equation 3.14, the phases were coupled by $\Delta\phi_i = \phi_i - \phi_j$ and wouldn't allow for an independent change. With independent 1D-lattices added with the same lattice vectors, we can choose $\Delta\phi_i$ freely,

$$V(\boldsymbol{r}) = 2V_{\text{lat}} \sum_{i=1}^{3} \cos(\boldsymbol{b}_i \cdot \boldsymbol{r} + \Delta\phi_i). \tag{3.16}$$

As mentioned, two of those phases will result in translation of the lattice position, but this leaves one degree of freedom which is defined as the geometry phase ϕ_{geom}[70]:

$$\phi_{\text{geom}} = \sum_{i=1}^{3} \phi_i \tag{3.17}$$

Implementation To change the geometry, we implement the multi-frequency lattice from [70]. This scheme realizes three independent 1D lattices by matching a carrier of one arm with the sideband of the EOM on another arm. In particular, we use:

$$\nu_{\text{dA1}} = \nu_{\text{dA2}} + \nu_{0,\text{E2}} \tag{3.18}$$

$$\nu_{\text{dA2}} = \nu_{\text{dA3}} + \nu_{0,\text{E3}} \tag{3.19}$$

$$\nu_{\text{dA3}} = \nu_{\text{dA1}} - \nu_{0,\text{E1}} \tag{3.20}$$

With the EOMs at
$nu_{0,\text{Ei}} = 45\,\text{MHz},\ 35\,\text{MHz}$ and $10\,\text{MHz}$, we set the doubles-pass frequencies to
$nu_{\text{dAi}} = 183\,\text{MHz},\ 148\,\text{MHz}$ and $138\,\text{MHz}$, which corresponds a radio frequency input of
$nu_{\text{Ai}} = 91.5\,\text{MHz},\ 74\,\text{MHz}$ and $69\,\text{MHz}$ to the AOMs (Fig. 3.7). This gives approximately the same efficiency for the AOMs as they are about the same distance from the optimal setting at $160\,\text{MHz}$.

With the matter-wave microscope, we are able to image the triangular lattice as well as the honeycomb lattice, see figure 3.8. We also check the ability to change the geometry in momentum space by performing Kapitza-Dirac measurements. The single 1D lattices with their independent phases imprint those onto the wave function, creating a momentum space lattice with a staggered flux[70]. This creates an imbalance between the population at the positive and negative first-order Bragg peaks,

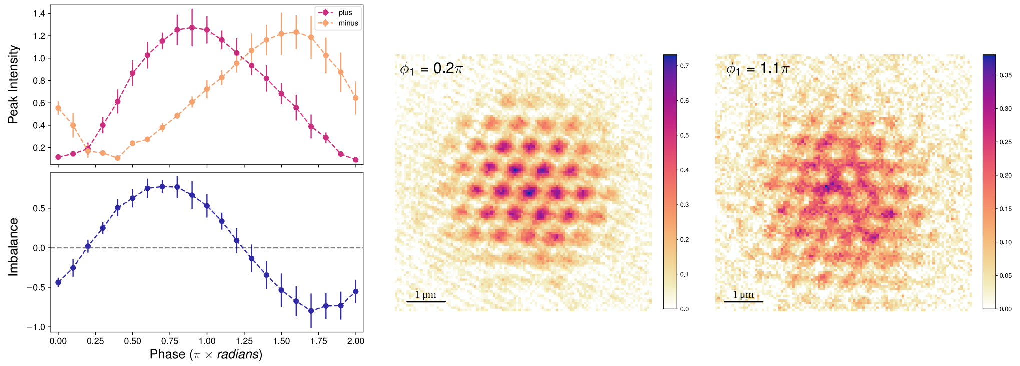

Figure 3.8: KD measurement of staggered flux and matter-wave images. (Left) We measure the imbalance between the population at positive and negative first-order Bragg peaks (lower panel). We observe the imbalance oscillate with the geometry phase. We attribute the non-π phase shift between the two components (upper panel) to not-optimally equalized 1D lattice depth of the three separate axes. The two zero crossings in the imbalance are the triangular and honeycomb configurations. The former is at $\phi_1 \approx 0.2\pi$ and the latter at $\phi_1 \approx 1.1\pi$, where ϕ_1 is the RF-phase on EOM1. The two matter-wave images are taken at these positions. The triangular case is exceptionally easier to prepare and magnify, thus showing a clear triangular density modulation. For the honeycomb lattice, a slight mismatch between the two sites is easily created, and additionally, with the effectively shallower lattice, the imaging has to be adapted. More fine-tuning will be needed for a clear picture of the two sub-lattice sites as in [21]. All images of the atomic density in this thesis are obtained through a defringing algorithm as in [77].

see figure 3.8. With this we showed, that the multi-frequency setup is working in our setup and can be used for future experiments. We note that the populations are not fully in phase and attribute this to not yet perfectly calibrated lattice depth for the multi-frequency setup. This also makes imaging a magnified honeycomb lattice difficult. The multi-frequency setup will eventually allow us to work with honeycomb and boron-nitride-like lattices with dynamical control and probe the density in higher bands. We will image the in-situ densities utilizing the matter-wave microscope.[2]

3.5 | Moving lattice

The versatile lattice setup enables us to create controlled running waves in the multi-frequency setup as well as the triangular setting in a well-controlled manner. The lattice potential given in eq. 3.14 becomes time-dependent,

$$V(\boldsymbol{r},\boldsymbol{t}) = 2V_{\mathrm{lat}} \sum_{i=1}^{3} \cos(\boldsymbol{b}_i \cdot \boldsymbol{r} - \Delta\omega_i t) \ , \tag{3.21}$$

where we introduced $\Delta\omega_i = \omega_i - \omega_{i+1}$ as the frequency difference between the lattice beams. The slight difference in frequency can be neglected with regard to the lattice constant. As a first measurement with the moving lattice, we prepare a 1D lattice by detuning one of the beams off resonant to the others, e.g. by $1\,\mathrm{MHz}$ or $8\,\mathrm{MHz}$. With these detunings, we expect no movement in the off-axis direction, i.e. by the fast running waves. The radial confinement in this setting has a trap

---

[2] The matter-wave microscopy will be explained in the following chapter.

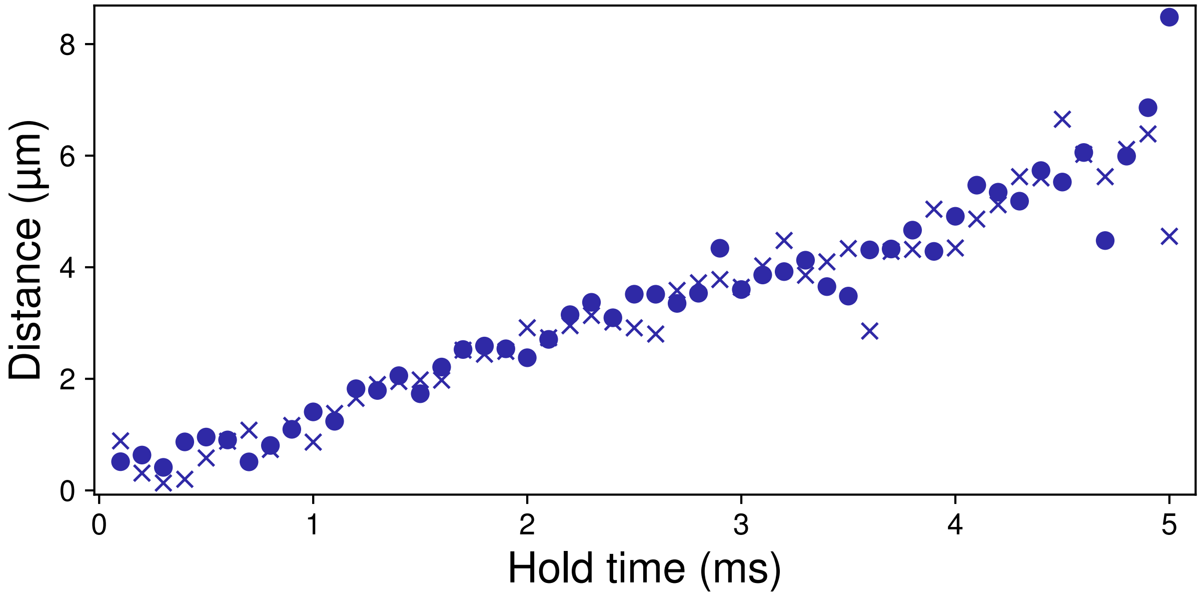

Figure 3.9: Position in moving lattice. We extract the position of the cloud by fitting a 2D Gaussian distribution. The relative distance is with respect to the center of the image, matching the initial position of the cloud. The distances are given in-situ and are along the moving direction of the lattice. We see the cloud dragged along with the lattice moving with $2\,\mathrm{kHz}$. The center of mass movement has a step-like behavior. We do not observe a significant difference between the two described cases, where the third beam is detuned by $1\,\mathrm{MHz}$ (dots) and $8\,\mathrm{MHz}$ (crosses).

frequency of only $\omega_r \approx 2\pi \times 0.8\,\mathrm{kHz}$. The onsite trap frequency of the 1D lattice with $V_{\mathrm{lat}} = 4\,E_{\mathrm{rec}}$ is $\omega_{\mathrm{onsite}} \approx 2\pi \times 100\,\mathrm{kHz}$.

After the 1D lattice is loaded, we move the cloud by switching the frequency on L1 by $\Delta\omega_{\mathrm{mov},1} = 2\pi \times 2\,\mathrm{kHz}$. We let the system evolve under this running wave for a time t_{mov} and take a matter-wave microscope image at the end. Example images are shown in fig. 3.10, where we observe two things: First, as expected, the cloud is pulled along by the moving lattice, as can be seen in the images and the change in relative distance (Fig. 3.9, position extracted from fitted Gaussian envelope). Over the duration of $5\,\mathrm{ms}$, the cloud is moved by approximately $6\,\mu\mathrm{m}$, i.e. about 10 lattice sites, which matches very well to the ten oscillations during that duration. Looking closely at the increase in relative distance, the center of the Gaussian distribution appears to increase step-like. Confirmation of this effect would need more statistics, although it might manifest in the second observation as well. The second observation is a density modulation appearing on top of the lattice structure right after the start of the translation. This additional modulation is visible as an increased spectral power between the Bragg peaks and the zero momentum peak in the Fourier transform (Fig. 3.10). The additional density modulation could be a similar effect as seen in [77]. In their case a strong tilt of $2\,\mathrm{kHz}$ in the confining potential created the spontaneous density modulation. Here we move the cloud up a harmonic potential, reaching similar gradients to the end. The density pattern appears directly, whereas in [77] it took time to build up.

Another, rather intriguing feature is the appearance of a modulation perpendicular to the moving direction when the off-resonant beam is detuned by only $1\,\mathrm{MHz}$ instead of $8\,\mathrm{MHz}$. This modulation appears to have a modulation period matching those of a 2D triangular lattice. This can be seen in the appearance of the Bragg peaks corresponding to the other two lattice directions. The contrast between the two detunings can be nicely seen from the averaged magnitude of the Fourier transformed images. While in the far detuning, no additional Bragg peaks appear, they are strongly visible in the nearer detuned case. The intriguing part is that the interference with the third beam should be averaged out because all other (onsite) trap frequencies are smaller by order(s) of magnitude. It would be highly interesting to study this effect further and to see how the lattice momenta of the other two running waves couple to the condensate.

3.6 | Band structure

The dispersion relation of a free particle is modified by the periodic potential described in the previous section. The periodicity of the potential also introduces a periodicity in the solution of the Schrödinger equation, which is the well-known Bloch theorem[78]. For a periodic potential, the Schrödinger

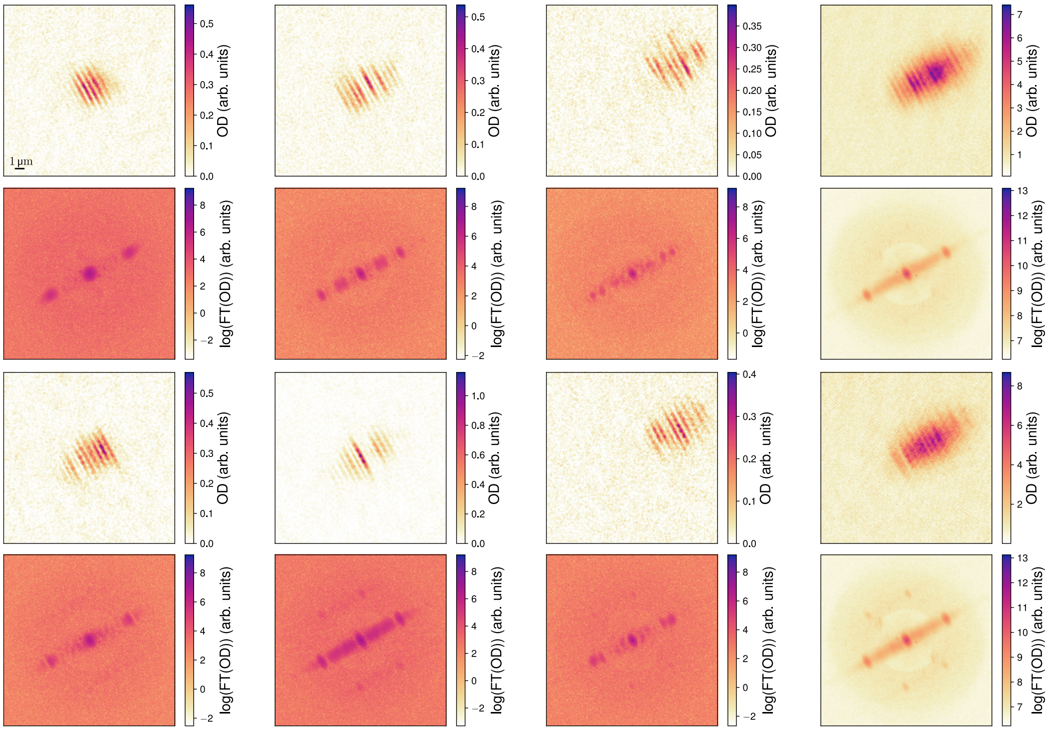

Figure 3.10: Matter-wave images of the moving cloud and their Fourier transform. The first three columns are matter-wave images and their Fourier transformation taken after $0.1\,\mathrm{ms}$, $0.3\,\mathrm{ms}$ and $4.6\,\mathrm{ms}$ of lattice movement. The last column is averages over all times measured presented in figure 3.9. The upper rows show data where the third beam is detuned by $8\,\mathrm{MHz}$, the lower the smaller detuning of $1\,\mathrm{MHz}$. In both cases, an additional density modulation along the lattice direction appears as soon as the cloud starts to move. This modulation is not constant, which leads to a smeared-out signal in the averaged Fourier image between the Bragg peaks of the present 1D lattice. Intriguingly, in the less detuned case, additional modulation appears with a reciprocal lattice vector matching those of the hexagonal lattice for all three beams, i.e. modulation perpendicular to the lattice movement. The clear feature remaining in the averaged signal of the Fourier transform shows that this modulation is present during the whole movement.

equation takes the form

$$H\psi_{\boldsymbol{q}}^{(n)}(\boldsymbol{r}) = E_{\boldsymbol{q}}^{(n)}\psi_{\boldsymbol{q}}^{(n)}(\boldsymbol{r}) \text{ with } H = \frac{p^2}{2m} + V(\boldsymbol{r}). \tag{3.22}$$

The solution is given by the Bloch wavefunctions

$$\psi_{\boldsymbol{q}}^{(n)}(\boldsymbol{r}) = e^{i\boldsymbol{q}\boldsymbol{r}/\hbar}u_{\boldsymbol{q}}^{(n)}(\boldsymbol{r}). \tag{3.23}$$

The wavefunction is described by the quasi-momentum q, which is defined in the first Brillouin zone, $q \in [-\hbar b, \hbar b]$, and the energy band n. The eigenvalues of the system $E_{\boldsymbol{q}}^{(n)}$ describe the energy bands in momentum space. The eigenvectors give the Bloch coefficients defining the wavefunction. We use the code from [73] to compute the band structure for the triangular lattice. We perform the band structure calculation up to the maximal lattice depth $V_{\text{lat}} = 3.7\,E_{\text{rec}}$ used in the following chapters. From the band structure, we deduce the bandwidth, which gives us the strength of the single-particle tunneling element K (Fig. 3.11).

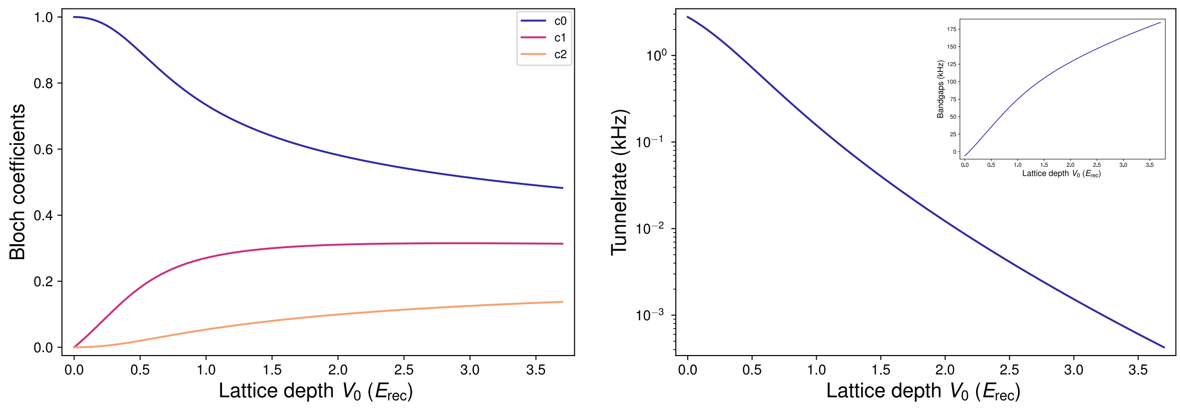

Figure 3.11: Bloch coefficients and tunneling rate. (Left) We plot the Bloch coefficients extracted from the band-structure calculation. (Right) Here we plot the tunneling rate calculated from the bandwidth and the inset shows the band gap between the first and second band of the triangular lattice.

Conclusion & Outlook

In this chapter, we presented our versatile lattice setup for a hexagonal lattice configuration. The setup features the possibility not only to create dynamically tunable geometries but also to effectively remove the lattice modulation by detuning the single arms far enough, such that the resulting potential is averaged to a bare dipole trap potential. The ability to switch between these configurations allows us to image the system with matter-wave microscopy, while using the same beam configuration. In addition to the static lattice potentials realized, it is possible to create "slow" running waves to study dynamical systems of the lattice potential, which can exhibit interesting phenomena as found in our preliminary measurements. With the multi-frequency setup in particular, it will be possible to excite the system to higher bands, and with the imaging capabilities of the matter-wave microscope, it will be intriguing to push towards imaging of the density orbitals. Eventually, imaging, for example, the p-band orbital and its hybridization in interacting systems[79].

CHAPTER 4

Coherence magnifier

The coherence of a quantum mechanical system is one of its most fascinating features. With the observation of interference patterns of two BECs[24], the coherent nature of matter-waves was proven for ultra-cold atomic gases and has been used as tool, e.g. to probe phase transitions[32]. In this chapter, we introduce matter-wave microscopy, which magnifies the atomic wavefunction and enables us to image the density with single-site resolution[21]. Using an optical matter-wave lens, we magnify a coherent wavefunction released from the lattice potential described in the previous chapter. The coherence of the system, in combination with a periodic density modulation, results in a self-imaging effect of the lattice potential, the Talbot effect[26]. We show the first in-situ images of the two-dimensional matter-wave Talbot effect. By resolving the self-imaged structure, we get a measure for the coherence between lattice sites. The number of self-images, called revivals, depends on the coherence of the system[80]. We utilize this tool to probe the loss of coherence while crossing the critical point of the Berezinskii-Kosterlitz-Thouless (BKT) transition[33, 34]. This chapter will provide a description of the matter-wave microscope based on the averaged optical potential discussed in the previous chapter. We outline the theoretical framework and the experimental implementation. We introduce the Talbot effect and the measurements of the in-situ density for both a 1D and 2D Talbot effect. Additionally, we present a measurement of the optical Talbot effect, created by the magnified density and the coherent absorption light. Finally, we present the measurement of the BKT-transition, at which point we see the Talbot revivals vanish drastically[23].

4.1 | Matter-wave microscope

The matter-wave microscope is a powerful tool to gain insights into the many-body wavefunction by magnifying the atomic wavefunction prior to imaging. It has been just recently established [21] for lattice and as of writing this thesis extended to single-atoms from a few-atom, bulk system[22]. We adapted it in our system during this thesis. Here we will recap the method and describe our implementation, see also [36].

The working principle of the matter-wave microscope is based on two Fourier transformas from real space to momentum space and back again, see figure 4.1. At the end of an experimental sequence, the atoms are subjected to a harmonic potential with trap frequency ω, where they evolve for a quarter period $T_4 = 2\pi/4\omega$. All kinetic energy will be transferred to potential energy, and vice versa.

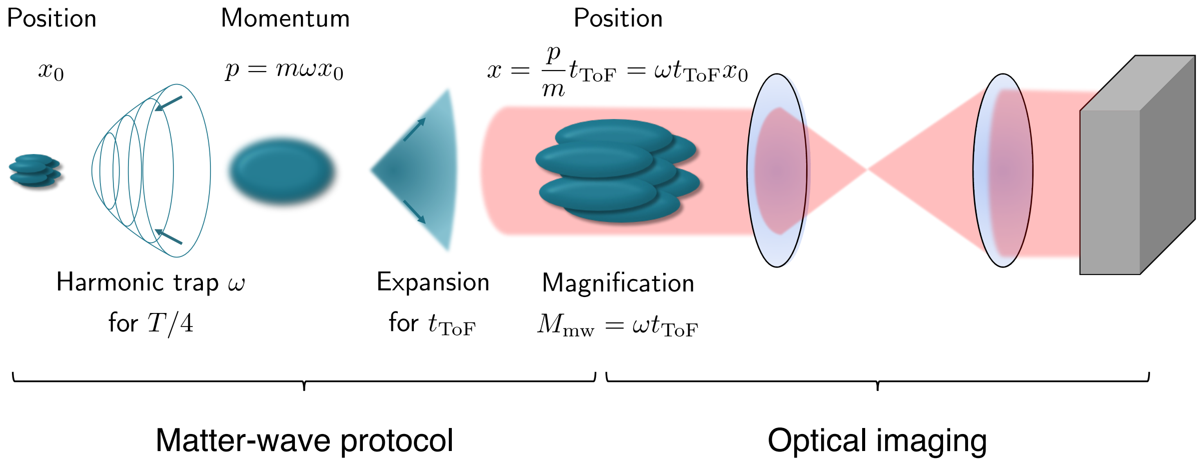

Figure 4.1: Matter-wave microscope protocol. The density distribution evolves first in a harmonic trap with the trap frequency ω. After a quarter period, the wavefunction is transformed to momentum space. At this point, the potential is switched off, and a free expansion, time-of-flight, for t_{ToF} follows. This Fourier-transforms the wavefunction again and brings it back to position space. These two steps result in a magnification $M_{\mathrm{mw}} = \omega t_{\mathrm{ToF}}$ of the initial density distribution. This magnified density distribution is then optically imaged, where additionally optical magnification is possible. (Figure adapted from [36])

In particular, if we started with a particle at a position x_0 and for simplicity, no kinetic energy. After a quarter period, this particle would be at the center of the trap $x = 0$ with an acquired velocity of $v = -\omega x_0$. Taking an image at this point would resolve the momentum distribution of the atoms and has been used as a technique with high-resolution imaging [81, 82]. A more common technique of capturing the momentum space is a free expansion, or time-of-flight (TOF), at the end of the experimental cycle[83]. Like in optics, a free expansion will approximate a Fourier transform if taken to the far-field limit. In the matter-wave microscope protocol, the harmonic confinement is turned off after the quarter period evolution, and a time-of-flight is used to transfer the wavefunction back to real space. As the trap is turned off, the particle will travel with its final velocity, and after a time t_{ToF}, it is at a new position given by $x = -\omega t_{\mathrm{ToF}} x_0$. The distance to the trap center is magnified by $M = |-\omega t_{\mathrm{ToF}}|$. This results in a magnification of the full atomic distribution, which is then imaged.

4.1.1 Theoretical description of the matter-wave lens

In experiments with ultra-cold atoms, the velocity distribution of the wavefunction of interest will also differ from $v = 0$. Especially, in lattice experiments, we expect to observe the momenta of the Bragg peaks. We therefore have to make sure that we reproduce the initial density while allowing initial velocity. We derive this focusing condition in the Heisenberg picture. Note that a description in the Schrödinger picture is also possible and allows us to show that the protocol also recovers correlations of the system [21]. We will illustrate the derivation in the 1D case, but it can be easily generalized to 2D or 3D. The Hamiltonian of a particle with mass m in harmonic confinement with a trap frequency

ω is the following:

$$\hat{H}_{\mathrm{ho}} = \frac{\hat{p}^2}{2m} + \frac{m\omega\hat{x}^2}{2}, \tag{4.1}$$

with the position operator $\hat{x}$ and the momentum operator $\hat{p}$. The equations of motion for this Hamiltonian are

$$\partial_t\hat{x} = \frac{i}{\hbar}\left[\hat{H}_{\mathrm{ho}}, \hat{x}\right] = \frac{\hat{p}}{m} \tag{4.2}$$

$$\partial_t\hat{p} = \frac{i}{\hbar}\left[\hat{H}_{\mathrm{ho}}, \hat{p}\right] = -m\omega^2\hat{x}. \tag{4.3}$$

The solution for a particular evolution time t_{ho} in the harmonic oscillator can be found to be

$$\hat{x}(t_{\mathrm{ho}}) = \hat{x}(t_{0,\mathrm{ho}})\cos(\omega t_{\mathrm{ho}}) + \frac{\hat{p}(t_{0,\mathrm{ho}})}{m\omega}\sin(\omega t_{\mathrm{ho}}) \tag{4.4}$$

$$\hat{p}(t_{\mathrm{ho}}) = \hat{p}(t_{0,\mathrm{ho}})\cos(\omega t_{\mathrm{ho}}) - m\omega\hat{x}(t_{0,\mathrm{ho}})\sin(\omega t_{\mathrm{ho}}), \tag{4.5}$$

depending on the initial position and momentum operators $\hat{x}(t_{0,\mathrm{ho}})$ and $\hat{p}(t_{0,\mathrm{ho}})$. For a quarter period, this will result in

$$\hat{x}(t_{\mathrm{ho},4}) = \frac{\hat{p}(t_{0,\mathrm{ho}})}{m\omega} \tag{4.6}$$

$$\hat{p}(t_{\mathrm{ho},4}) = -m\omega\hat{x}(t_{0,\mathrm{ho}}) \ . \tag{4.7}$$

The free evolution during the time-of-flight has just $H = \hat{p}/2m$ which gives $\dot{x} = \hat{p}/m$ and $\dot{p} = 0$. The operators then evolve as $x(t) = \hat{p}(t_{0,\mathrm{ToF}})/m \cdot t + \hat{x}(t_{0,\mathrm{ToF}})$ and just $\hat{p}(t) = \hat{p}(t_{0,\mathrm{ToF}})$, where $\hat{x}(t_{0,\mathrm{ToF}})$ and $\hat{p}(t_{0,\mathrm{ToF}})$ are the initial operators. Setting $\hat{x}(t_{0,\mathrm{ToF}}) = \hat{x}(t_{\mathrm{ho},4})$ and $\hat{p}(t_{0,\mathrm{ToF}}) = \hat{p}(t_{\mathrm{ho},4})$ we arrive at

$$\hat{x}(t_{\mathrm{ho},4} + t_{\mathrm{ToF}}) = -\omega t_{\mathrm{ToF}}\hat{x}(t_{0,\mathrm{ho}}) + \frac{\hat{p}(t_{0,\mathrm{ho}})}{m\omega} \tag{4.8}$$

$$\hat{p}(t_{\mathrm{ho},4} + t_{\mathrm{ToF}}) = -m\omega\hat{x}(t_{0,\mathrm{ho}}) \ . \tag{4.9}$$

Note the derived magnification factor $M = |-\omega t_{\mathrm{ToF}}|$, which we already got through the simple example above. For $t_{\mathrm{ToF}} \gg \hat{p}(t_{0,\mathrm{ho}})/(m\omega^2\hat{x}(t_{0,\mathrm{ho}}))$ we can neglect the initial momentum contribution and get a focused image of the initial density in the actual far-field version of the matter-wave microscope. For our experimental parameters this would refer to $t_{\mathrm{ToF}} \gg 2.3\,\mathrm{ms}$, where we used $p_0 = \hbar k_{latt,1D}$ and $x_0 = a_{latt,2D}$. This limit is difficult to reach as the signal-to-noise ratio would drastically decrease with decreasing atomic density and we would not be able to distinguish signal from background anymore. Fortunately, other focusing conditions can be found where the initial momentum contribution vanishes. By not working directly at $T/4$, essentially overshooting, the initial momentum contribution can be compensated. By using $\hat{x}(t_0) = \hat{x}(t_{\mathrm{ho}})$ and $\hat{p}(t_0) = \hat{p}(t_{\mathrm{ho}})$, the position operator after TOF has the following form:

$$\hat{x}(t_{\mathrm{ho}} + t_{\mathrm{ToF}}) = \frac{1}{m}t_{\mathrm{ToF}}(\hat{p}(t_{0,\mathrm{ho}})\cos(\omega t_{\mathrm{ho}}) - m\omega\hat{x}(0)\sin(\omega t_{\mathrm{ho}})) \tag{4.10}$$

$$+ \hat{x}(0)\cos(\omega t_{\mathrm{ho}}) + \frac{\hat{p}(0)}{m\omega}\sin(\omega t_{\mathrm{ho}}) \ . \tag{4.11}$$

The initial momentum is canceled for

$$t_{\mathrm{ToF}} = -\frac{1}{\omega}\tan(\omega t_{\mathrm{ho}})\ , \tag{4.12}$$

with which the position operator becomes

$$\begin{aligned} \hat{x}(t_{\mathrm{ho}} + t_{\mathrm{ToF}}) &= (\tan(\omega t_{\mathrm{ho}})\sin(\omega t_{\mathrm{ho}})) + \cos(\omega t_{\mathrm{ho}}))\hat{x}(0) && (4.13)\\ &= \hat{x}(0)\sqrt{1+\tan(\omega t_{\mathrm{ho}})^2} && (4.14)\\ &= \hat{x}(0)\sqrt{1+(-\omega t_{\mathrm{ToF}})^2} && (4.15)\\ &= \hat{x}(0)\sqrt{1+M^2}\ . && (4.16) \end{aligned}$$

The magnification in the matched focusing condition is given by $M' = \sqrt{1+M^2}$. For large enough $\omega t_{\mathrm{ToF}} \gg 1$, this simplifies to $M' \approx M = \omega t_{\mathrm{ToF}}$ again.

4.1.2 Optical matter-wave lens

The matter-wave lens in our setup is created by the optical potential of the three intercepting laser beams. Here we use the non-interfering setting, described in section 3.2. At the end of the lattice experiment, we jump the three driving frequencies of the AOMs out of resonance and let the cloud evolve in the remaining potential. Usually, the frequencies are switched to $\nu_{AOM,i} = 74\,\mathrm{MHz},\ 86\,\mathrm{MHz}$ and $80\,\mathrm{MHz}$. Note that we choose to jump AOM L2 instead of AOM L3. When jumping AOM L3, we observed a drop in intensity on the monitor PD of the respective path. Using AOM L2, we reduce this intensity drop, ensuring a sufficiently isotropic intensity evolution at all times. Finally, the optical potential is switched off entirely, and we perform the needed free expansion to image in the spatial domain. In the following, we will discuss the crucial settings to realize a matter-wave microscope with an optical potential.

Interaction During the magnifying protocol, high-density regions are possible, especially when releasing a coherent system from a shallow lattice. Here, the density will peak at the lattice momenta when reaching the momentum space intermittently. The interaction at these high-density points leads to density dependent mean-field lensing, which introduces aberration in to the matter-wave lens. With this, it is not possible to resolve the lattice structure properly, see figure 4.2. In the initial matter-wave microscope, the wavefunction had to be made incoherent to circumvent these interaction effects [21] as the interaction is effectively fixed in ^{87}Rb by the constant scattering length $a_s \approx 100 a_0$. To remove the coherence of the system, the lattice depth was ramped up until tunneling is highly suppressed, and each tube evolves independently. This eventually results in independent BECs per tube with no inter-tube coherence. Without the coherence, the high densities at the lattice momenta are removed and a Gaussian density distribution remains in the momentum space. This technique allowed the magnifying technique to work, but at the cost of the loss of potential access to the system's coherence, which is of high interest for quantum mechanical systems. Here, we solve this issue by utilizing the Feshbach resonance present in Lithium. The evaporation takes place at $a_s = 76 a_0$ $(B = 720\,\mathrm{G})$. The resulting density without changing the magnetic field is shown in figure 4.2, where a periodic structure is barely visible, if at all. By ramping down the magnetic field towards

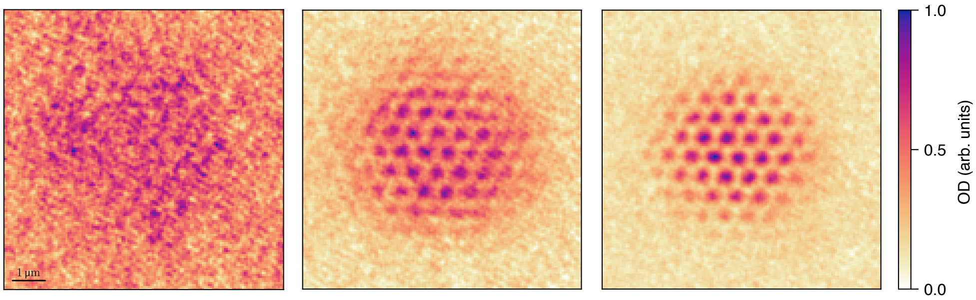

Figure 4.2: Interaction effect on the matter-wave lens. Magnified densities at different interaction. The image on the left shows the density taken at a scattering length of $76.1\,\mathrm{a}_0$ ($702\,\mathrm{G}$). Here, no lattice structure is visible. As we reduce the interaction by setting the magnetic field closer to the zero crossing, we are able to increase the lattice contrast. For $31.5\,\mathrm{a}_0$ ($670\,\mathrm{G}$, middle), a lattice structure becomes visible, and a sharp lattice is captured at $31.5\,\mathrm{a}_0$ ($610\,\mathrm{G}$, right). In all other experiments, we reduce the interaction further to a scattering length of $3.5\,\mathrm{a}_0$ ($580\,\mathrm{G}$).

the zero-crossing of the Feshbach resonance at $B = 543\,\mathrm{G}$, we can sufficiently suppress the interaction. Working at a magnetic field of $B = 560\,\mathrm{G}$, we have a scattering length of $a_s = 3.5a_0$. With this low interaction, we are able to resolve the lattice structure very clearly, while also maintaining coherence throughout the whole process. The lattice-resolved density is shown in figure 4.2.

Trap frequency and timing With the optical matter-wave lens, a sufficiently high trap frequency is necessary. The optical potential is created by the Gaussian beams and is approximately harmonic only for a small part in the center of the beam. During the magnifying protocol, the density may also probe the areas outside this harmonic region, which will lead to deviations from the focusing condition and strong aberrations. Assuming a harmonic potential, the relevant first lattice momentum will be at $x_k = \hbar k/m\omega_0$ after the quarter period. The main deviation from the harmonic potential is the next higher order in the expansion, the quartic term. The quadratic term is proportional to $1/w_0^2$ and the quartic term to $1/w_0^4$, the latter having the opposite sign to the former. For the harmonic approximation to be valid, we want $x_k < x_c = w_0$ and with that, $\omega_0 > \hbar k_{latt,1D}/mw_0$. For the system parameters, the trap frequency should be larger than $\omega_c = 2\pi \times 351\,\mathrm{Hz}$. For trap frequencies above ω_c, the quartic potential is less dominant, but still present. The boundaries are also discussed in [22]. The resulting aberration will be discussed in more detail in section 5.2. We choose a safety factor of about four, which reduces the contribution of the quartic potential to below $10\,\%$ and allows us to properly image the magnified density distribution. With a trap frequency of $\omega_0 = 2\pi \times 1.2\,\mathrm{kHz}$, the Bragg peak would have a distance of $\Delta x_k = 12.3\,\mathrm{\mu m}$ to the zero momentum peak, which would allow for selective manipulation with high-NA objectives, like phase imprinting or Fourier filtering. In an ideal case, we would instantly change the trap frequencies after turning off the lattice. This step-function is very difficult to follow for the power locking electronics. During the lattice, we work with about $500\,\mathrm{Hz}$ in the radial plane, which is about $200\,\mathrm{mW}$ per beam. Setting the lock point for the power instantly to $1\,\mathrm{W}$, we see a fast ramp in the beginning and oscillation at the final value compensating for the overshoot of the lock. We are able to obtain images of the lattice density, but without precise control over the intensity. A precise control over the evolution time and the trap frequency during magnification is necessary as later in the Talbot measurement, otherwise the calibration becomes impossible. The necessity of precise control of the trap frequency also deemed another approach infeasible, where we switched the RF-source from the closed-loop to an open-loop with a pre-set power. Here, we encountered fluctuations in the power which would lead to deviations in the $T/4$-time on the order of μs, which is the range of the expected signals. Fortunately, the magnifying protocol is not restricted to instant changes of trap frequency but allows for continuous ramps[84]. The effective frequency will then be th integrated trap frequency performing a Fourier transform after an effective $T/4$-time. We find a controlled ramp of $50\,\mu s$ to work well. This creates an image around $T_4 = 200\,\mu s$. The exact time depends on the current calibration and even in the almost non-interacting case on the interaction, and with that the coherence of the system. A last note on timing, the control system of the experiment has a maximum output frequency of $1\,\mathrm{MHz}$ in the analog and digital channels. We find the smallest slot length of $1\,\mu s$ is just short of the needed resolution. We extend this resolution to the sub-microsecond range by utilizing the home-built RF-source (dAOM), which exhibits a programmable real-time unit. The smallest time-step possible is $10\,\mathrm{ns}$. With the combination of the ADwin and the dAOM, we realize a resolution of $250\,\mathrm{ns}$ at the end of the ramp, while deviating the TOF duration only $0.75\,\mu s$, which is negligible compared to the $5\,\mathrm{ms}$ duration. This high timing resolution made us aware of a slight deviation of the turn-off time between the beams on the order of a few hundred nanoseconds. We find this to be a delay due to the electronics, although they are identical on each path. We compensate for this by adding delay lines by means of coaxial wire.

Isotropy Another factor for a clearly resolved lattice structure is the radial isotropy of the optical potential. An initial optimization is already done by overlapping the beams to the sub-micrometer scale. We find that this is not sufficient yet. To optimize the isotropy further, we utilize the matter-wave Talbot effect, which we observe when releasing the atoms from the lattice potential. The matter-wave Talbot effect will be discussed in the following section, and the calibration method explained. With this, we get a very good isotropy of the matter-wave lens.

Trap aberrations The ideal case of a matter-wave magnification setup is two consecutive clean harmonic potentials. Replacing the second harmonic evolution with a free expansion introduces no significant aberration, only the momentum will pick up slight deviation when calibrated carefully. Deviations from the harmonic potential, e.g. to a Gaussian potential, will lead to aberration effects picked up during the evolution in this trap. This sets limits on the resolvable structures and imageable system size. In our case, the matter-wave lens is created by the three Gaussian laser beams, resulting in an overall Gaussian potential. The first-order deviation from the harmonic potential is the quartic term of the Gaussian profile given by the waist of the beam w_0. We will discuss the difference in evolution in more detail as it will allow us to extend our measurement capabilities beyond density observables.

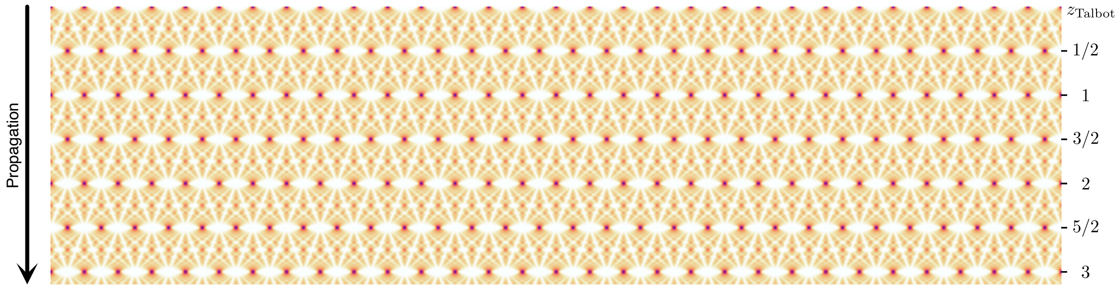

Figure 4.3: Talbot carpet. The Talbot effect in 1D creates self-images of the initial grating at multiples of z_{Talbot}, the primary revivals. In between the periodic structure, revivals occur but shifted by half the period, the secondary revivals. Depending on the slit width and the wavelength of the wavefunction, higher-order revivals may appear as seen here in between a primary and secondary revival. These have a periodicity which is an even factor higher than the original one. The evolution of the intensity distribution is known as the Talbot carpet.

4.2 | Talbot effect

The Talbot effect is an intrinsically coherent effect. First observed in optics by Henry Fox Talbot in 1836 [26] and later further studied by Lord Rayleigh [85]. The Talbot effect takes place when coherent light is scattered off a grating. Behind the grating, the emitted Huygens waves interfere and, in the far field, form the known diffraction pattern. In the near field, directly after the grating, the waves self-image the grating's structure. An image of the grating is formed after the so-called Talbot length $z_{\mathrm{Talbot}} = 2d^2/\lambda$, with the slit period d and the wavelength of the light illuminating the grating λ. This relation holds for $\lambda \ll d$. Keeping the introduction to 1D, one can see a second image of the grating between it and the first primary Talbot revival, the secondary revival at $z_{\mathrm{Talbot}}/2$. It has the same periodicity and images the grating, with one particular feature: that it is shifted by half a period. Besides full revivals, there can be structures with higher periodicity in n-multiples of the original period, the so-called fractional revivals. Solving the Fresnel integral for the near field, one gets the so-called Talbot carpet as in figure 4.3. The structure repeats itself multiple times depending on the system size.

The Talbot effect is also known in matter-wave optics. The coherent nature of quantum particles made it possible to observe the Talbot effect with atoms [27, 28], electrons [29], molecules [30], and plasmons [31]. This being a non-extensive list. With early experiments studying the Talbot effect with atoms, it has been the point of interest for multiple cold atom experiments, showing the effect of the reviving periodicity in 1D [28, 86], measuring coherence by Bragg scattering from the self-imaged density [87], or by releasing and recapturing the reviving density pattern with the lattice itself [80, 88]. Here we build on this pioneering and fascinating work, by showing the reviving density of a 2D triangular lattice structure. The near-field evolution is imaged in situ with the matter-wave microscope. This allows us for the first time to measure the in-situ density distribution of the 2D Talbot revivals of ultra-cold atoms released from a 2D lattice. We are also able to measure the 1D Talbot effect[89], which we extensively use to calibrate our system to high isotropy. We will first discuss the matter-wave Talbot effect in 1D and show measurements as well in 2D. In section 4.2.2, we will recap the optical Talbot effect as it is also present when imaging the atoms with coherent light. Finally, we will discuss measurements across the BKT phase transition by increasing the lattice depth. With deeper lattices, we observe a decrease in visible Talbot revivals.

4.2.1 Matter-wave Talbot effect

With the ability to keep the system coherent during the matter-wave protocol, the wavefunction released from the lattice undergoes Talbot revivals. We measure the matter-wave Talbot effect in the time-domain, i.e. we measure revivals at multiples of the Talbot time T_{Talbot}. With ultra-cold atoms in optical lattices, we can model each lattice site as an emitter in the plane wave basis. Upon release from the lattice, the dynamics are governed by the kinetic energies, namely the recoil energy of the corresponding modulation, $E_{\mathrm{rec}} = \hbar^2 k^2/(2m)$. Taking the inverse of the recoil frequency $\nu_{\mathrm{rec}} = E_{\mathrm{rec}}/h$, we get the Talbot time [90],

$$T_{\mathrm{Talbot}} = 2\pi \frac{2m}{\hbar k^2} = \frac{2a^2}{h/m} \ . \tag{4.17}$$

Here, we used the relation $k = 2\pi/a$ with a being the lattice constant. Note that one has to use the 1D lattice constant a_{1D} in the 1D case and the 2D case. The reciprocal lattice vectors $\boldsymbol{b_i}$ are defined via the 1D lattice constant $|\boldsymbol{b}_i| = 2\pi/a_{\mathrm{1D}}$ and are responsible for the dynamics after release. For the 2D lattice, we get $T_{\mathrm{Talbot},i} = 2\pi \frac{2m}{\hbar |\boldsymbol{b}_i|^2}$ and by ensuring the same lattice spacing, we have

$$T_{\mathrm{Talbot}} = \frac{2a_{\mathrm{1D}}^2}{h/m} = 13.24\,\mu\mathrm{s} \tag{4.18}$$

for the experimental parameters. As in the optical Talbot effect, there are also secondary revivals at $T_{\mathrm{Talbot}}/2$, which shift the density pattern again by half a period compared to the initial density, which for the triangular lattice means the density of a honeycomb lattice. Higher order revivals for $n/q \cdot T_{\mathrm{Talbot}}$ are also possible, but elusive in our system. The higher orders only appear if the initial wavepackets are strongly confined. Another limiting case is the finite resolution of our matter-wave microscope.

To get an analytical feeling for the matter-wave Talbot effect after release from a lattice, we model the system with Gaussian wavepackets spaced with the 1D lattice constant, following [80]. The initial state is

$$\Psi(x, t=0) = \sum_{n=-\infty}^{\infty} \psi(x - nd) \exp(i\theta_n) \tag{4.19}$$

$$\text{with } \psi_n(x) = \frac{1}{\pi^{1/4}\sqrt{\sigma}} \exp\left(-\frac{(x-nd)^2}{2\sigma}\right) \ , \tag{4.20}$$

where n denotes the n^{th} lattice site with θ_n the phase of the n^{th} wavepacket, d is the spacing between the lattice sites and σ the $1/e$-width of the wavepacket. An exemplary initial state in a lattice is shown in figure 4.4. Upon release from the lattice, the wavefunction evolves freely, which in momentum space is given by

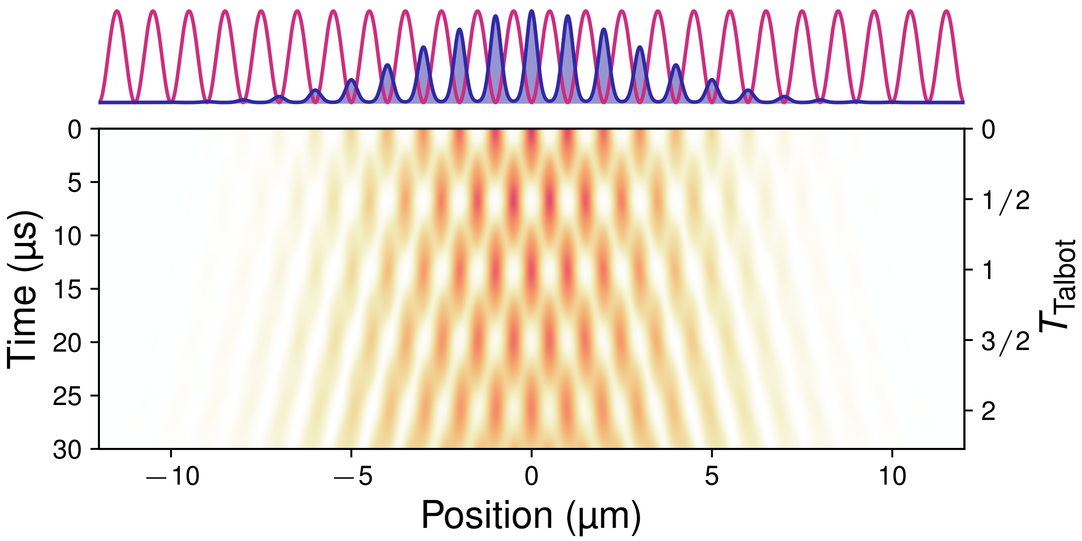

Figure 4.4: Matter-wave Talbot effect. The matter-wave Talbot effect is observed by a propagation in time after the coherent atomic wavefunction (blue filled line) is released from a periodic potential (purple line). We present here a finite system compared to the (almost) infinite one in figure 4.3 as it is closer to the situation in the experiment. The Talbot carpet is obtained by a GPE-simulation as presented in the following chapter. As in the infinite carpet, we observe primary revivals, which now correspond to the Talbot time T_{Talbot} with secondary revivals in between. Here, we do not observe higher order revivals due to the broader initial wavepackets at each lattice site.

$$\Phi(k,t) = \pi^{1/4}\sqrt{2\sigma}\exp\left(-\frac{k^2\sigma^2}{2} - i\frac{\hbar k^2}{2M}t\right)\sum_{n=-\infty}^{\infty}\exp(iknd - i\theta_n) \tag{4.21}$$

$$= \pi^{1/4}\sqrt{2\sigma}\frac{2\pi}{d}\sum_{\tilde{n}=-\infty}^{\infty}\delta(k - \frac{2\pi}{d}\tilde{n})\exp\left(-\frac{2\pi^2\sigma^2}{d^2}\tilde{n}^2 - i\frac{2\pi^2\hbar}{d^2 m}t\tilde{n}^2\right) \tag{4.22}$$

$$= \pi^{1/4}\sqrt{2\sigma}\frac{2\pi}{d}\sum_{\tilde{n}=-\infty}^{\infty}\delta(k - \frac{2\pi}{d}\tilde{n})\exp\left(-\tilde{n}^2\left(\frac{2\pi^2\sigma^2}{d^2} - 2\pi i\frac{t}{T_{\mathrm{Talbot}}}\right)\right) \tag{4.23}$$

where the Fourier representation of the Dirac comb is used and we substituted $T_{\mathrm{Talbot}} = 2d^2/(h/m)$. The last term in the exponential reveals the revival character of the Talbot effect. For $t = lT_{\mathrm{Talbot}}$ the initial wavefunction is restored, $\Phi(k, lT_{\mathrm{Talbot}}) = \Phi(k,0)$. Transforming $\Phi(k,t)$ back to position space and using $\tau = t/T_{\mathrm{Talbot}}$, which sets the time relative to the Talbot revival, we get

$$\Psi(x,\tau) = \frac{\sqrt{\sigma}}{\pi^{1/4}\sqrt{\sigma^2 + id^2\tau/\pi}}\sum_{n=-\infty}^{\infty}\exp\left(-\frac{(x-nd)^2}{2(\sigma^2 + id^2\tau/\pi)} + i\theta_n\right) . \tag{4.24}$$

The calculation of the resulting density, $n(\tau) = \left|\left\langle\Psi^\dagger(x,\tau)\middle|\Psi(x,\tau)\right\rangle\right|^2$, becomes quite involved, and we state the result from [80]. They find, by projecting back onto a single Gaussian wavepacket, that the overlap of the revival wavefunction with the initial wavefunction is a measure for the coherence. The projection is given as $n(\tau) = \left|\left\langle\psi_n^\dagger(x)\middle|\Psi(x,\tau)\right\rangle\right|^2$. The average density becomes

$$\overline{n_0(\tau = N)} \approx \frac{\sqrt{2\pi}\sigma}{d}\sum_{n=-\infty}^{\infty}C_{2Nn}\exp\left(-\frac{2\pi^2\sigma^2}{d^2}n^2\right) , \tag{4.25}$$

where C is defined as the phase correlator via $C_{n-n'} = \langle \exp(i(\theta_n - \theta_{n'})) \rangle$ and N is the number of the primary revival. For typical experimental settings, the above can be approximated taking only $n \leq 1$ into account,

$$\overline{n_0(\tau = N)} \approx \frac{\sqrt{2\pi}\sigma}{d} \left(1 + 2C_{2N} \exp\left(\frac{2\pi^2\sigma^2}{d^2} \right) + ... \right). \tag{4.26}$$

There are two things we can take away from this result: first, the projection back onto the initial density depends on the phase correlators C between lattice sites and gives a measure for the coherence of the system, and second, at the N^{th} primary revival, the projection probes the correlation at a distance of $2N$ lattice spacing. Therefore, if we extract the contrast of the density modulation of the in-situ images, thus comparing it to the maximal possible contrast of the image, we get a measure for the correlation length at $2Na_{\text{lat}}$ when setting $t = NT_{\text{Talbot}}$.

Implementation In the experiment, we measure the matter-wave Talbot effect by varying the time in the harmonic trap after switching off the lattice potential. With this, we image the density just shortly after release from the trap. Varying the time in the first trap measures the Talbot effect of the unmagnified system, and we expect a Talbot time T_{Talbot} of $13.24\,\mu\text{s}$. Note, if we would vary the TOF duration (or similar, the time in a second harmonic trap), the lattice spacing is magnified by M, and the Talbot time by M^2. As the system expands outwards, this eventually leads to too low densities and impractical Talbot times.

With the versatile lattice setup, we are able to create 1D lattices by interfering only two beams while the third beam is kept far detuned. This ensures the same harmonic envelope during the lattice section and the magnification. Matching harmonic confinement during the matter-wave protocol for the 1D and 2D lattices is important, because we use the 1D Talbot revivals to calibrate the isotropy also for the 2D case. In figure 4.5, the magnified density of the 1D Talbot revivals is plotted. The lattice contrast vanishes while increasing the duration in the harmonic trap up to $T_{\text{Talbot}}/4$. Here, one would expect a fractional revival to be present. Due to the shallow trapping and finite size effects, this is not present in our system. From this point on, the contrast increases again, and we find a revival of the lattice structure at $T_{\text{Talbot}}/2$, the secondary revival. This is shifted by half a period from the initial density modulation, but due to the current lattice setup, we do not have a phase lock on the lattice position with respect to the trap center. This leads to variation of the lattice position from shot to shot. We do not see any in-shot movement though. Progressing in time, we observe the lattice contrast vanish again before it revives at the primary Talbot revival.

To extract the Talbot time T_{Talbot}, we Fourier-transform the image and identify the peaks corresponding to the wavevectors of the density modulation. We get a measure for the contrast of the lattice by integrating over a small area containing the peaks' signal, see inset in figure 4.6. These peaks are at the position of the Bragg peaks of the lattice, but differ insofar that they are created by the density of the wavefunction and not the wavefunction itself. Repeating the analysis for a full scan of the harmonic evolution time reveals the full 1D carpet in terms of the contrast. It is notable that we not only see the Talbot effect by looking in positive times but also when looking at shorter times compared to the $T/4$-time of the trap. This is an effect of the symmetry of the magnification process in the harmonic trap. For a perfect harmonic trap, full symmetry around the image of the density is expected as we find in simulations. Here we see a slight asymmetry which we account for the essential Gaussian shape of the trap. We see the intensity of the contrast reducing while increasing the time difference to the image. This is an effect of the finite size of our system. A reduced picture explains this by imagining multiple copies of the cloud moving apart with the respective lattice momenta. As soon as the copies are too far apart to interfere, the contrast is lost. We observe about 8-10 revivals from negative to positive, including secondary ones, which matches the diameter of the cloud of 8-10 lattice sites. Following the cloud's density, we assume the envelope to be Gaussian as well.

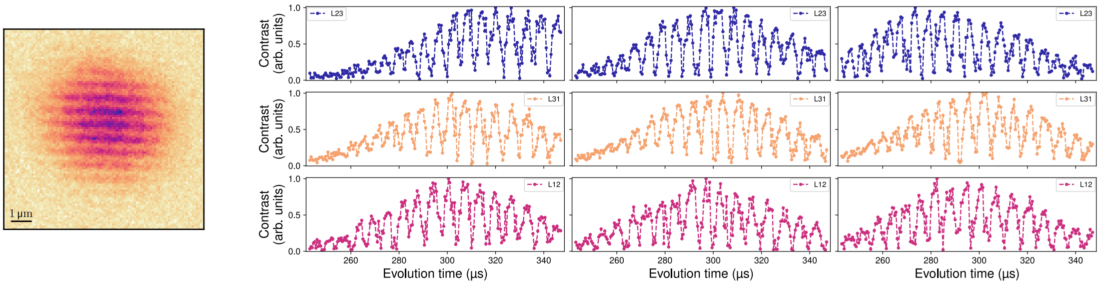

Figure 4.5: Calibration of isotropy. We calibrate the isotropy of the three axes by creating a 1D lattice and magnifying it with all three beams (left). We vary the power of one beam and scan through the Talbot carpet. On the right, we show nine exemplary scans. For each lattice direction, the Talbot carpet is scanned separately. The top row corresponds to the image on the left, and its reciprocal lattice vector is perpendicular to the beam, the power of which is increased from left to right. We observe a substantial shift in the center of the envelope and use this to align the envelope's center of all three axes. The power in L1 is $385\,\mathrm{mW}$, $435\,\mathrm{mW}$ and $485\,\mathrm{mW}$ from left to right.

Calibration of isotropy To measure the 2D Talbot effect, it is essential that all lattice directions are well aligned in their Talbot revivals. This is realized by an optimal isotropy of the magnifying potential. A change in the harmonic trap frequency changes the position of the matter-wave image in time. To overlap all 1D matter-wave images, we change the trap frequency in the direction of the current lattice vector a few percent and measure the shift on the center of the envelope, see figure 4.5. We find that this mainly changes the selected axis and use it to equalize all directional trap frequencies. First, we match the envelopes as good as possible, and then we optimize the overlap of the revivals for positive times. This gives us a very precise way to ensure isotropy of the matter-wave lens.

2D matter-wave Talbot effect As in 1D, we expect the density to undergo self-imaging at the Talbot times T_{Talbot}. In figure 4.6 we again have the magnified in-situ density, and when increasing the harmonic evolution time in the first trap, we see the contrast of the lattice modulation vanish at T_4. Also here, we do not observe the possible fractional revivals. At the secondary revival, we see a fascinating phenomenon of the 2D Talbot effect. In 1D, the single lattice axis would be shifted by half a period; in 2D, this leads to a change of geometry, though. We find a honeycomb-like structure at the secondary revival. We call this the inverted lattice structure. Increasing the harmonic evolution time further, we see the contrast vanish again, and at T_{Talbot}, we have the revived lattice structure.

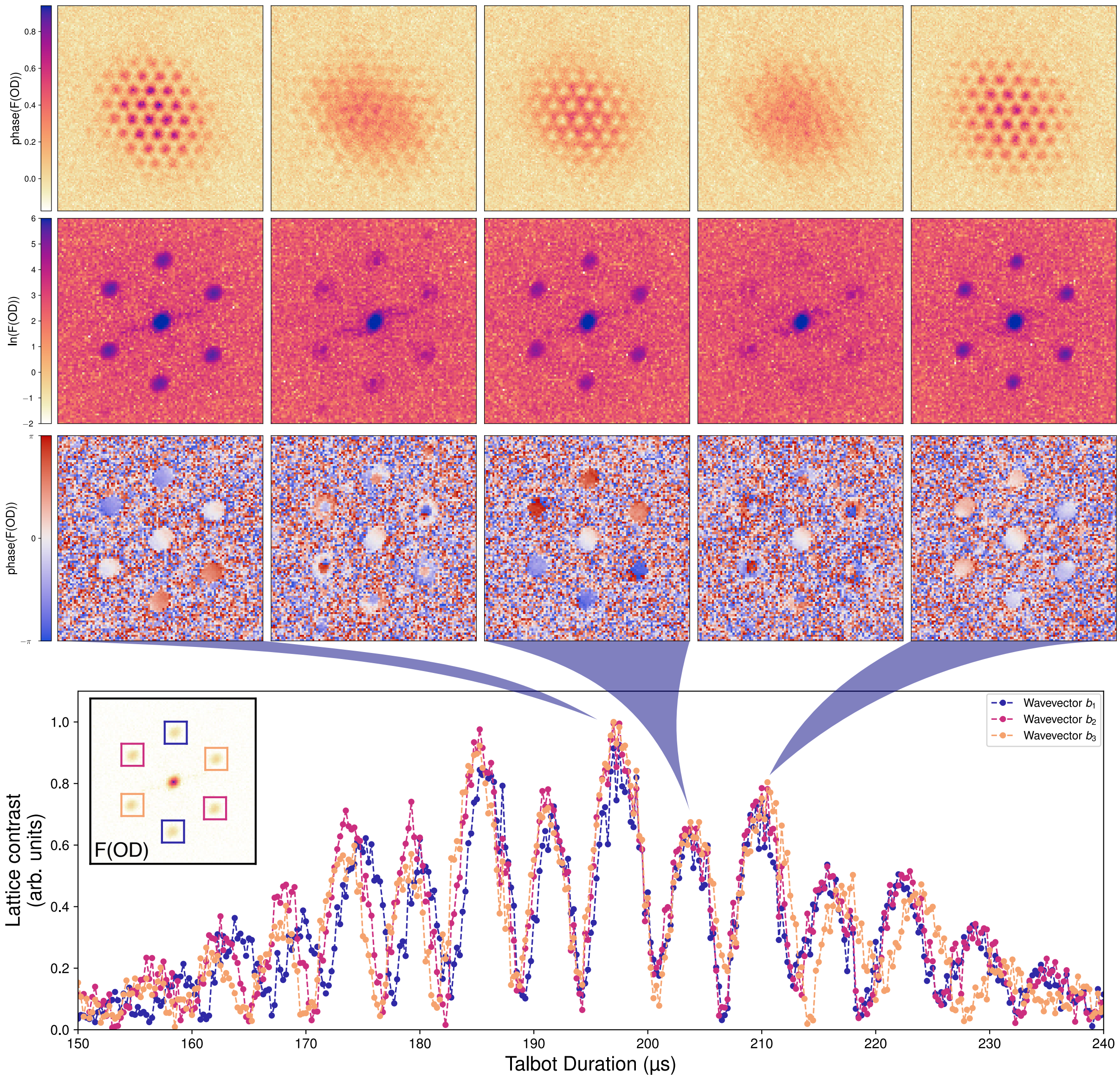

Figure 4.6: 2D Talbot effect. (Top, first row) Example images of ^{7}Li BECs released from a triangular optical lattice with a matter-wave magnification of 35.3(5) and evolution times of $197.5\,\mu\mathrm{s}$, $201.0\,\mu\mathrm{s}$, $204.25\,\mu\mathrm{s}$, $207.0\,\mu\mathrm{s}$ and $210.5\,\mu\mathrm{s}$, showing the Talbot revivals and the loss of lattice contrast for intermediate times. The images show the optical density (OD) in an area of $8.8\,\mu\mathrm{m}$ width in the atomic plane. In the second row, we show the magnitude of the Fourier transformed images of the above with a logarithmic color scale. In the intermediate images, centric structures are visible at the Bragg peaks, which we attribute to the finite size of our system. In the third row, the phase of the Fourier transforms are shown. Here, the phase jump in these centric structures is clearly visible. (Bottom) Lattice contrast as a function of evolution time around the imaging condition at $197.5\,\mu\mathrm{s}$ evaluated along the three directions of the lattice vectors featuring in total 14 Talbot revivals for positive and negative times ($\boldsymbol{b}_1$ in orange, $\boldsymbol{b}_2$ in blue and $\boldsymbol{b}_3$ in purple). The contrast is evaluated as the signal in the boxes around the Bragg peaks in the Fourier transformed images (see inset).

Exemplary magnified in-situ images are shown in figure 4.6 as well as the magnitude and the phase of the Fourier transformation of the images. As in the 1D analysis, we extract from the Fourier analysis the contrast of the lattice modulation by integrating around the momentum peaks of the lattice vectors as visualized in the inset in figure 4.6. We measure the contrast in two different manners. The first is to integrate over the whole area after taking the absolute value of each pixel. This results in a contrast observable greatly known in cold atom lattice experiments, but without the reference to the background. The second one differs in such a way that we first integrate the whole area while keeping the complex numbers resulting from the Fourier transform and then take the absolute value of the integrated result. This has two effects: on the one hand, this eliminates a lot of noise, as this has random phase fluctuations and will integrate to zero; on the other, we have an effect which is particular to our finite size system. As in 1D, we see not a complete depletion of the contrast at $\boldsymbol{b}_{\mathrm{i}}$, but a crossover between two phases of the lattice, see figure 4.4. With this second approach, we are highly sensitive to this position where we would expect the lattice contrast to fully vanish for an infinite system. The effect is nicely visible in the intermediate images, where the Bragg peaks show a ring-like structure in their magnitude as well as in the phase. The phase changes approximately by a factor of π, which fits the expected π-phase shift between primary and secondary revival. With this, we can map out the contrast of the Talbot carpet with high resolution. In figure 4.6, we show the contrast for a full scan of all three axes. Note the precise overlap of all three axes. This was only possible with the above-described fine intensity alignment procedure using the 1D Talbot effect and is of high importance for all further analysis. When reaching higher revivals, we see a dephasing between the three axes. We attribute this to the slight misalignment from the optimal $120°$ setting for the triangular lattice. We observe a slightly smaller Talbot time of $T_{\mathrm{Talbot}} \approx 12\,\mathrm{\mu s}$ than expected. A decrease in the Talbot time can be attributed to an increased effective mass in the lattice. This matches with an observed decrease of the Talbot time with increasing lattice depth.

4.2.2 Optical Talbot effect

As described in the introduction of the Talbot effect, the coherent nature of the absorption light also exhibits the Talbot effect when passing a grating, which is here created by the magnified density modulation of the atoms. Typical lattice quantum gas experiments have lattice constants in the sub-micrometer scale and imaging wavelengths on the same order. The Talbot length in that case would also be on the sub-micrometer scale and difficult to image. In our case, the 1D lattice constant $a_{\mathrm{1D}} = 614\,\mathrm{nm}$ and an imaging wavelength of $\lambda = 671\,\mathrm{nm}$ gives a Talbot length $z_{\mathrm{Talbot}} = 1.12\,\mathrm{\mu m}$. With a typical depth of field around $100\,\mathrm{\mu m}$, this is impossible to resolve. Even with high-NA microscopy as done in quantum gas microscopes [12], the depth of field around one micrometer deems the task of separating primary and secondary revivals extremely difficult and elusive to the authors' knowledge. For a few special cases, the optical Talbot effect on an atom density grating was measured. In [91] they observed the optical Talbot effect from the interference fringes of two BECs. In [92] they had a large lattice spacing of $d = 67.8\,\mathrm{\mu m}$ created by KD scattering from which they observed the optical Talbot effect. By magnifying the lattice structure prior to imaging, we make the optical Talbot effect measurable for atoms released from a lattice with a sub-micrometer lattice constant. The Talbot length for the magnified sample is given by

$$z_{\mathrm{Talbot}} = 2\frac{d^2}{\lambda} = 2\frac{M_{\mathrm{mw}}^2 a_{\mathrm{1D}}^2}{\lambda} = 1.42\,\mathrm{mm}, \tag{4.27}$$

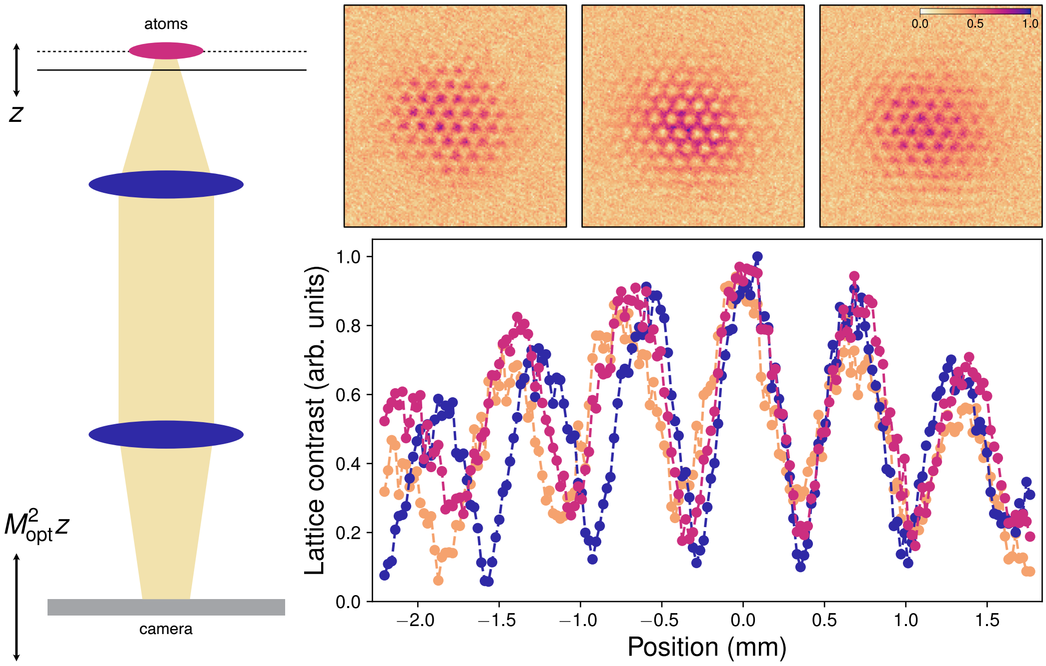

Figure 4.7: Optical Talbot effect. (Left) Sketch of the imaging system. By scanning the camera position, we image different planes around the atom plane. (Upper right) Magnified densities of the BEC in the lattice for the fixed matter-wave imaging condition. The position of the optical imaging plane is varied, yielding primary and secondary optical Talbot revivals. From left to right, at $z = 0$ the image of the magnified lattice is captured, at $z \approx 0.7\,\mathrm{mm}$ the secondary revival, and at $\approx 1.4\,\mathrm{mm}$ the primary revival. The found distances fit well with the expected value of the optical Talbot length $z_{\mathrm{Talbot}} = 1.4\,\mathrm{mm}$. (Bottom right) The lattice contrast as a function of the image plane is shown ($\boldsymbol{b}_1$ in orange, $\boldsymbol{b}_2$ in blue, and $\boldsymbol{b}_3$ in purple). In the measured range, we observe six revivals (primary and secondary). The slight dephasing between the revivals along the different directions is due to a small deviation of the lattice angles.

where we used a matter-wave magnification of $M_{\mathrm{mw}} = 35.5$. A separation of $1.42\,\mathrm{mm}$ is easily resolved by our imaging system, as well as the separation between secondary and primary revivals of $0.72\,\mathrm{mm}$. We measure the optical Talbot effect by moving the camera with a translation stage (sketch fig. 4.7). This moves the imaging plane of the imaging system. A translation Δz in the atom plane is given by a movement of the camera of $M_{\mathrm{opt}}^2 \Delta z$, with the magnification of the optical imaging system $M_{\mathrm{opt}} = 3$. For an optimally aligned imaging system, we get a sharp image of atomic density. Moving the camera about $6.3\,\mathrm{mm}$ allows us to image the secondary revival as well as the primary revival with an additional movement of the same amount. The images are shown in figure 4.7. We move the camera continuously and capture the whole optical Talbot carpet. As in the matter-wave Talbot case, we extract the contrast and find good agreement with the above the Talbot length, see figure 4.7.

We find that the observation of the optical Talbot effect is highly sensitive to the optical alignment of the imaging system. A misalignment leads to dephasing of the three axes and a strong reduction in contrast of the revivals. We find that especially the reduction in contrast is correlated to an asymmetric behavior of lattice-like structures around the central density when imaging far out of focus. We assume this structure to be an intermediate case between near-field and far-field diffraction from the lattice. The asymmetry increases with worse alignment accompanied by a reduced contrast of the corresponding lattice axis. We use this as a tool and optimize the optical alignment in a far out-of-focus condition by creating a symmetric positioning of the lattice-like structures.

4.3 | Coherence carpet

We utilize the matter-wave Talbot effect to study the coherence properties of the 2D lattice system across the Berezinskii-Kosterlitz-Thouless (BKT) phase transition. The array of tubes with weakly interacting BECs can be mapped to a classical XY model [93–95], which exhibits the BKT transition at low temperature. The transition is associated with the unbinding of vortex-anti-vortex pairs to free vortices. The free vortices scramble the phase coherence between the tubes and destroy the superfluidity of the array [32, 96–101]. We are able to measure the phase coherence via the contrast of the Talbot revivals.

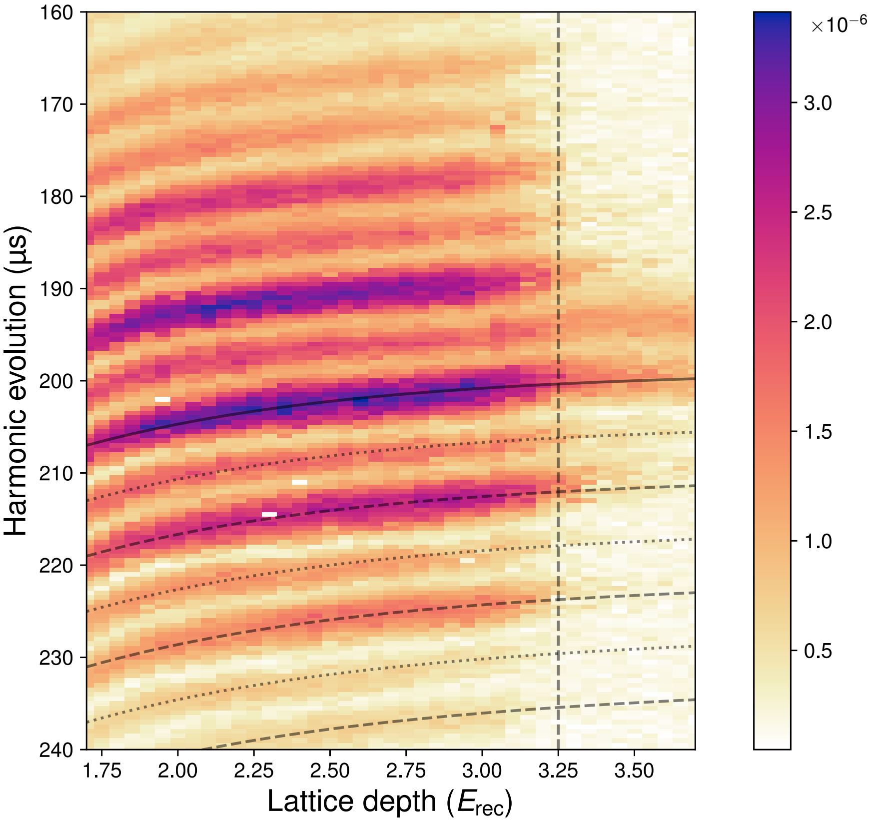

Figure 4.8: Coherence carpet. Contrast around the reciprocal lattice vectors. We measure the lattice contrast for the different lattice depths. The solid line indicates the image branch, the dashed lines the positive primary revivals, and the dotted lines the positive secondary revivals. The branches bend to shorter times due to the finite interaction strength. We assume the phase transition to be at $V_{\mathrm{lat}} = 3.25\,E_{\mathrm{rec}}$, where the contrast in the higher revivals quickly drops.

Increasing lattice depth We probe the BKT transition by increasing the lattice depth and thereby reducing the tunneling between the tubes. For each configuration, we measure a full scan of the

Talbot carpet as in figure 4.6. We average the contrast of all three axes and get a 2D map of the contrast, the coherence carpet (Fig. 4.8). At a lattice depth of $V_{\text{lat}} = 1.7\, E_{\text{rec}}$, we reproduce a similar signal as before with a slight difference in the timing of the imaging condition as different trapping frequencies are used during magnification. The image branch, maximum contrast around the imaging condition, starts at an evolution time of $t \approx 208\,\mu\text{s}$, is shifted to shorter evolution times, and settles at deep lattices around $t \approx 200\,\mu\text{s}$. This shift of about $4\,\%$ in evolution time, we attribute to interaction effects even for the small scattering length of $a_{\text{S}} = 3.6\, a_0$. The interaction effects are more prominent in the shallow lattice because the high density at the Bragg peaks and zero-momentum create a mean-field repulsive potential, while the wavefunction passes through the momentum space associated portion of the matter-wave protocol. Next to the image branch at longer evolution times in the matter-wave-lens potential, we observe the maximum contrast branch of the secondary revival followed by the branch of the first primary revival. The secondary revival has less contrast than the primary revivals, as we already observed. A possible reason for the difference might be, that we use the same analysis for the different geometries, triangular and honeycomb-like. We also find this difference in simple numerical simulations of the free-space two-dimensional Talbot effect. This effect is more pronounced with stronger confinement, i.e. deeper lattices. The higher-order revival branches reduce in contrast as we expect due to finite system size. As before, we also see Talbot revivals towards shorter evolution times. The overall envelope we observe is asymmetric in all axes.

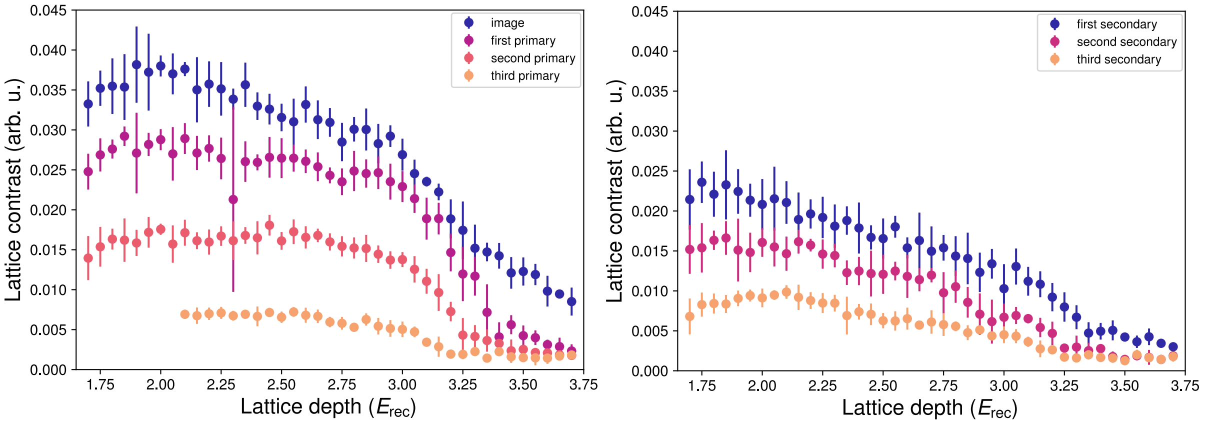

Figure 4.9: Strength of the Talbot revivals. (Left) The lattice contrast along the image branch (solid line in fig. 4.8) and the first and secondary Talbot revival branch (dashed lines in fig. 4.8). (Right) The contrast along the secondary revivals (dotted lines in fig. 4.8). The primary revivals are almost constant up to the phase transition, where all drop to zero. Only the image branch remains finite. The secondary revivals reduce gradually with a steeper decline in the vicinity of the phase transition. (The branch for the third primary revival is not fully captured, thus the missing data points at low lattice depth.)

We fit the contrast for each lattice depth with a heuristic model to extract the time-wise positions of the branches. We additionally fit an exponential function to the former result to get a smooth curve along which we plot the contrast averaged over $\pm 1\,\mu\text{s}$ (Fig. 4.9). Initially, the contrast slightly increases in all shown branches up to $V_{\text{lat}} = 2.0\, E_{\text{rec}}$ and then stays almost constant. Around $V_c = 3.25\, E_{\text{rec}}$ we observe a drop of the contrast in the first and second primary revival and a strong reduction of the image branch, indicating a loss of coherence in the system. We take V_c as the critical value of the BKT-transition in our system. For lattice depth above the transition, we fit an exponential decay with respect to the index of the primary revival (the image branch we take as index zero). The Talbot revivals show the coherence mainly at $d = 2 * n_{\mathrm{revival}}$[80]. We take this into account and get the correlation length in terms of lattice presented in figure 4.10. We observe a divergence towards the critical value, which matches well with the expectation from theory. We fit a Gaussian envelope as we expect it for a finite Gaussian system size. In figure 4.10 we also show the reduced χ^2 for both fits across the phase transition and find that the exponential decay fits better above the phase transition, whereas the Gaussian shape matches much better below the phase transition. With the small system size, i.e. only a few primary revivals for extraction of the correlation length, this analysis has to be treated with caution.

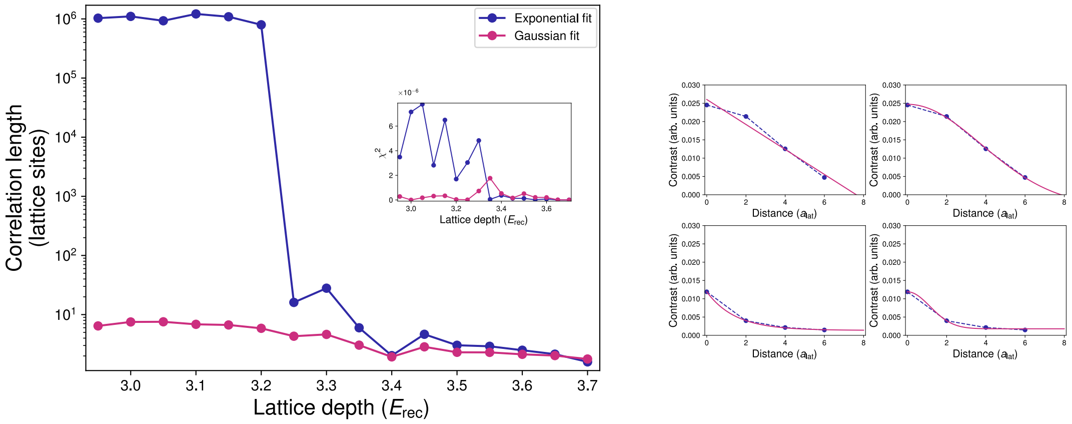

Figure 4.10: Correlation length from Talbot revivals. We fit an exponential decay to the strength of the primary revivals around the phase transition and find a vanishing correlation length. Towards the phase transition, the correlation length diverges, but we note that an exponential decay is not a valid model anymore in this regime. We additionally fit a Gaussian envelope to the same data and find that it holds better below the phase transition. For an infinite system, we would expect the revival strength to be (almost) constant for a fully coherent system. Our finite size of Gaussian shape reduces the revival strength with system size, i.e. with the Gaussian shape, we assume the system to be coherent. The reduced χ^2 above the phase transition, shown in the inset, is mainly smaller for the exponential decay, confirming the change in functional behavior and the loss of coherence. On the right, we show two exemplary lattice depths below and above the phase transition, $V_{\mathrm{lat}} = 3.05$ and $V_{\mathrm{lat}} = 3.55$, (top and bottom, respectively). The left shows the exponential fit, the right the Gaussian fit.

In figure 4.11 we show exemplary images along the image and first primary revival branch, as well as the first secondary branch. Along the image branch we see the system's $1/e^2$-diameter increase from 5 to 9 lattice sites, which is due to the increased effective onsite interaction, which indicates thermal equilibrium. This interaction effect is separate from the interaction effect during expansion. With increasing lattice depth we see fluctuations in the density per lattice site get stronger up to V_c. This effect will be discussed in detail in the following chapter. The lattice structure on the image branch remains triangular throughout all lattice depths. This is in stark contrast to the other exemplary images of the primary and secondary revival around and above V_c. This confirms the correct determination of the image branch. Along the branch of the revivals the triangular lattice structure is lost above the critical lattice depth. Instead we observe a speckle-like structure. This is a phenomenon analogous to laser speckle, where the emitters are coherent light but the phase between

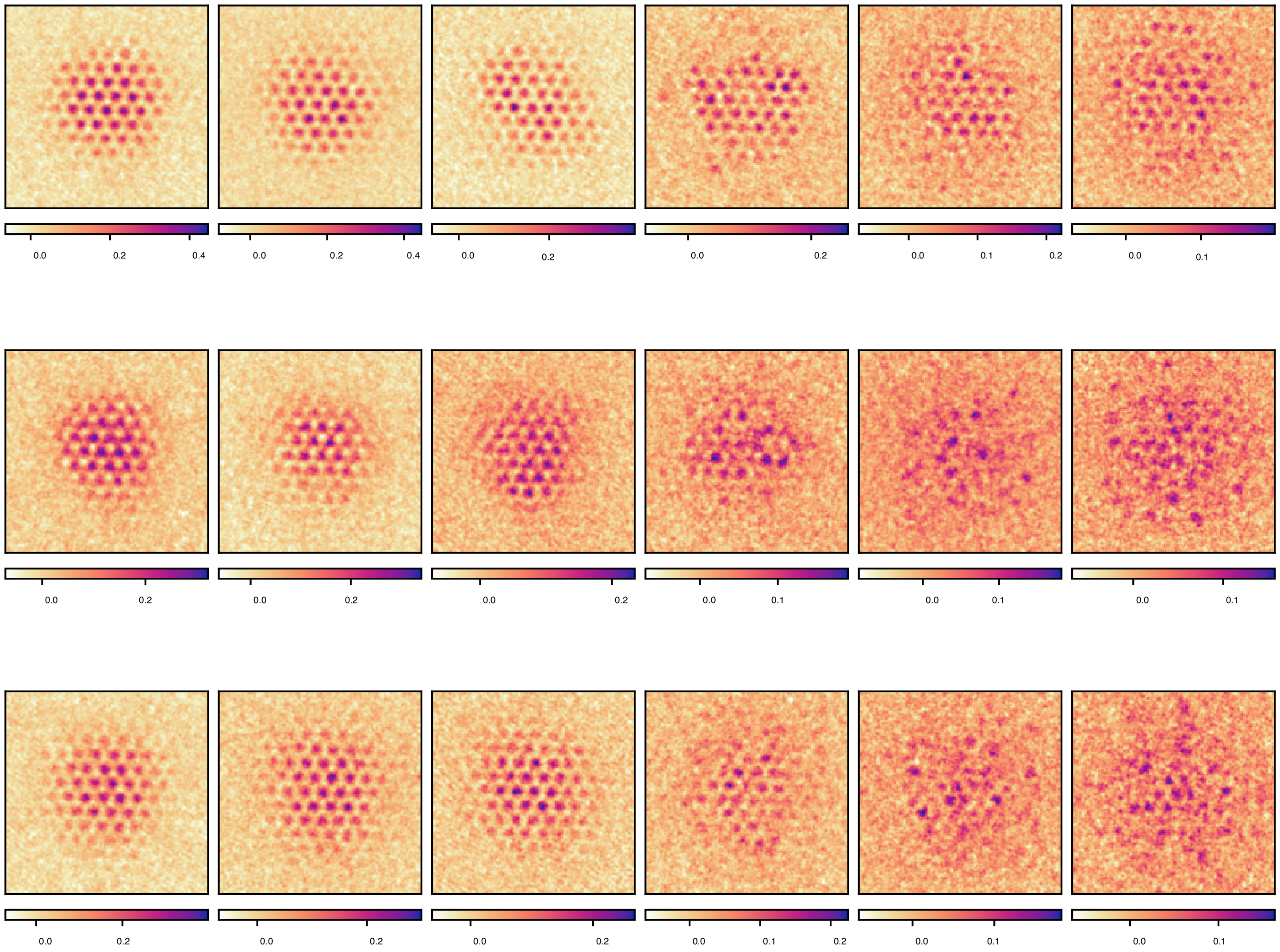

Figure 4.11: Coherence carpet. Images of the magnified density along the image, secondary, and the primary revival branch (top to bottom). The selected lattice depths are $V_{\mathrm{lat}} = 1.9, 2.3, 2.7, 3.2, 3.35$ and $3.5\,E_{\mathrm{rec}}$. A Gaussian filter with $\sigma = 0.7\,\mathrm{px}$ is applied to the images.

them is random. Here, we have separate BECs in each tube which in themselves are still coherent. The phase between them is scrambled above the phase transition resulting in random relative phases. This produces the speckle pattern as seen in the 1D Talbot effect[89].

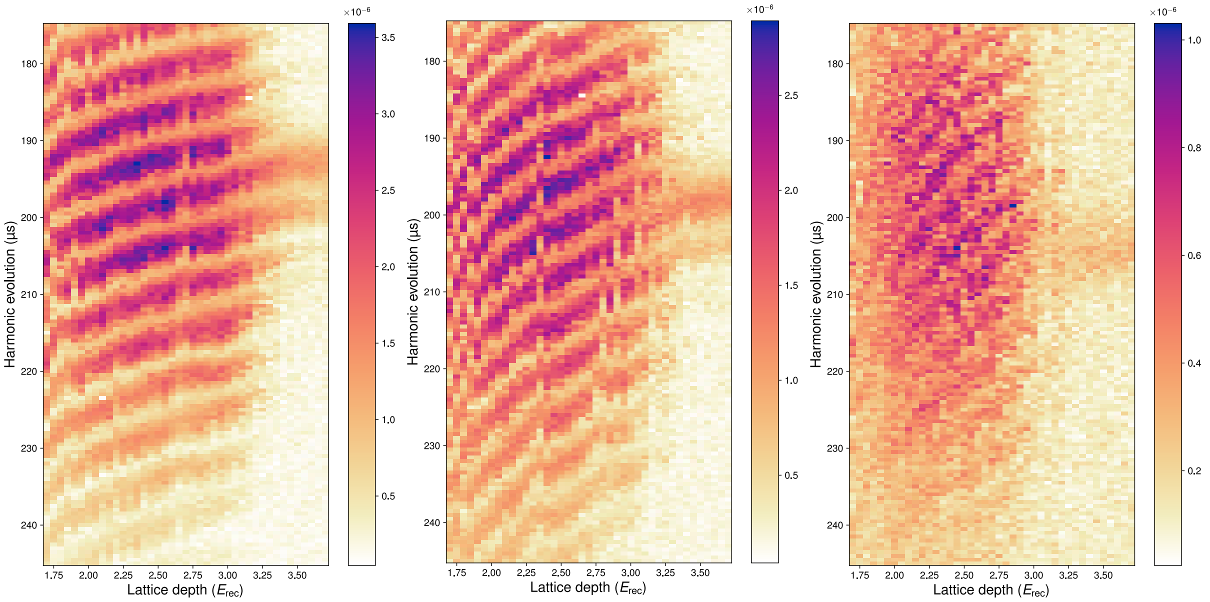

Figure 4.12: Coherence carpet with interactions. Same as in figure 4.8 but with increased interactions. The scattering lengths are $8.3\,\mathrm{a}_0$, $31.5\,\mathrm{a}_0$ and $76.1\,\mathrm{a}_0$ compared to $3.6\,\mathrm{a}_0$. For stronger interactions, the branches bend more strongly to later times with less lattice depth, which is according to expectations. For the strongest interaction measured here, we see the contrast vanish for all times and low lattice depths as no sharp image of the lattice structure can be acquired. For intermediate lattice depth, the Talbot branches reappear weakly, before the contrast vanishes for all branches except the image branch. This takes place at a lower lattice depth than in the almost non-interacting case, $V_{c,76\,a_0} \approx 3\,E_{\mathrm{rec}}$ compared to $V_c = 3.25\,E_{\mathrm{rec}}$.

Different interactions The above measurements were taken at $a_s = 3.6\,a_0$, which results in almost no contact interaction. We took brief measurements of the coherence carpet also for stronger interaction values. As these are earlier measurements, we note that the timing of the imaging condition varies to the above measurement. In addition, we optimized the ramping procedure of the lattice depth between this and the above measurement. The following data thus has to be taken with care in terms of thermal equilibrium. Nonetheless, they provide a great intuition on interaction effects during the matter-wave protocol. The additional measurements are taken at $610\,\mathrm{G}$, $670\,\mathrm{G}$ and $702\,\mathrm{G}$, which correspond to a scattering length of $8.3\,\mathrm{a}_0$, $31.5\,\mathrm{a}_0$ and $76.1\,\mathrm{a}_0$[40]. The coherence carpets are plotted in figure 4.12. With increasing interaction, we see the revivals shift to longer evolution times. The effect increases with decreasing lattice depth. Whereas, we find the image branch at $V_{\mathrm{lat}} = 1.7\,E_{\mathrm{rec}}$ and $610\,\mathrm{G}$ at an evolution time of $T_{4,\mathrm{eff}} = 213\,\mu\mathrm{s}$, the shift at $670\,\mathrm{G}$ is increased by almost $20\,\mu\mathrm{s}$ ($10\,\%$ of the quarter period) to $T_{4,\mathrm{eff}} = 230\,\mu\mathrm{s}$. At $702\,\mathrm{G}$, it is quite difficult to follow the image branch to shallow lattices as here the interaction effect during the matter-wave protocol becomes so strong that it completely washes out the lattice structure. We identify the branch with a peak at about $t = 225\,\mu\mathrm{s}$ and $V_{\mathrm{lat}} = 2.25\,E_{\mathrm{rec}}$ as the image and follow it to shallower lattices. At $t = 230\,\mu\mathrm{s}$ and $V_{\mathrm{lat}} = 2.2\,E_{\mathrm{rec}}$ it closes in with a next branch, which is barely visible here. This branch is at $t = 242\,\mu\mathrm{s}$ for the shallowest lattice, i.e. the image branch is outside the measured area and would have an increase in quarter period of more than $20\,\%$ compared to the (almost) non-interacting case. The shift to longer evolution times confirms the mean-field effect introduced by interaction as described in [21]. The wavefunction acts as a concave matter-wave lens on itself, increasing the effective focal time. For the deepest lattices in these measurements, we only see a small shift from the almost non-interacting to the stronger interacting case of about $5\,\%$. This corroborates the notion that in momentum space high densities lead to an effective concave lens.

The Talbot effect does not seem to be affected strongly by the higher interaction strengths. In all measurements multiple revivals are visible although hardly distinguishable from the background for the strongest interaction and higher revivals. In [80, 88] they also find that interactions only have a small effect on the Talbot effect.

The location of the phase transition barely changes for $8.3\,\mathrm{a}_0$ and $31.5\,\mathrm{a}_0$, but at $76\,\mathrm{a}_0$ it shifts down to $V_c \approx 3\,E_{\mathrm{rec}}$. The behavior is still similar though, along all revivals the contrast drops and only the image branch remains. A stronger interaction can lead to a reduction of the BKT temperature, compare [102], but also enhanced multi-particle tunneling rate due to a larger number of atoms could explain the shift. It will be highly interesting to study this in more detail and push it to the strongly correlated regime, eventually.

Conclusion & Outlook

In this chapter, we presented the matter-wave microscope using an optical matter-wave lens. Our ability to image coherent systems allowed us for the first time to image the matter-wave Talbot effect from a 2D grating. The necessary coherence for the Talbot effect enabled us to probe the coherence of the system. In our system of tubes, we were able to measure the loss of coherence at the BKT phase transition. We will discuss the BKT-transition in more detail in the following chapter and extend the measurement capabilities. Besides the exploration of the BKT transition, this new tool opens the possibilities to probe other phase transitions, like the BEC transition, and more complex phenomena in the many-body regime. In the following chapter, we will introduce the phase microscope, but we want to note that already in the first secondary and primary revival, the information of the relative phase should be present. The relation between the phase on single sites and the resulting density is complex, as we have seen in the theoretical description. We thus envision a Gerchberg-Saxton-like (GS) algorithm[103] to extract the phase from a Talbot revival, either the secondary or the primary (possibly also even density distribution in between). We performed first numerical simulations in that direction and were able to restore the phase per lattice site from a revival image (Fig. 4.13). Here, the propagation was straightforward and possible to back-propagate. For an experimental system, this can become quite involved, and machine learning could be employed as a helpful and powerful tool to realize a full-fledged Talbot phase microscope.

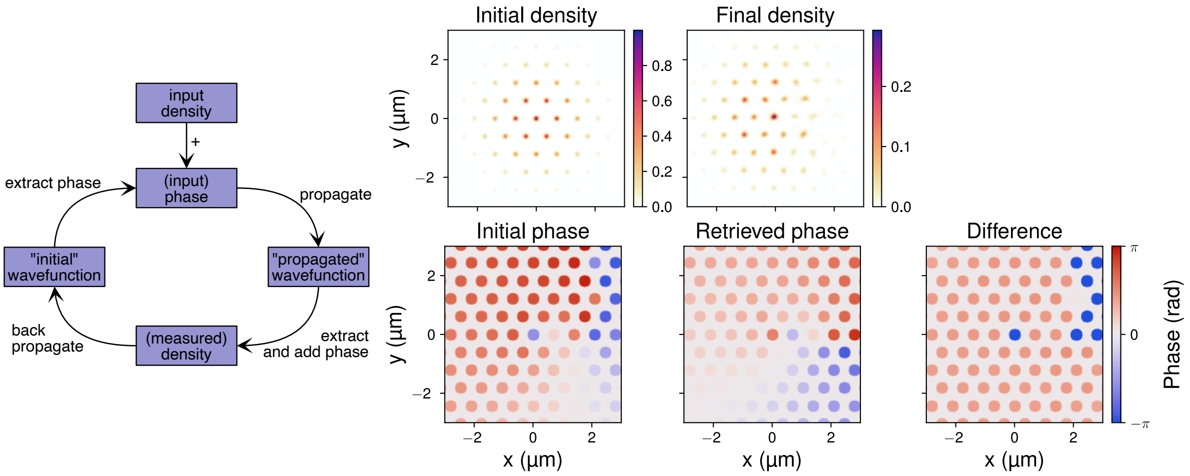

Figure 4.13: Phase retrieval from Talbot revivals. (Left) Sketch of the principle of the GS-like algorithm used to extract the onsite phase. The input phase is added to the input density, and this wavefunction is propagated forward. From the propagated wavefunction, the phase is extracted and added to the final (measured) density. This is propagated back, and again the phase is extracted and added to the input density. From here, the loop is repeated for several iterations until a threshold or hard cap is reached. (Right) A first test of the algorithm with a free space propagation of the experimentally close density distribution. 30 iterations reconstruct it very well with only a global phase offset. The leftmost column shows the initial density (top) and its phase (bottom). The top right shows the propagated density (here the primary revival) used as the measured density from which the phase at the bottom is retrieved. The rightmost image shows the difference between the two to the right.

CHAPTER 5

Phase microscope

The Talbot effect is a great tool to infer global as well as local coherence properties [80], relying on its intrinsic interference between many lattice sites. The interference between multiple lattice sites can be limiting when the initial phase profile on a single site is of interest. In the previous section, we laid out a route to still accomplish this with Gerchberg-Saxton-like algorithms and an envisioned use of machine learning. Here we present a phase microscope inspired by [104], which provides direct access to the local phases. This scheme relies on a momentum-dependent phase imprint, which can be realized during the matter-wave optics. The idea is sketched in figure 5.1 on the left. The phase imprinting in the Fourier plane is analogous to the well-known technique of phase contrast imaging [62, 105, 106]. Phase fluctuations can be mapped in a similar fashion by a short free evolution [98, 101, 107–110]. Here we push the local resolution of the phase-to-density mapping to the single-site level of the used lattice. Instead of imprinting a momentum-dependent phase in the Fourier plane, e.g. with a tightly focused beam addressing only particular momenta, we utilize the aberrations introduced by the first lens of the matter-wave microscope, see figure 5.1 on the right. We confirm this approach by measuring the decrease of phase correlation towards the Berezinskii-Kosterlitz-Thouless (BKT) transition, which we already encountered in the coherence carpet measurement in the previous chapter. With the phase microscope, we are able to extract the critical exponent η_c of the algebraic decay[23].

We first recap the BKT phase transition and its applicability to our system. Secondly, the aberration-induced phase accumulation is discussed. Finally, the experimental implementation and analysis are presented.

5.1 | BKT phase transition

The Berezinskii-Kosterlitz-Thouless (BKT) transition [33, 34] highlights the impact of dimensionality on the properties of a physical system. In a three-dimensional system at temperatures below a critical temperature $T_{\mathrm{c,BEC}}$, a Bose gas condenses and exhibits true long-range order (LRO). In a two-dimensional system, however, no true long-range order is possible at any finite temperature. Thermal fluctuations prevent long-range order from building up, and the formation of BEC is formally prohibited. Instead, a transition of the functional form in the first-order correlation $g_1(r) = \langle \psi^\dagger(\boldsymbol{r})\psi(0) \rangle$ from exponential to algebraic is found in interacting systems. The algebraic decay of the correlation

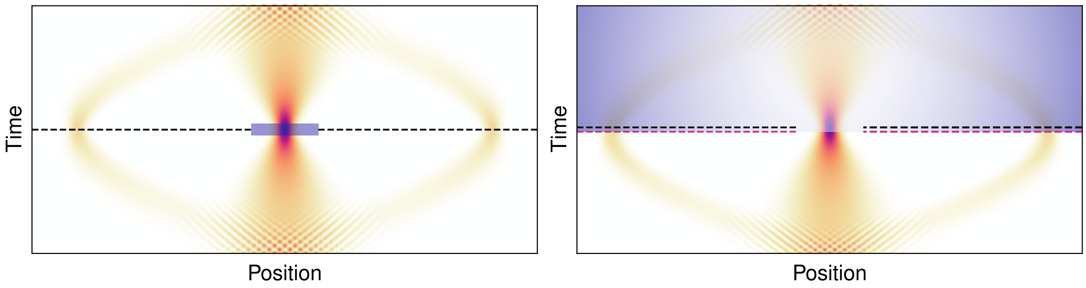

Figure 5.1: Sketch of the phase microscope. (Left) Phase microscope realization with imprinting a constant phase on the zero momentum. The wavefunction is propagated in a harmonic trap to momentum space, indicated by the dashed line, where the phase is imprinted and then propagated back to position space to measure the density deviation, i.e. the phase. (Right) Realization with a continuous phase accumulation in an anharmonic trap. The wavefunction accumulates phase while propagating in the anharmonic trap up to the focusing condition, effective momentum space, indicated by the red dashed line. From there, the propagation is performed in a harmonic trap (or by free expansion).

function is very slow, and quasi-LRO is observed below a critical temperature $T_{\mathrm{c,BKT}}$. In this section, we give a short introduction to the topic and, in particular, discuss the mapping from an array of tubes with coupled BECs to the XY-model. We will follow loosely the comprehensive review by Hadzibabic and Dalibard[111].

No true LRO in 2D The notion that systems with a dimensionality $d < 3$ will not exhibit LRO was first investigated by Peierls[112, 113] and later studied by Bogoliubov[114], Hohenberg[115], and Mermin and Wagner[116]. Their finding states that there is no LRO order at any finite temperature for 1D or 2D systems, which is the known Mermin-Wagner theorem. In 3D, the low-temperature phase transitions are accompanied by the spontaneous breaking of a continuous symmetry in the Hamiltonian. In low dimensions, the spontaneous symmetry breaking is prevented by low-energy, low-wavelength thermal fluctuations, always restoring the symmetry. For the infinite homogeneous Bose gas, this prevents condensation into the ground state. In 3D, the critical temperature for condensation can be found via the density of states and the saturation of the excited states, forcing all particles into the ground state. The density of states in 3D is energy-dependent via

$$\mathrm{DoS}(\epsilon) = V\frac{\sqrt{2}}{2\pi^2\hbar^2}(m)^3/2\sqrt{\epsilon}, \tag{5.1}$$

where V is the considered volume and m is the mass of the particles. The energy ϵ is given as the kinetic energy $\epsilon = p^2/2m$. For the density of states, the following dependence on the dimension can be found

$$\mathrm{DoS}(\epsilon) \propto \epsilon^{\alpha-1}, \tag{5.2}$$

where α describes the dependence on the dimension with respect to a considered volume element. For the homogeneous case, α is given by $\alpha = d/2$, for the often experimentally relevant case of a harmonic confinement, it is $\alpha = d$. The number density for the Bose gas with the respective Bose-Einstein statistic $1/(\exp(-\beta(\epsilon - \mu) - 1)$ is solved with the polylogarithm $Li_\alpha(z)$:

$$n_d(\epsilon) \propto Li_\alpha(z) \tag{5.3}$$

For a homogeneous 3D Bose gas with $\alpha = 3/2$, the polylogarithm is finite on the interval of the fugacity $z \in [0,1]$, i.e. the number of possible excited states is capped and goes to zero for $T \to 0$. This results in a macroscopically populated ground state, and a BEC is formed. In the two-dimensional homogeneous case, we have $\alpha = 1$, and the polylogarithm diverges at $z = 1$, and the population of the excited states is always possible apart from $T = 0$, no condensation takes place. As we will see for a harmonic confinement with $\alpha = d$, the 2D number density will be $n_{2,\mathrm{HO}} \propto Li_2(x)$, which is finite for $z \in [0,1]$ and condensation will be possible.

Correlation at low-energy - ideal Bose gas From the number density of the 2D uniform Bose gas, we can deduce the first-order correlation function as

$$g_1(\boldsymbol{r}) = \frac{1}{(2\pi)^2}\int_0^\infty \mathrm{d}^2k\, n_{\boldsymbol{k}} e^{i\boldsymbol{k}\cdot\boldsymbol{r}}, \tag{5.4}$$

where $n_{\boldsymbol{k}} = 1/(\exp(\beta(\epsilon_k - \mu) - 1)$ and $\epsilon_k = \hbar^2 k^2/2m$. Without condensation, the correlation always vanishes for $r \to \infty$, but the decay shows different behavior at low and high temperatures. For high temperatures, the number density is given by

$$n_{\boldsymbol{k}} \approx z e^{-\beta\epsilon_k} \approx n\lambda_{\mathrm{dB}}^2 e^{-k^2\lambda^2/4\pi} \ll 1(\forall \boldsymbol{k}) \tag{5.5}$$

and all momentum states are weakly occupied. This gives a Gaussian decay of the correlation

$$g_1(r) \approx n e^{-\pi r^2/\lambda^2} \tag{5.6}$$

with a length scale of $\lambda/\sqrt{\pi}$. Thus, the high-temperature Bose gas shows only short-range correlations.

At low temperatures, in the degenerate regime, where $n\lambda^2 > 1$, we have to differentiate between low and high-energy states. While the high-energy states are still only weakly populated, the low-energy states are highly populated. The number density for the high-energy states remains Gaussian. With $\beta\epsilon_k \ll 1$ for $k^2 \ll 4\pi/\lambda^2$, the number density becomes

$$n_{\boldsymbol{k}} \approx \frac{k_\mathrm{B}}{\epsilon_k = |\mu|} = \frac{4\pi}{\lambda^2}\frac{1}{k^2 + k_c^2} \gg 1, \tag{5.7}$$

with $k_c = \sqrt{2m|\mu|}/\hbar$. This gives a bimodal form of the correlation function. At short distances, $r \approx \lambda$ (Fourier transform of the high momenta), g_1 remains Gaussian, but at large distances with $r \gg \lambda$ the decay becomes exponential:

$$g_1(r) \approx e^{-r/l} \text{ with } l = k_c^{-1} \approx \lambda e^{n\lambda^2/2}/\sqrt{4\pi} \tag{5.8}$$

Although there is no phase transition, there is a change from a Gaussian decay to an exponential decay, the correlation length of which $l \propto e^n\lambda^2$ grows exponentially with decreasing temperature. This can lead to correlations spanning over the whole system in a finite-size experiment.

Interactions With repulsive interactions, the low-temperature behavior changes, and a phase transition from normal fluid to superfluid is found, the BKT phase transition. For the homogeneous case, the prior statement of no condensation into a BEC holds, though. For the low-temperature atomic gas we consider here, we have only contact interactions. The interaction strength in 3D is $g_{\mathrm{3D}} = (4\pi\hbar^2/m)a_s$, where a_s is the 3D scattering length. The 3D interaction is proportional to the scattering length; in 2D, the relation can be defined as

$$g = \frac{\hbar^2}{m}\tilde{g}, \tag{5.9}$$

where $\tilde{g}$ is dimensionless. The healing length becomes $\xi = \hbar/\sqrt{mgn} = 1/\sqrt{\tilde{g}n}$. The strongly interacting regime is reached for $E_{\mathrm{int}} = E_{\mathrm{kin}}$, which in the case of the 2D gas is given at $\tilde{g} = 2\pi$.

For a weakly repulsively interacting gas, the thermal fluctuations at low temperatures are strongly suppressed. The energy cost for adding a particle is

$$\frac{\partial E_{\mathrm{int}}}{\partial N} = gn = \frac{\hbar^2}{m}\tilde{g} \tag{5.10}$$

and comparing it to $k_{\mathrm{B}}T$ confirms the suppression for low temperatures where $D \gg 2\pi/\tilde{g}$. When assuming a macroscopic wavefunction $\Psi = \sqrt{n}e^{i\theta}$ and suppression of thermal density fluctuations, an effective low-energy Hamiltonian can be found including only phase fluctuations:

$$H_\theta = \frac{\hbar^2}{2m}n_s \int (\nabla\theta)^2 d^2r, \tag{5.11}$$

where $n_s \leq n$ is the superfluid density. This is the continuous version of the Hamiltonian of the XY model with spins on a lattice. A formal mapping though is only given if density fluctuations are fully suppressed. Hadzibabic and Dalibard follow with a Bogoliubov analysis showing why the density fluctuations are sufficiently suppressed and that the phase fluctuations destroy true LRO. The argument here is that the energy cost for phase fluctuations $k \to 0$ goes to zero and due to the population of the low k energy states in 2D becomes relevant. With the Bogoliubov analysis, they also arrive at the low-energy Hamiltonian. Finally, they derive the algebraic decay of the correlations for $r \gg \xi$ and $k \ll 1/\xi$. Starting again with $\psi = \sqrt{n_s}e^{i\theta}$, the one-body correlation function is

$$\begin{aligned} g_1(r) &= \left\langle \psi^\dagger(\boldsymbol{r})\psi(0) \right\rangle = n_s \left\langle e^{i(\theta(\boldsymbol{r})-\theta(0))} \right\rangle & (5.12) \\ &= n_s e^{-\frac{1}{2}\left(\left\langle \Delta\theta(\boldsymbol{r})^2 \right\rangle\right)}, & (5.13) \end{aligned}$$

where $\Delta\theta = \theta(\boldsymbol{r}) - \theta(0)$ is introduced, which is assumed to be an independent Gaussian variable u such that $\left\langle e^{iu} \right\rangle = e^{-1/2\left\langle u^2 \right\rangle}$. With the analysis of the low-energy momentum modes, they arrive at the following algebraic decay:

$$g_1(r) = n_s \left(\frac{\xi}{r}\right)^{1/\left(n_s\lambda^2\right)}, \tag{5.14}$$

where $n_s\lambda^2$ is the superfluid phase space density.

BKT mechanism - vortex-anti-vortex unbinding The microscopic theory by Berezinskii and Kosterlitz and Thouless takes into account another natural occurrence of phase fluctuation besides phonons: vortices. The vortices play a crucial role in describing the phase transition. While the phonon excitation can explain the destruction of true LRO, they cannot explain the sudden transition. With the addition of vortices, this is explained by the unbinding of vortex-anti-vortex pairs. A vortex-anti-vortex pair consists of two (single-charged) vortices with opposite rotation, i.e. opposite sign in their phase winding, $\pm 2\pi$, for a single-charged vortex. A bound pair of vortices, a "dipole", causes only a distortion of the phase in the close vicinity of the pair. At larger distances around the pair, no significant change of the phase is present. The dipoles affect the correlation function $g_1(r)$ only at short distances but do not change the behavior at long distances. The pairs are (tightly) bound below the BKT transition temperature T_{BKT}. Above the critical temperature, the pairs unbind, and eventually, free vortices are present. Their disorder and long-range phase field completely "scrambles" the phase and thereby destroys quasi LRO in the system and reduces the superfluid density. The BKT phase transition can be considered a topological one. At temperatures below T_{BKT}, the whole system has a common phase; the phonons add only smooth variation, as do the dipole vortices. On a closed contour, the defect can be annihilated, which makes this state topological comparable with that of a BEC. For free vortices, this argument does not hold anymore; i.e. the distortion cannot be eliminated by continuous deformations. We will follow the simple physical picture presented by Hadzibabic and Dalibard to explain how the vortices drive the phase transition. A full thermodynamical description was formally derived in [117]. The main finding here is that the superfluid density exhibits a universal jump from $n_s = 0$ in the normal fluid to $n_s = 4/\lambda_{\mathrm{dB}}^2$ below the critical temperature. This signature was experimentally first shown in thin superfluid helium films[118]. The argument is based on the free energy $F = E - TS$ associated with single vortices. The kinetic energy of a vortex is given by

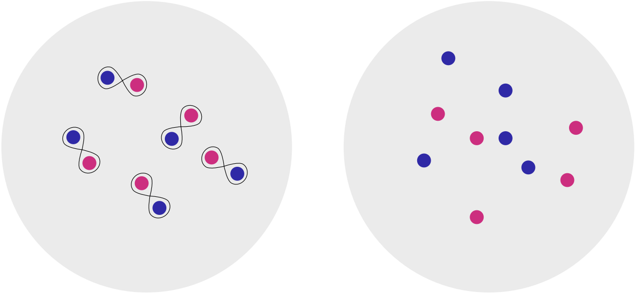

Figure 5.2: Sketch of the vortex-anti-vortex unbinding. For temperature below the phase transition, $T < T_{\mathrm{BKT}}$, vortex excitation only appears in pairs of counter-rotating vortices (left). As the temperature is increased, the distance between the two vortices becomes larger and eventually decouples, i.e. free vortices are created. The free vortices scramble the phase and destroy the quasi LRO of the system.

$$E = \int_{\xi}^{R} \frac{1}{2} n_s \left(\frac{\hbar}{mr}\right)^2 d^2 r = \frac{\hbar^2 \pi}{m} n_s \ln\left(\frac{R}{\xi}\right), \tag{5.15}$$

where the integration goes from the vortex radius ξ to the edge of circular geometry at radius $R \gg \xi$ with $R \to \infty$. All possibilities of placing the vortex inside this geometry give the entropy associated with the vortex as

$$S = k_{\mathrm{B}} \ln\left(\frac{R^2\pi}{\xi^2\pi}\right) = 2k_{\mathrm{B}} \ln\left(\frac{R}{\xi}\right). \tag{5.16}$$

With this, the free energy becomes

$$\begin{aligned} F &= \left(\frac{\hbar^2\pi}{m} n_s - 2k_{\mathrm{B}}T\right) \ln\left(\frac{R}{\xi}\right) && (5.17) \\ &= \frac{k_{\mathrm{B}}T}{2}\left(n_s\lambda_{\mathrm{dB}}^2 - 4\right) \ln\left(\frac{R}{\xi}\right). && (5.18) \end{aligned}$$

The change of sign of the free energy at $n_s\lambda_{\mathrm{dB}}^2 = 4$ defines the transition temperature T_{BKT}. Below T_{BKT}, the large positive free energy ensures the stability of the superfluid, i.e. no free vortices can be formed. Going across the transition from below, the now negative free energy does not prevent the creation of free vortices and thus lowers the superfluid density, which enhances the creation of vortices. This becomes an avalanche process, and the superfluid is completely destroyed. The superfluid density can only take values above $4/\lambda_{\mathrm{dB}}^2$ or zero, but not in between. The curve jumps from zero to this value at the phase transition, but then further increases for even lower temperatures.

Experiments in trapped 2D gases Besides the observation of the BKT transition in liquid helium, experiments with ultra-cold quantum gases made efforts to observe the transition in systems confined to 2D. The first signature of the BKT transition in atomic gases was found in [32]. Here, they prepared two separate 2D gases and had them interfering at the end of the experiment during a free expansion. The interference showed a clean, unwavy modulation below a critical temperature, whereas above the critical temperature, the interference pattern became wavy. Recent experiments [100, 101] build up on this and find a critical exponent of $\eta = 0.17$ in their finite-size system. In [101], they employ a mapping form the phase fluctuations onto density fluctuations developed in [109], see also [119, 120]. In [99, 121, 122] they let the system freely expand and probe the form of the density distribution. In [99], they find a significantly larger exponent of up to $\eta = 1.4$. The larger values can be explained by the averaging nature of the measurement as pointed out by [123]. Measuring the vortices in the system [94, 124] or stirring it[97, 125] probes the phase transition.

XY model As mentioned, the low energy Hamiltonian, found above, is the continuous version of the XY model. The XY model describes classical spins $\boldsymbol{s}_i$ on a lattice structure,

$$H = J \sum_{\langle i,j \rangle} \boldsymbol{s}_i \cdot \boldsymbol{s}_j - h \sum_i \boldsymbol{s}_i, \tag{5.19}$$

where J is the interaction coupling between spins and h an external (magnetic) field. The indices denote single lattice sites. As the continuous version, the discrete version in 2D exhibits a BKT phase transition. Here the transition is seen in the magnetization m of the system going from a finite value to zero at the transition temperature. The transition temperature depends on the coupling strength between the spins and is found by Monte Carlo simulations to be at $k_{\mathrm{B}}T/J = 0.898(1)$[126].

Array of tubes to XY model In [93] they map a 2D lattice structure of tubes with BECs, as we have it in our system, to the Hamiltonian of the XY model. For frozen out axial excitation and harmonic oscillator length larger than the system size, the field operator is expanded to

$$\Psi(\boldsymbol{r}, t) = \sum_j \psi_j(t)\phi_j(\boldsymbol{r}), \tag{5.20}$$

where $\phi_j(\boldsymbol{r})$ is the Wannier function on a lattice site, ψ the bosonic creation operator, i.e. $N = \psi_j^\dagger \psi_j$ the bosonic number operator each on the j^{th} site. With the expanded field operator, the Bose-Hubbard Hamiltonian is constructed:

$$H = -K \sum_{\langle i,j \rangle} \left(\psi_i^\dagger \psi_j + \text{h.c.} \right) + \frac{U}{2} \sum_j N_j \left(N_j - 1 \right) \tag{5.21}$$

$\sum_{\langle i,j \rangle}$ denotes the sum over nearest neighbors, the onsite interaction $U = (4\pi\hbar^2 a/m) \int \mathrm{d}^3 d\phi_j^4$ is set by the s-wave scattering length, and the tunneling element $K \approx -\int \mathrm{d}r(\hbar^2/(2m)\nabla\phi_i \cdot \nabla\phi_j + \phi_j V \phi_j)$ is controlled by the lattice potential. From the (single-particle) tunneling element, a multi-particle tunneling is defined with the average onsite particle number N_0 via

$$J = 2KN_0. \tag{5.22}$$

For the case that $N_0 \gg 1$ and $J/N_0^2 \ll U$, the Bose-Hubbard model reduces to

$$H = H_{\text{XY}} - \frac{U}{2} \sum_j \frac{\partial^2}{\partial \theta_j^2} \text{ with } H_{\text{XY}} = -J \sum_{\langle i,j \rangle} \cos(\theta_i - \theta_j). \tag{5.23}$$

θ_j is the phase on the j^{th} lattice site, and H_{XY} the Hamiltonian of the XY model with the spins in equation 5.19 given as $\boldsymbol{s}_j = (\cos(\theta_j), \sin(\theta_j))$. The point of the phase transition T_{BKT} is proportional to the multi-particle tunneling element $T_{\text{BKT}} \propto J/k_{\text{B}}$. To study the BKT transition in this system, the critical temperature T_{BEC} for condensation in a single well should be $T_{\text{BEC}} \gg T_{\text{BKT}}$. For low temperatures $T < T_{\text{BEC}}$, a macroscopic wavefunction ψ_j per site can be assumed. With the number fluctuations per site strongly suppressed, the wavefunction is $\psi_j \approx \sqrt{N_0} e^{i\theta_j}$, where N_0 is the average site population and assumed to be constant. From H_{XY}, the magnetization of the system is, expanding the cosine and keeping only the quadratic term,

$$M(N, T) = \left\langle \left| \frac{1}{N} \sum_{i=1}^{N} \boldsymbol{s}_i \right| \right\rangle = \left(\frac{1}{2N} \right)^{T/8\pi}, \tag{5.24}$$

where $\langle \cdot \rangle$ describes a thermal average and N is the number of spins[127]. The Monte Carlo simulation in [127] and [93] show a deviation from the spin-wave result at $k_{\text{B}}T/J \approx 1$ for the 2D XY model. This is due to the unbinding of the vortex-anti-vortex pairs, which leads to the randomization of the phase and a zero magnetization.

The model also describes an array of Josephson junctions in superconducting networks and the mapping is well known[128, 129]. A first experimental implementation of BECs in an array of tubes looking at the BKT transition was performed in [94]. There they used a triangular lattice with ^{87}Rb-atoms and probed the proliferation of free vortices at the transition. The vortices were detected in time-of-flight and they observed the onset of free vortices around $J/(k_{\text{B}}T) = 1$. The phase transition is also observed in an antidot lattice[95].

Experimental parameters We estimate the relevant parameters for our experimental setting and set them in relation with the above bounds. The critical temperature T_{BEC} for condensation in a single well is given by $T_{\mathrm{BEC}} \approx 0.94 N_0^{1/3} \hbar\bar{\omega}/k_{\mathrm{B}}$ [62], where N_0 is the atom number per tube. The onsite trapping frequency is given by $\hbar\omega_t = 3\sqrt{2V_0 E_{\mathrm{rec}}}$. We have a vertical confinement with a trap frequency of $\omega_z = 2\pi \times 941(31)\,\mathrm{Hz}$. For the lattice depth used in the experiments $V_0 = 1.7\ \mathrm{E_{rec}}$ to $3.7\ \mathrm{E_{rec}}$, we get onsite trap frequencies between $\hbar\omega_t = 2\pi \times 140\,\mathrm{kHz}$ and $200\,\mathrm{kHz}$. We take the geometric mean as $\hat{\omega} = (2\omega_t\omega_z)^{1/3}$. With average atom numbers between $N_0 \simeq 600$ and 100, the critical temperature is in the range of $T_{\mathrm{BEC}} \approx 10\,\mu\mathrm{K}$ to $7\,\mu\mathrm{K}$. With the temperatures measured in chapter 2 and reasonable adiabatic loading of the lattice, we have $T < T_{\mathrm{BEC}}$, i.e. the atoms in the wells can be considered as coherent, single BECs with a macroscopic wavefunction and constant phase. The observed speckle patterns in figure 4.11 for deeper lattices support this phase coherence within the tubes.

The relation $J = 2KN_0$ for the Josephson coupling energy is valid for $J/N_0^2 \ll U \ll J$. We estimate the interaction with $U = \frac{4\pi\hbar^2}{m} a_s (\frac{1}{2\pi})^{(3/2)} \frac{1}{a_t^2 a_z}$, where a_t and a_z are the transverse and vertical harmonic oscillator lengths. We find $U \approx h \times 20\,\mathrm{Hz}$. With the single-particle tunneling element found in chapter 3, the above relations are fulfilled. Furthermore, the interaction is sufficiently small that a shift of the transition temperature is not expected [102]. The energy of the axial confinement $\hbar\omega_z = h \times 941(31)\,\mathrm{Hz} = k_{\mathrm{B}} \times 45\,\mathrm{nK}$ is larger than the temperatures of 38 to $13\,\mathrm{nK}$ (see Fig. 5.10). In our range of lattice depths between 1.7 and $3.7\,E_{\mathrm{rec}}$, the band gap between the first two bands is between $4,600$ and $43,000$ times larger than the single particle tunneling energy, and thermal excitations into the second band can be completely neglected.

5.2 | Aberrations by the matter-wave lens

The matter-wave microscope works aberration-free only in the case of two successive harmonic potentials.[3] The potential given by the three overlapped beams is only approximately harmonic, but rather an isotropic Gaussian potential for the relevant area around the intercepting point (Fig. 5.3). The influence of the quartic part leads to a deviation from the trajectories in the harmonic potential, i.e. it creates momentum-dependent phase differences at an effective quarter period. The negative quartic term in the Gaussian potential will lead to an increased quarter period and will, for comparison with optics, introduce anti-spherical aberrations.

A perturbative approach for the evolution in anharmonic traps can be found in [130]. We follow this approach to discuss the effective trap frequency and the resulting phase shift.

We will consider here the 1D case and the Hamiltonian of a perturbed harmonic oscillator of the following form

$$H = \frac{p^2}{2m} + \frac{1}{2} m\omega_0^2 x^2 + m f(x) \ , \tag{5.25}$$

---

[3] The use of a free expansion instead of the second propagation in a harmonic potential creates only very minor aberrations in the momentum distribution. The free expansion as the second matter-wave lens, as used in the experiment, is therefore of no concern.

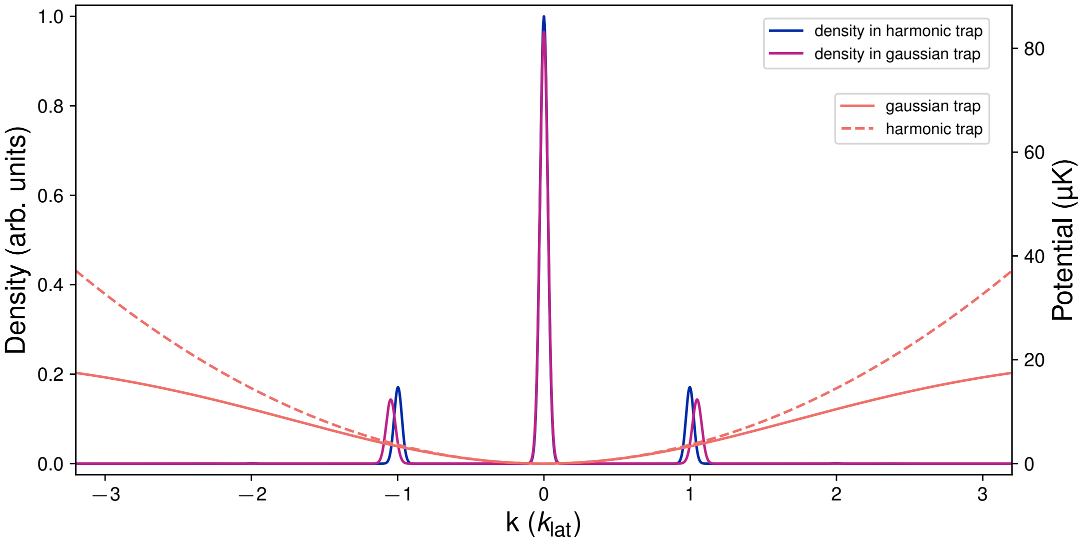

Figure 5.3: Momentum space density distribution in an (an-)harmonic potential. The density distribution after a quarter period in a harmonic trap (dashed orange line, density in blue) and Gaussian trap (solid orange line, density in red) are plotted. The first Bragg peaks of the lattice have higher effective momenta in the Gaussian potential than in the harmonic potential. We also observe a slight decrease in peak intensity, which is linked to slight broadening of the peaks. The Gaussian potential has the same trap frequency in the center as the harmonic potential, $\tilde{\omega}_0 = 1.2\,\mathrm{kHz}$.

with $f(x) = \sum_{n\geq 3} \frac{1}{n}\lambda_n x^n$. In the case of the Gaussian potential, we only have symmetric contributions, i.e. only even n. The potential of the trap has the form $V(x) \propto (1 - \exp(-2x^2/w_0^2))$. We will investigate the system only upto quartic perturbation. We expand the potential around zero and get

$$V(x) = (1/2)m\omega_0^2 x^2 + m(\lambda_4/4)x^4 \ , \tag{5.26}$$

where we kept terms upto fourth-order and obtained the parameter $\lambda_4 = -2(\omega_0/w_0)^2$. Here ω_0 is the trap frequency of the harmonic potential, w_0 is the $1/e^2$-radius of the Gaussian beam and m the mass of the atom.

The perturbative approach is based on the classical equation of motion

$$\ddot{x} - \omega^2 x = -\frac{\mathrm{d}f}{\mathrm{d}x} \tag{5.27}$$

The trajectory of a classical wavepacket in this potential is given as

$$x_\beta = x_{0,\beta} + x_{1,\beta} \tag{5.28}$$

$$= A_\beta \sin(w_\beta t) + \frac{\lambda_4 A_\beta}{32\omega_0^2}\sin(3\omega_\beta t) \tag{5.29}$$

$$= A_\beta \sin(w_\beta t) + \frac{A_\beta}{16}\alpha_\beta^2 \sin(3\omega_\beta t) \ , \tag{5.30}$$

where we introduced $\alpha_\beta = \frac{A_\beta}{\omega_0}$ with the momentum as $p_\beta = \beta\hbar b$. b is the lattice momentum as in chapter 3. The effective frequency is $\omega_\beta = \omega_0 + \omega_1$ and ω_1 is given by

$$\omega_1 = \frac{\lambda_4}{\omega_0} A_\beta^2 \frac{4!}{4!!} = -\frac{3}{4}\alpha_\beta^2 \omega_0. \tag{5.31}$$

So we can rewrite ω_β as $\omega_\beta = \omega_0(1+\epsilon)$ with $\epsilon = -3/4 \cdot \alpha_\beta^2$. The amplitude of the main oscillation is A_β, which will be given in terms of the lattice momenta $A_\beta = \beta \frac{\hbar b}{m\omega_0}$ with $\beta b = \beta \cdot 2\pi/a_{\mathrm{1D}}$. Note that all parameters introduced here are dependent on their initial momentum. In the following, we will drop the momentum-dependent indices for readability.

To describe the effect of the aberration of the matter-wave lens, we are interested in the phase evolution of the system. Here, we look at the phase deviation after a quarter period in the trap. The accumulated phase during the process can be described by the classical trajectory of a wavepacket and calculating its action over the time interval $[0,t]$. The phase is then given by

$$\phi = \frac{1}{\hbar}\int_0^t (T - V)\mathrm{d}t \; . \tag{5.32}$$

For the perturbed trap, we have to solve the following integral

$$\phi = \frac{m}{2\hbar}\int_0^t \left(\dot{x}^2 - \omega_0^2 x^2 + \frac{\omega_0^2}{w_0^2}x^4\right)\mathrm{d}t \; . \tag{5.33}$$

We would set $x = x_0 + x_1$ and $\dot{x} = \dot{x_0} + \dot{x_1}$ in the integrand, but as we only consider small perturbations in α_β, we find that the terms with x_1 do not contribute to ϕ when considering terms up to quartic order in α_β. The integral vanishes for quarter-period evolution in a harmonic trap, but we get contributions from the slightly mismatched integration time $\tau = T/4 + \gamma$ for $\gamma \neq 0$ and from the quartic potential. We substitute $u = \omega t$ and set integral boundaries to $[0, \pi/2(1 - 3/4\alpha_\beta^2 + 3/4\gamma\alpha_1^2]$, which we introduced to vary the time around the effective $T/4$-time. The phase for a particular momentum is then given by

$$\begin{aligned}
\phi_\beta = \frac{m w_0^2 \omega_0}{2\hbar}\int_0^{\frac{\pi}{2}(1-\frac{3}{4}\alpha_\beta^2+\frac{3}{4}\gamma\alpha_1^2)} & \frac{1}{2}\alpha_\beta^2\left(\cos^2(u) - \sin^2(u)\right) \\
& - \frac{1}{8}\alpha_\beta^4\left(-4\sin^4(u) + 3\sin^2(u) + 3\cos^2(u)\right) \\
& + O\left(\alpha_\beta^5\right)\mathrm{d}u
\end{aligned} \tag{5.34}$$

$$\begin{aligned}
= \frac{m w_0^2 \omega_0}{2\hbar \cdot 128} \Bigg(& 3\pi\alpha_\beta^2(-3\gamma\alpha_\beta^2 + 3\alpha_\beta^2 - 4) - 2\alpha_\beta^2 \sin\left(\frac{3}{2}\pi(\alpha_\beta^2 - \gamma\alpha_1^2)\right) \\
& - 16\left(\alpha_\beta^2 - 2\right)\sin\left(\frac{3}{4}\pi(\alpha_\beta^2 - \gamma\alpha_1^2)\right)\Bigg)
\end{aligned} \tag{5.35}$$

$$\approx \frac{m w_0^2 \omega_0}{2\hbar}\alpha_\beta^2\left(-\frac{3\left(\pi\gamma\right)\alpha_1^2}{8} + O\left(\alpha_1^4\right)\right) + \alpha_\beta^4\left(\frac{3\pi}{16} + \frac{3\pi\gamma\alpha_1^2}{32} + O\left(\alpha_1^4\right)\right) + O\left(\alpha_\beta^5\right) \tag{5.36}$$

$$\approx \frac{m w_0^2 \omega_0}{2\hbar}\left(-\frac{3\pi\gamma\alpha_1^2}{8}\alpha_\beta^2 + \frac{3\pi}{16}\alpha_\beta^4\right) \tag{5.37}$$

where we expanded the sine around zero in α_β^2 and α_1^2, while keeping only quartic orders also in their product $\alpha_\beta^n\alpha_1^m$ with $m + n \leq 4$. With this, we get a phase evolution of a particular k-vector when imaging at times around the focusing condition, where the phase of the first Bragg equals that of zero momentum. We will consider the accumulated phase ϕ_β now in terms of momentum via the dimensionless constant β in the following form

$$\phi_\beta = -\frac{3\pi}{8}\alpha_1^4\tilde{\phi}\gamma\beta^2 + \frac{3\pi}{16}\alpha_1^4\tilde{\phi}\beta^4 = -1.784\pi\gamma\beta^2 + 0.892\pi\beta^4, \tag{5.38}$$

where $\tilde{\phi} = \frac{m w_0^2 \omega_0}{2\hbar}$. We find the focusing condition, where the zero-momentum and first-order Bragg peak have equal phase, for $\beta = 1$ at $\gamma = 0.5$.

Here, we used typical values according to our experimental parameters. With a trap frequency $\omega_0 = 2\pi \times 1.25\,\mathrm{kHz}$ and a $1/e^2$ waist radius $w_0 = 41\,\mu\mathrm{m}$ for the Gaussian beam profile, we have $A_1 = 11.82\,\mu\mathrm{m}$ after a quarter period. The dimensionless prefactor at the first Bragg peak becomes $\alpha_\beta = \alpha_1\beta = A_\beta/w_0\beta = 0.283\beta$ and the pre-factor $\tilde{\phi} = 742.1$. The accumulated phase for an effective $T/4$-pulse is shown in figure 5.4(a) as well as a comparison with a phase imprinting approach resulting in a Heaviside-function. When the phase difference between zero-momentum and b vanishes, i.e., when $\phi_0 = \phi_1$, the lattice has maximal contrast. This is given at the effective quarter-period time given by $\gamma = 0.5$. The effective quarter-period is a fraction of $\gamma\epsilon_1 = 0.031$ longer than the bare harmonic quarter-period. This matches well to the fraction of 0.036 longer time that we find in the numerical simulations (Sec. 5.2.2). We find a minimum of the phase accumulation of -0.24π at $\beta = 1/\sqrt{2}$. This will result in a maximal conversion between phase and density fluctuation for phase-fields with a modulation frequency $b/\sqrt{2}$ for homogenous densities.

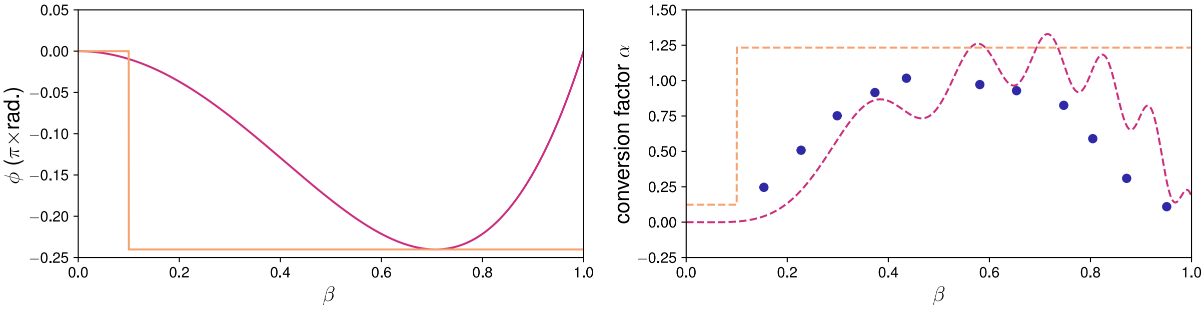

Figure 5.4: Accumulated phase and conversion factor. Momentum dependent conversion between phase and density. (Left) The acquired phase from the matter-wave aberrations is momentum dependent and goes to zero at the reciprocal lattice vector b (purple line). The phase imprinted by the phase mask is shown for comparison (orange line). (Right) The conversion factor α from initial phase fluctuations to measured relative density fluctuations is momentum dependent, but similar in both cases (dashed lines, same colors as on the left). In addition to the analytical results, we plot data retrieved from numerics (blue discs), which simulate the evolution of the system close to experimental parameters. We find a good agreement between the analytic theory and the numerical simulations.

5.2.1 Mapping the phase to density

Revealing the phase of the wavefunction as envisioned in [104] relies on the k-dependent interference of the wavefunction with itself. The simplest case is analogous to the technique used in phase contrast imaging. In the Fourier plane, i.e. momentum space, a phase mask is added to the wavefunction before it gets transformed back to real space. To reveal the phase profile of the initial system, the zero-momentum part is used as an interference reference by changing its phase with respect to the other momenta. The idea here is easily understood when approximating the phase in the wavefunction $\psi = \sqrt{n_0}e^{i\theta(x)}$ for small phase variations as

$$\psi(x) \propto e^{i\theta(x)} \approx 1 + i\theta(x). \tag{5.39}$$

We Fourier-expand $\theta(x) = \sum \theta_k e^{ikx}$ and assume a global phase of $\theta_0 = 0$. The phase imprinting to the zero-momentum will only manipulate the first term,

$$\tilde{\psi}(x) = e^{i\phi_0} + \sum_{k \neq 0} \theta_k e^{ikx} = e^{i\phi_0} + i\theta(x). \tag{5.40}$$

With this, the constant part has an imaginary part and will interfere with the complex phase part. The resulting density is modulated by the phase profile $\theta(x)$ via

$$\tilde{n}(x) = |\tilde{\psi}(x)|^2 = n_0(1 - 2\sin(\phi_0)\theta(x) - \theta^2(x)). \tag{5.41}$$

The comparison with the non-manipulated density n_0 allows us to extract the initial phase profile from the manipulated density $\tilde{n}(x)$ through

$$\frac{\tilde{n}(x) - n_0}{n_0} = -2\sin(\phi_0)\theta(x), \tag{5.42}$$

here we neglect the quadratic term in $\theta(x)$ as we consider only small phase fluctuations. The relative density reveals the phase with a conversion factor $\alpha = -2\sin(\phi)$. The approach relies on small phase fluctuations and sufficient population of the zero-momentum state, the BEC. When phase fluctuations get too strong and the zero-momentum population is reduced, the mapping breaks down. We assumed a global phase offset of $\theta_0 = 0$, which in hindsight is reasonable because the interference with the zero-momentum part cancels. With this approach, a measurement of the order parameter of the BEC, its phase, is not possible.

A special case we consider here is that of a lattice. The modulated density leads to a reduced conversion factor as we will lay out. To illustrate this, we assume a density modulation of the form $\psi(x) \propto e^{i\theta(x)}(c_0 + 2c_1\cos(bx))$, where c_0 and $c_1 = c_{-1}$ are the first Bloch coefficients of the lattice structure and b is the lattice vector given by $b = 2\pi/a_{1\mathrm{D}}$. As above, we manipulate the wavefunction in the Fourier plane by adding a phase to the zero-momentum, which will add a phase to Bloch coefficient c_0:

$$\begin{aligned} \psi(x) &\propto (1 + i\theta(x))(c_0 + 2c_1\cos(bx)) && (5.43)\\ &= c_0 + ic_0\theta(x) + 2c_1\cos(bx) + 2i\theta(x)c_1\cos(bx) && (5.44)\\ \rightarrow \tilde{\psi}(x) &= c_0 e^{i\phi_0} + ic_0\theta(x) + 2c_1\cos(bx) + 2i\theta(x)c_1\cos(bx) && (5.45) \end{aligned}$$

From this we can already see that the relative density modulation as in 5.42 will be only scaled by the zero Bloch coefficients c_0, which gives

$$\alpha = -2\sin(\phi)c_0^2. \tag{5.46}$$

With increasing lattice depth, the conversion between phase and relative density fluctuations is suppressed and matches the limit for $c_0 \rightarrow 1$ for no modulation.

This simple and idealistic case needs to be adapted to the experimental settings. Using matter-wave optics to transform between real and momentum space, it is possible to imprint a phase onto a particular momentum, e.g. the zero-momentum of the system. One option to imprint a phase onto the wavefunction of the atoms is by using the atom-light interaction. A laser beam focused on the zero-momentum position for a pulsed time around $T/4$ creates an accumulated phase with respect to the non-illuminated region. This technique is well established in the quantum gas community[131]. The finite extent of the optical potential has to be taken into account, as well as the finite time the potential is active, while the wavefunction is in momentum space, i.e. very fine control is needed here. The mapping from phase to density in our system does not need an additional external light potential. The aberrations in the matter-wave lens create a momentum-dependent phase in the Fourier plane, while the second matter-wave lens, i.e. the free expansion, is nearly aberration free. The mainly quartic aberration leads to an accumulation of a phase as estimated in (5.38). With the smooth change in phase, the conversion factor is not reduced only to the zero-momentum component. We calculate the mapping for the modulated density in the following. We Fourier-expand the phase field to

$$\theta(x) = \int_{\beta=0}^{1} (a_\beta \cos(\beta b x) + b_\beta \sin(\beta b x)) \tag{5.47}$$

with the real valued Fourier components a_β and b_β. We restrict the integral from zero to the lattice momentum, due to the effective sampling on the lattice, i.e. due the Nyquist theorem. We substitute the Fourier expansion into 5.43 and obtain

$$\begin{aligned} \psi(x) &\approx c_0 + c_1 \cos(bx) && (5.48)\\ &+ i \int_{\beta=0}^{1} [c_0(a_\beta \cos(\beta b x) + b_\beta \sin(\beta b x)) && (5.49)\\ &\qquad + 2c_1(a_\beta \cos(bx)\cos(\beta b x) + b_\beta \cos(bx)\sin(\beta b x))]\, d\beta, && (5.50) \end{aligned}$$

where β is a dimensionless factor describing the momentum $p_\beta = \beta \hbar b$. The wavefunction with the accumulated phase is

$$\begin{aligned} \tilde{\psi}(x) \propto\ & c_0 e^{i\phi_0} + 2c_1 e^{i\phi_1} \cos(bx) \\ &+ i \int_{\beta=0}^{1} \Big[c_0 e^{i\phi_\beta} [a_\beta \cos(\beta b x) + b_\beta \sin(\beta b x)] \\ &\qquad + c_1 e^{i\phi_{1+\beta}} [a_\beta \cos((1+\beta)bx) + b_\beta \sin((1+\beta)bx)] \\ &\qquad + c_1 e^{i\phi_{1-\beta}} [a_\beta \cos((1-\beta)bx) - b_\beta \sin((1-\beta)bx)] \Big]\, d\beta. \end{aligned}$$

Here we set $\phi_0 = 0$ and neglect terms quadratic in a_β and b_β as well as terms with wave vector outside $[0, b]$. With this we obtain a density

$$\begin{aligned} |\psi(x)|^2 &= c_0^2 + 4c_0 c_1 \cos(\phi_1)\cos(bx) + 4c_1^2 \cos^2(bx) + \int_{\beta=0}^{1} \alpha_\beta \left[a_\beta \cos(\beta b x) + b_\beta \sin(\beta b x)\right] d\beta \\ &= [c_0 + 2c_1 \cos(bx)]^2 + \int_{\beta=0}^{1} \alpha_\beta \left[a_\beta \cos(\beta b x) + b_\beta \sin(\beta b x)\right] d\beta \end{aligned}$$

with the momentum-dependent conversion factor

$$\alpha_\beta = -2c_0^2 \sin(\phi_\beta) - 2c_1^2 \sin(\phi_{1+\beta} - \phi_1) - 2c_1^2 \sin(\phi_{1-\beta} - \phi_1). \tag{5.51}$$

With this, we can compare the two methods in their conversion factor depending on the momentum. The calculated phases result in a conversion factor shown in figure 5.4. The lattice and phase-accumulated version describes a smooth momentum dependence, whereas the phase-imprinting gives a sharp jump. In the former, oscillations of the conversion factor are present as the terms in 5.51 all depend on the phase over different momenta, here considered up to $\beta = 2$. Above $\beta = 1$ the quartic term dominates, leading to stronger oscillations. In the range $\beta \in [0.3, 0.9]$ the phase can be assumed approximately constant, which is essential for the experimental implementation as this allows to define an averaged conversion factor. The range also includes the maximal phase accumulated from the aberrations at $\beta = 0.71$. The Bloch coefficients used in figure 5.4 are $c_0 = 0.9$ and $c_1 = 0.9$, which approximately describe the density used in the following numerical simulations.

For a 2D system, as in the experiment, the situation is qualitatively similar, but the calculations become more involved. We therefore calibrate the conversion factor experimentally, as follows. We use the expected temperature dependence of the extracted phase fluctuations and find a conversion factor of $\alpha = 0.35(3)$. It can be assumed constant for our range of lattice depths and for the wave vectors of the phase fluctuations corresponding to distances up to three sites that we evaluate below. For the experimental lattice depths, $V_0 = 1.7\ \mathrm{E_{rec}}$ to $3.7\ \mathrm{E_{rec}}$, we obtain the following Bloch coefficients from the band structure calculation: $c_0 \in [0.6134, 0.5135]$, $c_1 \in [0.3056, 0.3151]$, and $c_2 \in [0.0885, 0.1376]$. For a typical value of $c_0 = 0.56$, we get with the estimate for the conversion factor $\alpha = -2\sin(\phi_{\max})c_0^2 = 0.43$ with the phase set to a maximal magnitude of $\phi_{\max} = -0.24\pi$. This matches well with our calibrations.

5.2.2 1D-simulation in a Gaussian trap

To corroborate our analytical model, we perform numerical simulations of a one-dimensional system. We evolve the density-modulated wavefunction by solving the Gross-Pitaevskii equation (GPE)[132, 133] with the split-step method [134]. The GPE is given by

$$i\hbar \frac{\partial \Psi(\boldsymbol{r}, t)}{\partial t} = \left(-\frac{\hat{p}}{2m} + V(\boldsymbol{r}) + g \left| \Psi(\boldsymbol{r}, t) \right|^2 \right) \Psi(\boldsymbol{r}, t), \tag{5.52}$$

where g is the inter-particle interaction. The time evolution of the wavefunction $\Psi(\boldsymbol{r}, t)$ is computed with the time evolution operator $U(t) = \exp(-i\hat{H}t/\hbar)$. The time evolution is split into two parts of the Hamiltonian, one acting in momentum space $\hat{H}_k$ and the other in real space $\hat{H}_r$. With the Baker-Campbell-Hausdorff formula and strang splitting, the time evolution becomes

$$\Psi(\boldsymbol{r}, t + \mathrm{d}t) = \left(e^{\frac{-i\hat{H}_r dt}{2\hbar}} e^{\frac{-i\hat{H}_k dt}{\hbar}} e^{\frac{-i\hat{H}_r dt}{2\hbar}} \right) \Psi(\boldsymbol{r}, t) + \mathcal{O}(dt^3) \tag{5.53}$$

with only a third-order error in $\mathrm{d}t$. The time evolution operators can now be implemented numerically on a vector grid, and the algorithm alternates between momentum and position space with fast Fourier transforms.[4]

---

[4] A great introduction to the split-step method with simple numerics can be found in [134]

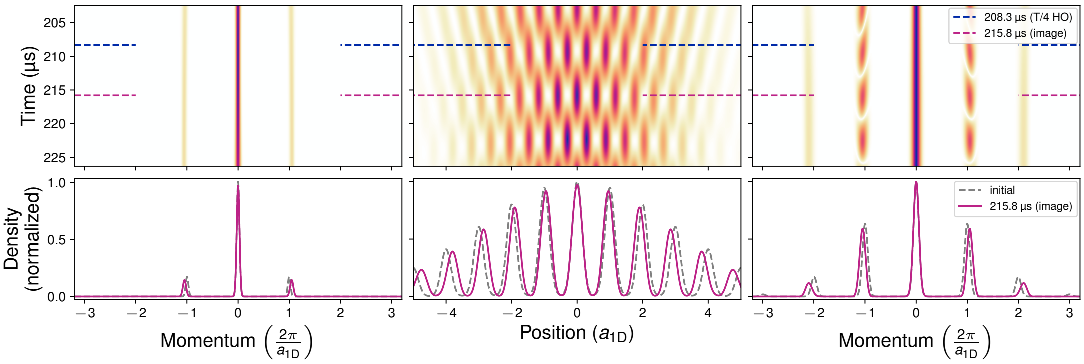

Figure 5.5: Numerical simulation of the aberration-induced phase microscope.. (A) Density of the wave function after evolution in the Gaussian trap for times around the $T/4$-time in a harmonic trap ($T_4 = 208.3\,\mu\mathrm{s}$, blue dashed line) and the imaging condition including the aberrations ($T_{4,\mathrm{eff}} = 215.8\,\mu\mathrm{s}$, red dashed line). (B) Density of the wave function, when the stated time evolution in the Gaussian trap is continued by a time evolution in a harmonic trap for $T_{4,2} = 208.3\,\mu\mathrm{s}$ to complete the matter-wave protocol. The imaging condition leads to a sharp lattice structure. The sharp lattice structures shifted out of phase, which occur around $\pm 6.5\,\mu\mathrm{s}$ from the imaging condition, are the first secondary Talbot revival (positive) and its negative counter-part. (C) The absolute value of the Fourier transform of the final density shows the strongest Bragg peaks for the sharp lattice structures. In between, the Bragg peaks vanish in a way that gives rise to a double peak, which we identify as a finite size effect. The two halves of the peaks are out of phase and can cancel each other out. (D) Density profile at the evolution time of $215.8\,\mu\mathrm{s}$ in the Gaussian trap (purple) and Fourier transform of the initial density (gray dashed). (E) Density profile after the full matter-wave protocol (purple) and the initial density for comparison (gray dashed). The Wannier functions on the lattice sites are broadened due to the aberrations in the matter-wave protocol. The matter-wave image is slightly demagnified due to the longer evolution time to compensate for the aberrations. (F) The absolute value of the Fourier transform of the density profiles in (E) also illustrates the slight demagnification.

Here we use a grid of 10^5 points with a spacing of $2\,\mathrm{nm}$. This minimizes boundary effects. The lattice vectors can quickly introduce momenta at the edge of the system, which then get reflected back, causing large errors. For simplicity, we work with SI units but find no significant errors introduced by floating-point variations. A change to a matching atomic unit system would probably increase computation speed and render 2D simulation feasible. For the numerical simulations presented, we model the wavefunction Ψ as a sum of Gaussian wavepackets of width $\sigma_{\mathrm{wp}} = 130\,\mathrm{nm}$ with an overall Gaussian envelope matching our system size $\sigma_{\mathrm{env}} = 3\,a_{1\mathrm{D}}$,

$$\Psi(x) \propto \exp(-\frac{x^2}{2\sigma_{\mathrm{env}}^2}) \left(\sum \exp(-\frac{(x - n a_{1\mathrm{D}})^2}{2\sigma_{\mathrm{wp}}^2})\right). \tag{5.54}$$

We use the 1D lattice spacing $a_{1\mathrm{D}}$ between neighboring wavepackets (Fig. 5.5). The width of the wavepackets is on the order of the onsite harmonic oscillator length for the relevant trap depth range of $1.7\,E_{\mathrm{rec}}$ to $3.7\,E_{\mathrm{rec}}$.

The initial wavefunction resembles the wavefunction in the lattice at the instance, where the potential is switched off. As in the experiment, we perform the matter-wave protocol, but here now numerically. We subject the wave function to the anharmonic potential of the first matter-wave lens, a Gaussian potential,

$$V(x) = V_1 \exp(-2x^2/w_0^2), \tag{5.55}$$

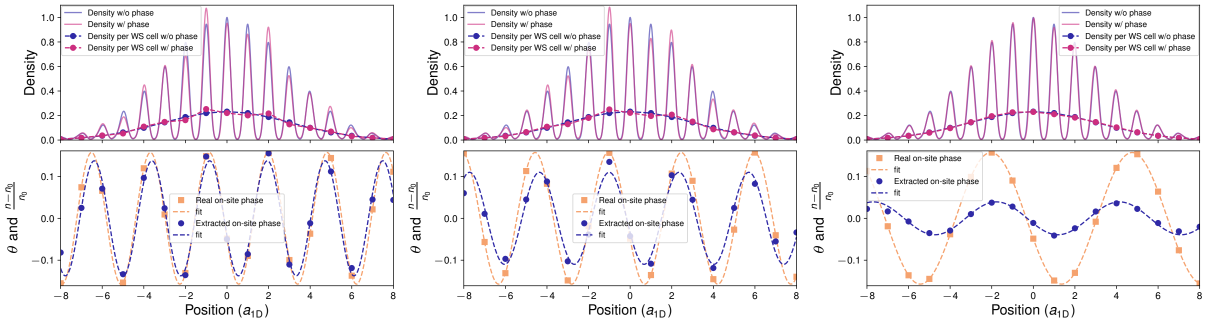

Figure 5.6: Numerical determination of the momentum-dependent conversion factor. (Top row) Determination of the conversion factor for an example phase profile of wavevector $k_\theta = 2\pi/(a_{\mathrm{phase}})$ with $a_{\mathrm{phase}} = 2.8, 3.5$ and $6.8\,a_{1\mathrm{D}}$ (left to right). Density after the matter-wave protocol with the phase profile (purple) and with constant phase (blue) to calculate the deviation. The data points give the densities integrated over the Wigner-Seitz cells (adapted to the slight demagnification). (Bottom row) Phase profile extracted from the relative density profile (purple) together with the initial density profile (blue) (adapted to the slight demagnification). We extract the conversion factor $\alpha \approx 1.0,\ 0.75$ and 0.25, respectively, to make the two amplitudes match. The slight shift in the wavevector is also visible.

where w_0 is the $1/e^2$-radius of the waist of the beam, and we set the potential depth to $V_1 = -(1/4)m\omega_0^2 w_0^2$. This matches the trap frequency at the center with its respective harmonic potential. We use a harmonic trapping frequency of $\omega_0 = 2\pi \times 1.2\,\mathrm{kHz}$ and a waist $w_0 = 42\,\mu\mathrm{m}$. As the second matter-wave lens, we use a pure harmonic potential of the same trapping frequency, replacing the free expansion in the experiment. Using a free expansion instead of a harmonic potential introduces only a small deviation in the resulting momenta[84]. The choice of matching the trap frequencies of the two lenses gives a magnification of order one and makes the numeric implementation less demanding because the extension of the wavefunction remains restricted mainly to the initial extent. We are now interested in the evolution of the wavepacket around the effective quarter period time $T_{4,\mathrm{eff}}$ of the anharmonic trap. We expect the effective time to be delayed compared to the respective bare quarter period $T_4 = 208.3\,\mu\mathrm{s}$ by about a factor $\gamma\epsilon_1 = 0.031$. This gives an effective quarter period of $T_{4,\mathrm{eff}} \approx 214.8\,\mu\mathrm{s}$. The numeric evolution of the wavefunction is split into three parts: an initial propagation in the anharmonic trap up to a time $t_1 < T_{4,\mathrm{eff}}$, a continued propagation in the anharmonic trap to time $t_2 > T_{4,\mathrm{eff}}$, where the wavefunction is stored for each intermediate evolution step, and a final propagation in the harmonic for exactly T_4. The final propagation is performed for all stored intermediate wavefunctions separately. A propagation from $t_1 = 202.33\,\mu\mathrm{s}$ to $t_1 = 226.33\,\mu\mathrm{s}$ is shown in figure 5.5. From the maximal overlap with the initial density, we find an effective quarter period time $T_{4,\mathrm{eff}} \approx 215.8\,\mu\mathrm{s}$, i.e. a factor of 0.036 longer in good agreement with the estimated value. The longer effective quarter-period introduces a slight demagnification of the density of $M = 0.96$. The propagation for times around the quarter period also reveals the Talbot effect of the released periodic wavefunction in the anharmonic trap. The timing of the secondary Talbot revivals in the simulation matches the expected value of $t_{\mathrm{T},a_{1\mathrm{D}}}/2 \approx 6.5\,\mu\mathrm{s}$ very well. The numerical simulation reproduces also a finite size artifact, which we found in the experimental data. The intensity around the Bragg peaks is split by a phase jump between revivals when taking the Fourier transform of the final density. This effect vanishes when simulating larger system sizes.

To simulate the influence of a phase profile, each initial wavepacket is multiplied with an individual phase. Here we only propagate for the found $T_{4,\mathrm{eff}}$-time, the imaging time, in the anharmonic potential. The final propagation in the harmonic trap remains the same. In figure 5.6 we compare the resulting density profiles with an additional phase modulation with those without one. As expected we see an increase/decrease in density for a lattice site with an initial positive/negative phase. We also observe a reduction of that mapping as we increase the modulation length to longer wavelengths. We extract the relative density deviation $\nu = (N_i - \bar{N}_i)/\bar{N}_i$, where N_i is the integrated density per Wigner-Seitz cell with a non-zero phase profile and $\bar{N}_i$ without one. When comparing the extracted phase profile to the original one, we take into account that the matter-wave protocol inverts the image and also account for the small demagnification. We fit the extracted relative density deviation with a cosine and compare its amplitude to the amplitude of the imprinted phase modulation. The resulting ratios are plotted with the computed values by the aberration of the anharmonic trap in figure 5.4. Beside the momentum dependent conversion factor we find a reduction of the wavelength of the mapped phase modulation with increasing wavelength. This is possibly caused by the effectively momentum dependent demagnification in the Gaussian trap. The effective quarter period found here is that of the first lattice momenta. The effect of the anharmonicity of the Gaussian potential becomes stronger for larger momenta, leading to larger effect quarter periods, i.e. stronger demagnification in this setting. We find good agreement between the numerical and analytical methods.

5.3 | Phase extraction

As we have shown in section 5.2, the anharmonic shape of our matter-wave lens realizes a mapping from phase fluctuation to density fluctuation, and the phase fluctuations are the direct observable for the BKT-transition. We now extract the phase for each lattice site. The data analysis to confirm the viability of our approach is a self-consistent estimate of the relevant scales. We begin with the extraction of the onsite population. As in the coherence carpet measurements we measure in the range of $V_0 = 1.7$ to $3.7\,E_{\mathrm{rec}}$, this time only along the image branch. Each data point is measured 100 times to fit a mean density profile, which will be a Gaussian distribution. With almost no interaction and large trap frequency the use of the harmonic-oscillator ground state distribution is motivated instead of using the Thomas-Fermi approximation. From the comparison of single-shot and mean onsite densities, we get the relative onsite densities, which we will convert to the phase of the lattice site. To estimate the conversion factor α, we use phase thermometry[135].

Onsite population To extract the onsite population, we follow the approach used in [21]. Initially, we use the OD-images to find the lattice constant and the rotation of the lattice with respect to the pixel grid of the camera. This is done by rotating the image and successively integrating along one axis. The integrated density is fitted by a heuristic model of a lattice modulation by a Gaussian potential as an envelope. The lattice modulation will be strongest when the integration is perpendicular to one of the reciprocal lattice vectors $\boldsymbol{b}_i$. This yields the rotation and the lattice constant of the particular lattice vector. With an average lattice constant of $a_{\mathrm{2D,M}} = 11.57(18)\,\mathrm{px} = 25.06(38)\,\mathrm{\mu m}$ and an expected lattice constant of $a_{\mathrm{2D}} = 709\,\mathrm{nm}$, we get a matter-wave magnification of $M_{\mathrm{mw}} =$

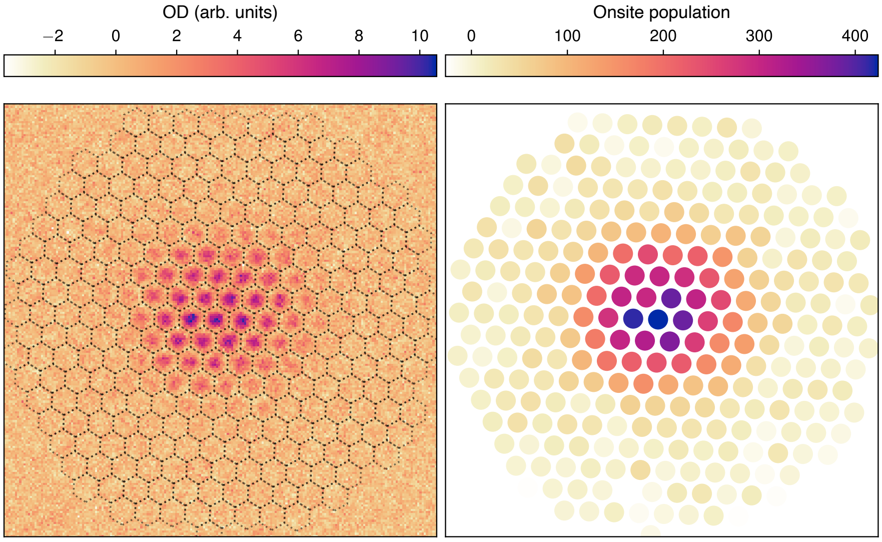

Figure 5.7: Extraction of onsite population. (Left) Exemplary OD image of the magnified lattice on the image branch. We overlay the triangular lattice with hexagonal Wigner-Seitz (WS) cells. The position and rotation is optimized as described in the main text. The colormap is in atoms per pixel. (Right) We integrate the atomic density in each WS cell and obtain the onsite population visualized here. The colormap represents the atom number per lattice site.

$35.33(53)$. With respect to the pixel grid of the camera, the lattice is rotated by $-1.5(5)^\circ$. This analysis also recovers the slight misalignment of the laser beam along $\boldsymbol{k}_1$ of $1.5(5)^\circ$ with respect to the other two beams. With the magnified lattice constant and the rotation, we create an array of Wigner-Seitz (WS) cells. To match the shot-to-shot fluctuation in the positional phase of the lattice potential, we maximize the integrated value of the OD in half-sized WS-cells. The onsite populations are then extracted by integrating over the optimally positioned WS cells. Here, we increase the pixel resolution artificially by a factor of four to reduce allocation errors at the edge of the WS cells.

We fit the distribution of onsite population N_i with eq. 2.6. The fit to the sample image from above is shown in figure 5.8. Here we refrain from a step-wise fit routine, because the thermal fraction should be very small at these low temperatures. We are not able to make out any significant thermal fraction above the noise floor of approximately ten atoms per pixel. Additionally, the in-situ density distribution of the thermal and condensed part overlap. The single run may stand only as an example, as we proceed with taking all available data for one lattice depth to get an average signal. Especially for the deeper lattices this is of essence as here the phase fluctuations lead to large density fluctuations and the fit to a single image would not match the actual in-situ density. The result for two exemplary lattice depths are given in figure 5.8. We assume that this average density profile $\bar{N}_i$ of 100 iterations per lattice depth matches the in-situ density very well. With this we can define the relative density fluctuations per lattice site as

$$\nu_i = \frac{N_i - \bar{N}_i}{\bar{N}_i}, \tag{5.56}$$

where the index i denotes a single lattice site. The total atom number N, the mean atom number in the central Wigner-Seitz cell N_0 and the Gaussian width of the cloud are plotted in figure 5.9 as a function of the lattice depth V_0.

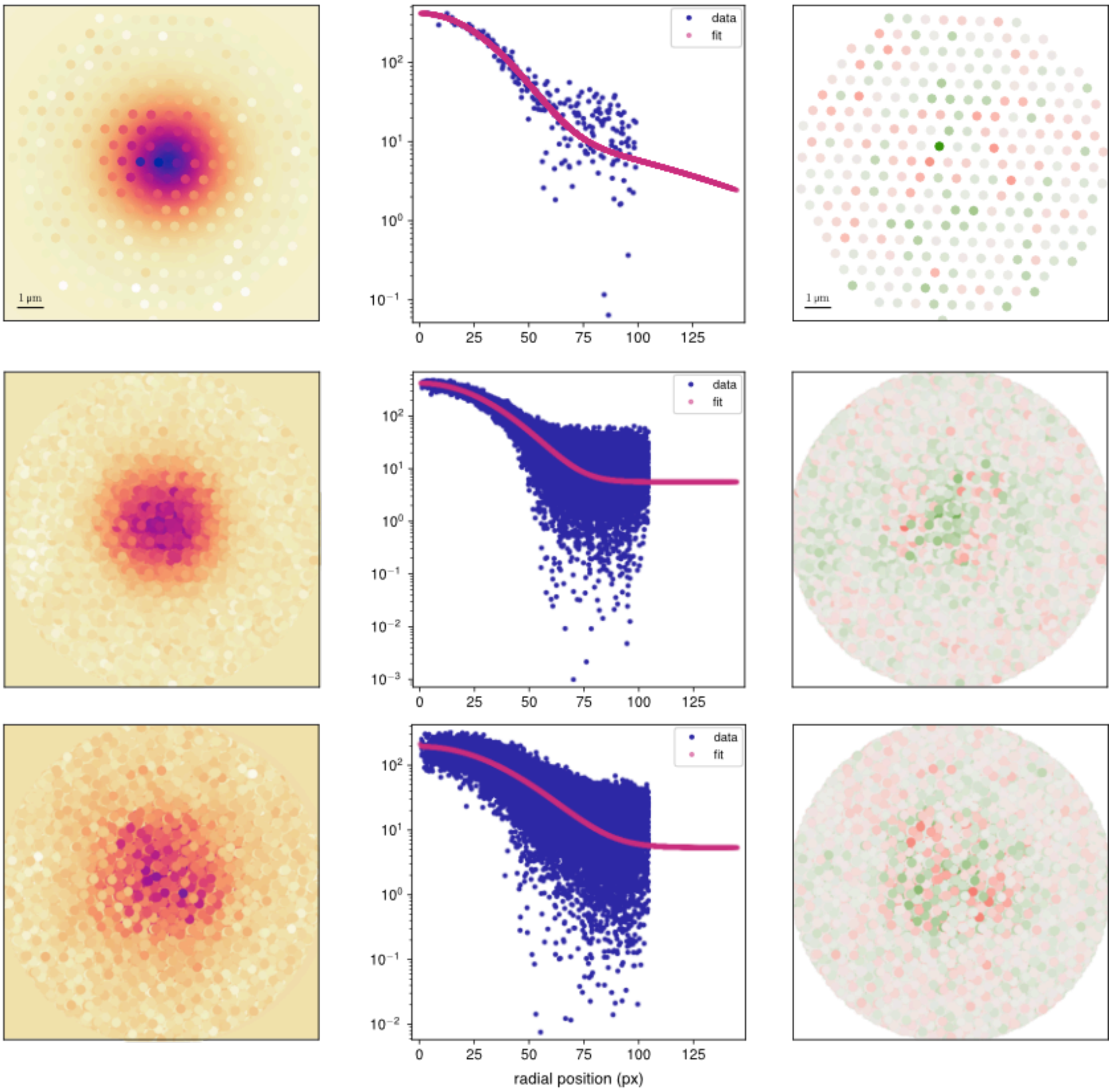

Figure 5.8: Determination of the mean density profile. To the extracted onsite population we fit a bi-modal distribution. (Top) The left column shows the exemplary onsite distribution from figure 5.7 represented as scatter-dots above the fitted density distribution. The middle column shows the radially integrated signal, visualizing the matching fit. The right column shows the density deviation between the fit and the measured data (red negative deviation, green positive, single image ± 50 atoms, averaged images ± 150 atoms). (Middle row) Here, we take all onsite populations from the 100 iteration of a single lattice depth to obtain a good mean density profile. Columns same as above. The top and middle row have $V_{\mathrm{lat}} = 2.0\,E_{\mathrm{rec}}$, the bottom row has $V_{\mathrm{lat}} = 3.1\,E_{\mathrm{rec}}$.

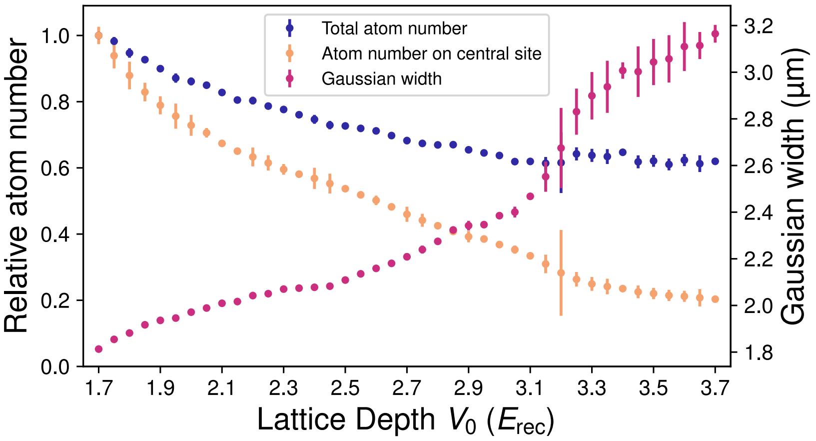

Figure 5.9: Atom numbers and system size. Relative total atom number N (blue), relative atom number in the central Wigner-Seitz cell N_0 (orange) and $1/e^2$-Gaussian width of the cloud (purple) as a function of the lattice depth V_0. The maximum values of the atom numbers are $N_{\max} = 14,743$ and $N_{0,\max} = 567$.

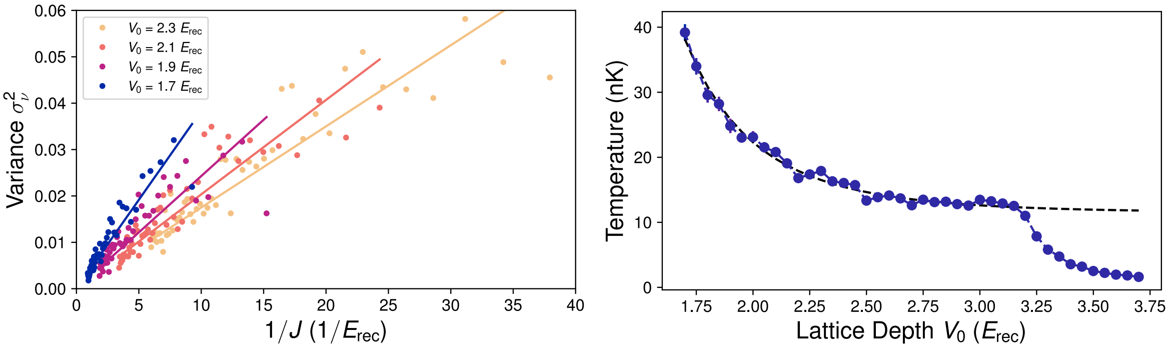

Figure 5.10: Variance of relative density fluctuation and extracted temperature. (Left) Measured variance of the relative density fluctuations σ_ν^2 as a function of the inverse of local tunnel coupling $1/J$ for example lattice depths of $V_0 = 1.7, 1.9, 2.1$ and $2.3\,E_{\mathrm{rec}}$. We fit the slopes for each lattice depth and extract the temperature, which is shown on the right.

Phase thermometry The phase thermometry is based on the assumption that for $T \ll J$ the phase fluctuations are given by $\langle \Delta\phi^2 \rangle = k_{\mathrm{B}}T/J$ [135, 136]. This holds for lattice depths with about $V_0 = 3\,E_{\mathrm{rec}}$, if we assume a temperature of $T = 50\,\mathrm{nK}$ as measured at the end of the evaporation. The relative density fluctuations σ_ν are directly proportional to the phase fluctuations $\Delta\phi = \sigma_\nu/\alpha$, i.e. we expect a linear dependence in $1/J$. For each lattice depth, we determine the local multi-particle tunneling element with $J = 2K\bar{N}_i$ and plot the relative density fluctuations σ_ν against $1/J$ (Fig. 5.10). Each data point is a J-binned average located at the bin center. The exemplary lattice depth in figure 5.10 shows a clear linear correspondence. We perform a linear fit and extract the slope τ for each lattice depth. From the slopes τ, we get the temperature via $T(V_0) = c_\tau \tau(V_0)$ with the scaling factor c_τ. We parameterize the slopes $\tau(V_0)$ with the single-particle tunneling $K(V_0)$. We choose a polynomial model of the form

$$\tau(V_0) = a_0 + a_1 K(V_0) + a_2 K(V_0)^2, \tag{5.57}$$

which is motivated by the expectation that the temperature scales linearly with the single particle tunneling, $T(V_0) \propto K$ for an adiabatic ramp of the lattice depth[137]. The additional quadratic term is added to account for non-adiabaticity, e.g. due to three-body losses. We take the above approximation as the limit ($V_0 = 3\,E_{\rm rec}$) for the data used in the fit. The fit results in the following parameters: $a_0 = 0.0011\,E_{\rm rec}$, $a_1 = 1.7$, and $a_2 = 970\,1/E_{\rm rec}$. We use this parameterization to extrapolate to deeper lattices and determine the scaling factor c_τ via the condition $(k_{\rm B}T/J)|_{V_0=V_c} = 0.898$. We use the critical lattice depth found in the coherence carpet measurement of $V_c = 3.25\,E_{\rm rec}$ and the largest value in J of this lattice depth, i.e. at the center of the density distribution. With this, we get

$$c_\tau = J/\tau|_{V_0=V_c} \times 0.898 \approx 8.5. \tag{5.58}$$

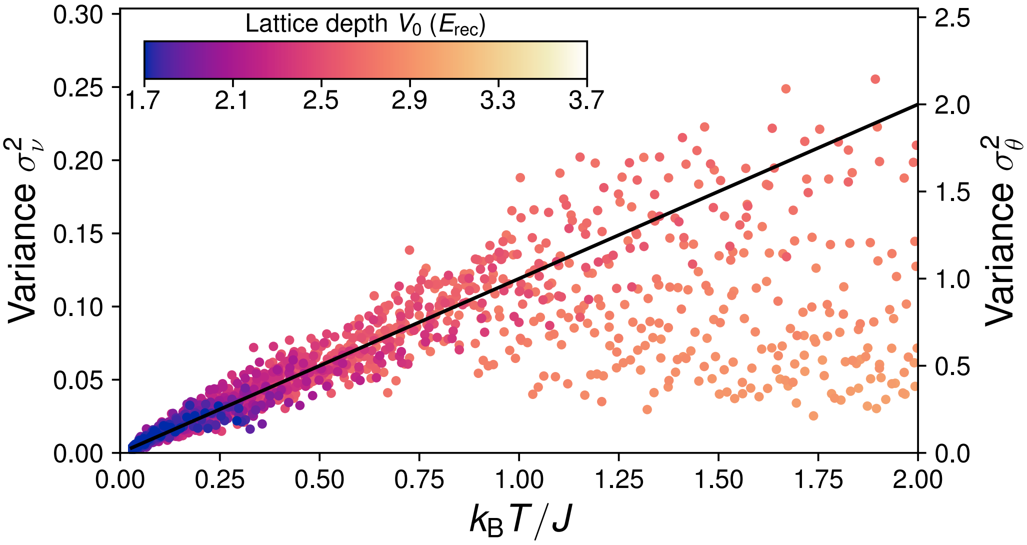

Figure 5.11: Experimental calibration of the conversion factor. With the temperature curve in figure 5.10 the variance data of the relative densities collapse to a single line when plotted against the scaled temperature $k_{\rm B}T/J$. We fit this slope and enforce $\sigma_\theta^2 = k_{\rm B}T/J$ onto it. With this, we get the conversion factor of $\alpha = 0.345(1)$.

The rescaled temperature is shown in fig. 5.10 with the rescaled parametrization. With the temperature $T(V_0)$, we can scale the $1/J$-axis to $k_{\rm B}T/J$, and all variances with small $k_{\rm B}T/J$ collapse to a single line (Fig. 5.11). This confirms the expectation of $\sigma_\nu^2/\alpha^2 = \Delta\theta^2 \simeq k_{\rm B}T/J$ for thermal phase fluctuations in the XY model [94, 136]. At the phase transition, the condition $k_{\rm B}T/J = 0.898$[126] allows us to fix not only the temperature curve but also to determine a global conversion factor α between the relative density fluctuations σ_ν and the phase fluctuations $\Delta\phi$. We perform a linear fit to all variances with $V_{\rm lat} < 3\,E_{\rm rec}$ and obtain a value of

$$\alpha = 0.345(1). \tag{5.59}$$

In addition to the statistical error, we estimate a systematic error of $10\,\%$ due to the uncertainty in the calibration of atom number. This is in good agreement with estimates from section 5.2. With parameters close to our experimental setting, we obtain an estimate of the aberration-induced phase imprint of $\phi_{\rm max} = -0.24\pi$ and Bloch an average coefficient $c_0 = 0.56$, yielding a conversion factor $\alpha \approx -2\sin(\phi_{\rm max})c_0^2 = 0.43$. With the conversion factor, we are able to convert the relative density deviation into a phase for each lattice site. The density fluctuation due to increasing $k_\mathrm{B}T/J$ was already visible in the coherence carpet measurement along the image branch. Here, we show them now as phase fluctuations (Fig. 5.12). These are exemplary images, and each configuration looks different, especially approaching the phase transition. At and beyond the phase transition, we have to note that the mapping breaks down as we are only able to measure small phase fluctuations, and the loss of coherence leads to a depletion of the zero-momentum, which we use as an interference reference.

5.4 | Spatially-resolved phase correlations

With the single-site resolution of the phase microscope, we are able to extract the phase correlation of the system with spatial resolution of a single lattice site. Below the BKT transition, we expect an algebraic decay of the first-order correlation function $g_1(d)$. We want to extract the exponent η of the decay. We therefore extract the phase correlation between the lattice sites and obtain the g_1-function[111] as

$$g_1(d) = \left\langle \psi^\dagger(\mathbf{r})\psi(\mathbf{r}+d) \right\rangle \propto \exp(-1/2 \left\langle (\Delta\theta)^2(d) \right\rangle), \tag{5.60}$$

where $\Delta\theta = \theta(\mathbf{r}) - \theta(\mathbf{r}+d)$ is the phase difference between lattice sites at a distance d. We restrain the evaluation of the g_1-function to a radius r_d around the center of the density distribution and average the tunneling element J over this area (Fig. 5.13). For each iteration, we identify the lattice sites, the centers of which are located inside the disc. We then compute the phase difference between all lattice sites in a single shot and take the average over all iterations with respect to the distance between lattice sites. The resulting correlations are plotted in figure 5.13 for a few exemplary lattice depths below the phase transition in a log-log plot and show the expected algebraic decay. We fit the algebraic model $g_1(d) \propto d^{-\eta}$ to the extracted correlations up to a distance of $d = 2.56\, a_\mathrm{lat}$ and obtain the exponents shown in figure 5.14. Here, we also extended the radius of the evaluation region, and remarkably, we find all data collapsing to one curve when scaling the data with the averaged tunneling element J, supporting the validity of the algebraic decay in inhomogeneous systems.

Beyond the phase transition, the stronger fluctuations are not properly mapped by the phase microscope, leading to a shallow $g_1(d)$ profile and small exponents under the invalid assumption of algebraic decay. In the superfluid regime, the exponents follow a linear scaling with temperature as predicted by Nelson and Kosterlitz[117]. Experimental evidence of this prediction has been shown recently in [101]. We fit this linear scaling including data points up to $k_\mathrm{B}T/J = 0.75$ and get a slope of $0.668(7)$, which yields a critical exponent at the phase transition of $\eta_c = 0.598(6)$. In addition to this statistical error, we estimate a systematic error of 10% due to the uncertainty in the calibration of atom number and lattice depth.

Our value and also the one found in [99, 100] differ from the expected critical value of the infinite homogeneous system $\eta_c = 0.25$. In [123], they performed a spin wave approximation of a harmonically confined Bose gas. They not only confirm the algebraic decay persists in the confined case but in addition find that the critical exponents are increased with decreasing system size. Especially, in the case of averaged g_1-functions, they find an increase of the critical exponent of a factor between 1.5

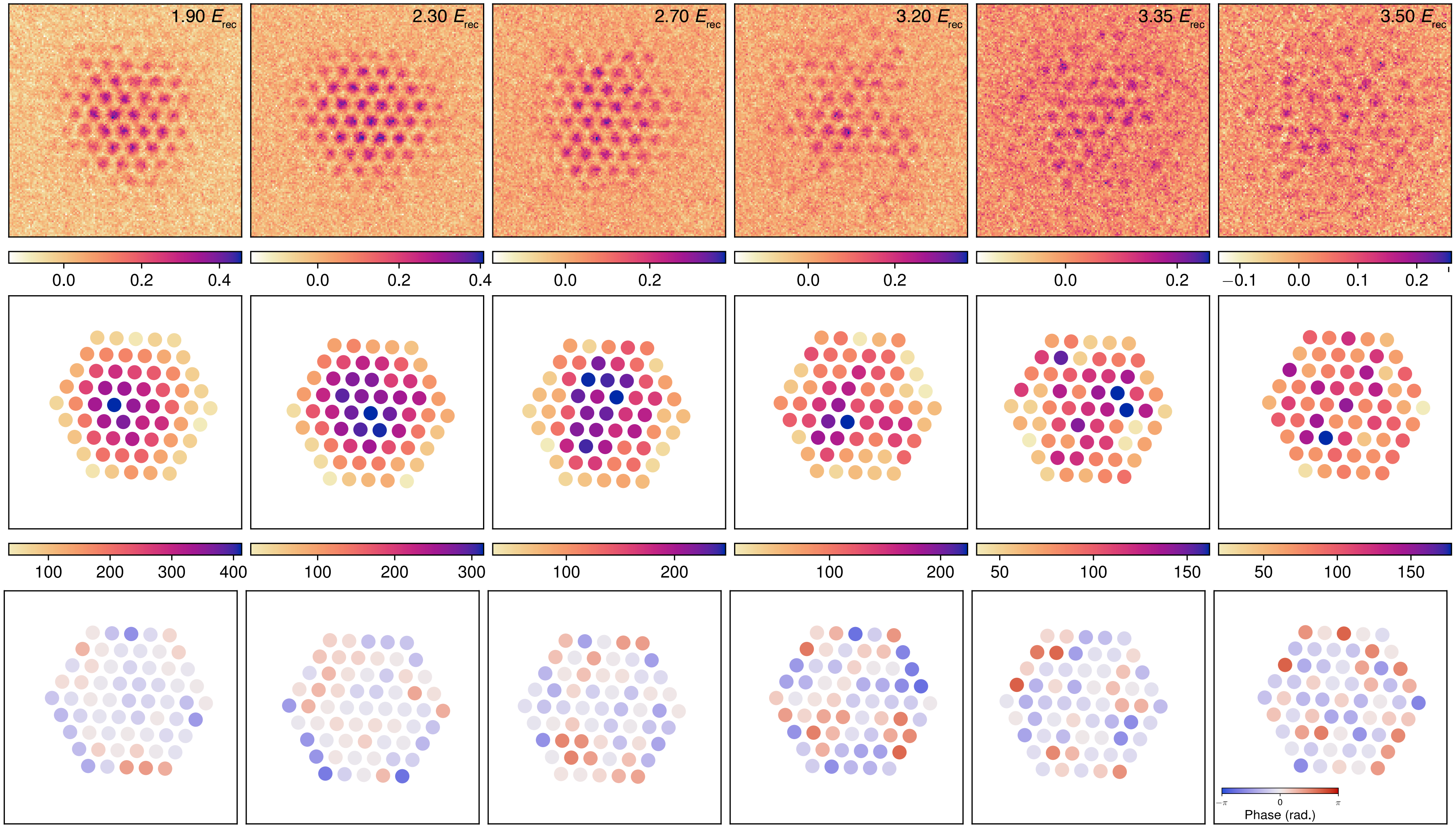

Figure 5.12: Phase microscope images. (Top) Measured optical density of phase microscope images for lattice depths $1.90, 2.30, 2.70, 3.20, 3.35$ and $3.50\,E_{\mathrm{rec}}$ displaying increasing fluctuations for deeper lattices. (Middle) Onsite populations obtained by integrating the density over the Wigner-Seitz cells. (Bottom) Individual phase profiles obtained by subtracting the mean envelopes and scaling by the conversion factor. The phase fluctuations increase with lattice depth towards the phase transition.

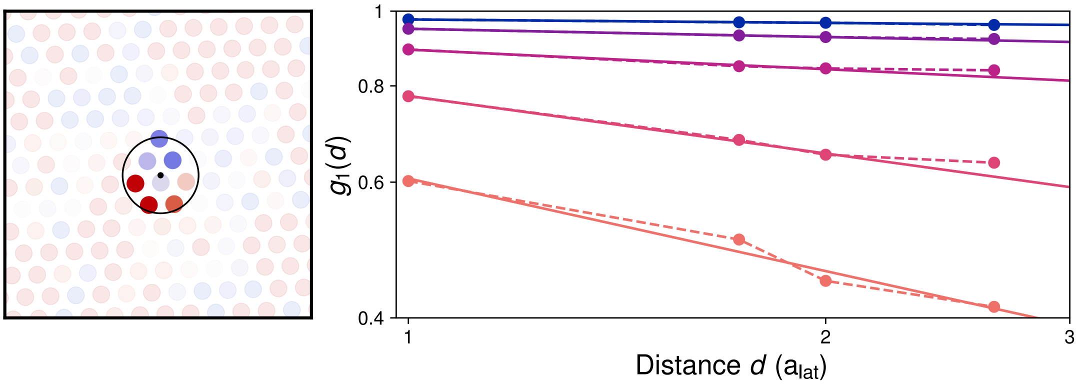

Figure 5.13: Extraction of g_1-correlation function. (Left) We extract the correlation of the extracted phases over a small area in center of the cloud to reduce averaging errors. Here the radius is $r = 1.5\,a_{\mathrm{lat}}$, i.e. distances with $d < 3$ are extracted. (Right) The phase coherence function $g_1(d)$ as a function of the distance d evaluated from the phase microscope shows an algebraic decay and we fit an exponent. The values are extracted for lattice values $V_0 = 1.7, 2.1, 2.5, 2.9$ and $3.3\,E_{\mathrm{rec}}$ (from top to bottom).

and 2, which matches the results in [99]. In [100], they explain the reduction in the critical exponent by their finite size system [138].

We find a similar behavior when increasing the radius R and evaluated distance d to the edge of the cloud as in [123] (Fig. 5.15). We do not change the system size, but as in figure 5.14, we increase the radius of evaluation. For small T/J, we find an algebraic decay up to about half the system size with only slightly increasing exponent and an increasing vertical offset. Our system has an $R/\lambda \approx 4$, where λ for our discrete spin model is the lattice spacing. In [123], they find a change in behavior only for the ratio of $R/\lambda \gtrsim 100$. We already find a plateau-like behavior when increasing the radius of evaluation to the edge of the cloud for significantly smaller systems (Fig. 5.15). The differences from the theory here may be explained by experimental fluctuations and initial density fluctuations at the edge of the system as well as the limits of the phase microscope at and above the phase transition. Probing the system with the phase microscope opens the possibility to compare the experiments to theory on a very detailed level in larger systems in the future.

Conclusion & Outlook

In this chapter, we introduced the phase microscope for quantum gases based on matter-wave microscopy, with which we are able to measure the phase on a single site level. We presented aberration-induced phase accumulation for this implementation of the phase microscope and compared it with numerical simulation. Experimentally, we presented the analysis to calibrate the conversion factor between the measured density deviations and the extracted phases. The calculated and calibrated conversion factor matches well, corroborating the analytic and calibration method. With the phase microscope, we probed the coherence properties and phase fluctuation across the BKT phase transition, utilizing the knowledge from the previous chapter. We extracted the correlation between

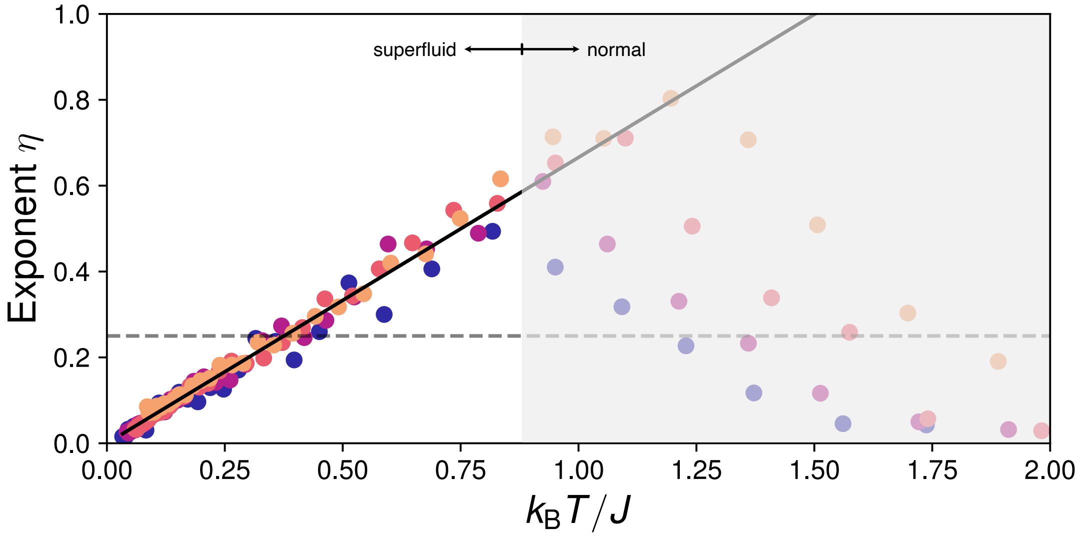

Figure 5.14: Algebraic exponents of the g_1-function. The exponents η evaluated on disks with increasing radius $(1.5, 2.5, 3.5$ and $4.5\,a_{\mathrm{lat}}$ (blue, purple, orange, yellow)) collapse onto a single line. The tunneling element J is the mean over the selected area. The data follows the expected linear increase with $k_{\mathrm{B}}T/J$ in the superfluid regime (non-shaded area) and we fit a slope using data up to $k_{\mathrm{B}}T/J = 0.75$ (black line), which yields $\eta_c = 0.598(6)$ at the phase transition to the normal phase (shaded area).

single lattice sites and were able to extract the algebraic decay below the phase transition. When extrapolating towards the critical value, we obtain $\eta_c = 0.598(6)$.

With the single-site resolution of the phase fluctuations, it is possible to extract the magnetization of the system as described in [93]. We take the Fourier transform on a hexagonal grid.[5] of our finite system with extended zero-padding. When averaging over all 100 configurations per lattice depth and extracting the zero-momentum component, we get a decreasing magnetization towards the phase transition as in figure 5.16. The behavior matches the spin-wave result for values below the phase transition [93, 127]. The onset of the predicted steep decrease towards the phase transition is, if at all, only barely visible. More data close to the phase transition would be needed. In addition, at and above the transition, this implementation of the phase microscope ceases to function, which explains the unexpected increase in magnetization and might deem the extraction of lower magnetization impossible. Other variations might be more effective in this region.

---

[5] The fast Fourier transform on a hexagonal grid is described in appendix A

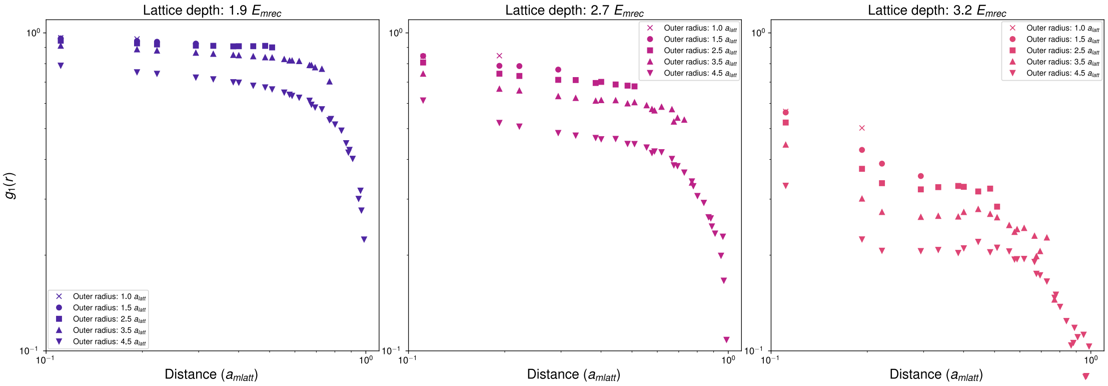

Figure 5.15: Averaging effects on the correlation function. Extraction of the correlation function for ever larger radii. When increasing the evaluation radius, we observe a decrease in the correlation length and an increase of the algebraic exponent at small distances. When reaching the edge of the cloud the correlation drops to zero. This behavior resembles the results in [123], but at much smaller R/λ.

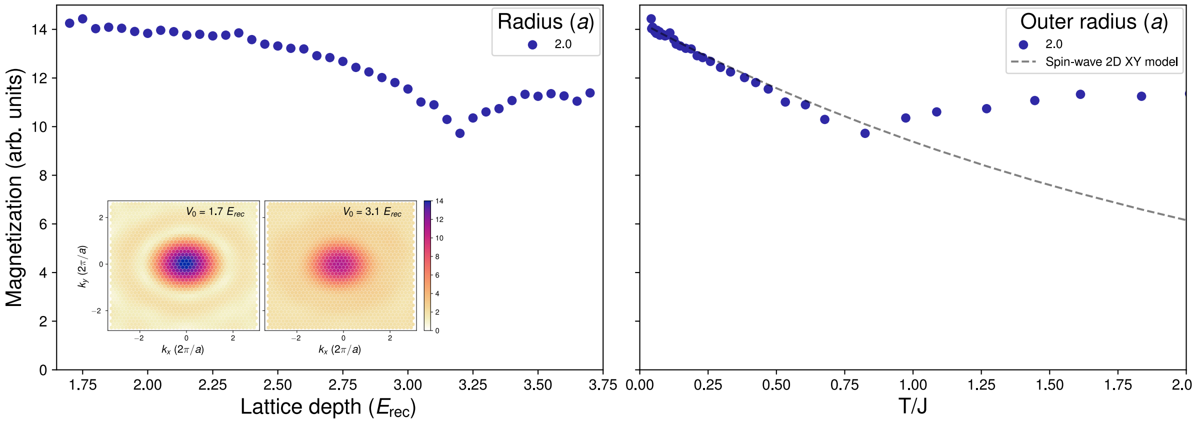

Figure 5.16: Magnetization extracted from hexagonal Fourier transform. (Left) The magnetization, the mean zero-momentum component, is plotted against the lattice depth. The insets show exemplary averaged Fourier transforms of the phase field. (Right) Here magnetization is plotted against the $k_{\rm B}T/J$, where the temperature T is the result from the phase thermometry and the tunneling element J is the mean multi-particle tunneling element of the radius $r = 2a_{\rm lat}$. The dashed line shows the spin-wave result as in [127], $M = (1/2N)^{1/8\pi K}$ with a manual adaption to data.

CHAPTER 6

Conclusion & Outlook

In this thesis, we presented the coherence magnifier utilizing the Talbot effect and the implementation of the phase microscope as new tools for quantum simulation with quantum gases.

In chapter 2, we provided an overview of the experimental setup used to achieve Bose-Einstein condensation with Lithium-7 atoms, focusing on laser cooling and evaporative cooling techniques. The setup features a compact design with an oven, a 2D-MOT, and 3D-MOT for initial laser cooling. We employ two evaporative stages, one in a magnetic trap and the other in an optical dipole trap, where we reach degeneracy. The lowest temperatures are below $50\,\mathrm{nK}$ with a condensate fraction around $90\,\%$ and up to 3×10^4 atoms.

In chapter 3, we described the development and functionality of a versatile optical trap setup that allowed multiple configurations, including the triangular lattice, the optical dipole trap, the multi-frequency lattice, and a moving lattice. The versatile lattice paves the way for advanced studies of lattice dynamics and coherence properties.

In chapter 4, we focused on using matter-wave microscopy to investigate coherence in quantum gases. By magnifying the atomic wavefunction, we captured density distributions at single-site resolution and explored the Talbot effect, which reveals coherence across lattice sites. This chapter demonstrated how the Talbot effect could be used as a tool to measure loss of coherence across the Berezinskii-Kosterlitz-Thouless (BKT) phase transition.

In the final chapter, we introduced the phase microscope that provided direct access to the local phase with a single-site resolution. We discussed the aberrations in the matter-wave lens, allowing us to extract the phases and confirmed the analytic methods with numerical simulations. We gave a short recap of the BKT phase transition and used the phase microscope to extract the local correlations. We obtained a critical exponent at the phase transition of $\eta_c = 0.598(5)$, discussed it in the context of trapped systems and compared it to other experimental results.

With a refined phase retrieval algorithm, which could possible be enhanced by machine learning[139], we envision a Talbot microscope measuring the phase on local sites, extending the capabilities of the presented phase microscope, possibly above $k_{\mathrm{B}}T/J = 1$. With the addition of the magnetization analysis, a close comparison with theory will then be possible. Furthermore, a detection method for vortex-anti-vortex pairs could be realized and the unbinding be measured in-situ.

On the experimental front, the introduction of rapid interaction switching at the beginning of the matter-wave protocol will facilitate studies of strongly interacting systems with minimal perturbation in the matter-wave protocol[140]. For further studies of strongly correlated systems, achieving single-atom sensitivity through spin-resolved, free-space fluorescence imaging[141–144] will be crucial. Reinstalling the high-resolution objective into the setup will enable this[45]. For this purpose, we developed a new method to shine the MOT beam through the objective. In Nora Bidzinski's master thesis, we developed a fiber-in-objective approach[145]. The fiber is polarization-maintaining. The end utilizes a 45° rotated piece of fiber to rotate the polarization from linear to circular at the output. The output facilitates a strong curvature, creating a focus behind the fiber and enlarging the numerical aperture, thus creating a large collimated beam in combination with the high-resolution objective.

A combination of high-resolution imaging and matter-wave microscopy as in [22] could expand the resolution limit. A full-fledged phase microscope would bring the characterization of quantum many-body systems to a new level. The possibilities may include distinguishing superfluid phases from Bose glass phases [146], probing of coherence locally in trimerized Mott insulators [147], identifying ergodic bubbles in many-body localized systems [148], or detecting chiral domains[149, 150].

With the matter-wave microscope, the emerging lattice structures from off-resonant laser beams, as we have seen in the moving lattices measurement, could be explored further[151]. The moving lattices could also be used to study the superfluidity of the condensate. Finalizing the implementation of the multi-frequency lattice will allow fast lattice ramps to excite the system into higher Bloch bands[70]. A particularly interesting direction would be the study of chiral superfluidity in these systems[79]; with a high-resolution objective, the matter-wave microscope could directly image the vortices and orbital structures of chiral phases with a sub-lattice constant resolution[21, 152].

APPENDIX A

Magnetization from hexagonal fast Fourier transform

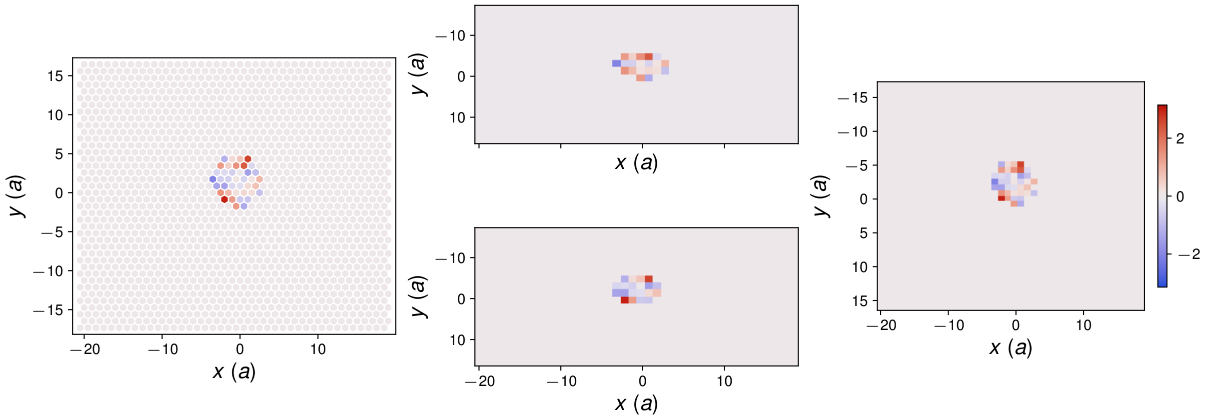

Figure A.1: Hexagonal representation in split array. Phase map from the phase microscope. The triangular lattice structure on the left is split into two, with the even rows in the upper panel ($a = 0$) and the odd rows in the lower panel ($a = 1$). These two arrays are used for the HFFT. The right shows a combined version of the two arrays on a square grid. The lattice depth is at $V_{\text{lat}} = 3.1\ E_{\text{rec}}$, i.e. close to the phase transition. The included radius of the cloud here is $r = 4a_{\text{lat}}$.

The magnetization in [93] is obtained from the lattice model by taking the Fourier transform of the wavefunction, i.e. the phase, because the density is assumed to be constant,

$$\tilde{\psi}_{\rightarrow k} = \frac{1}{N} \sum_{\rightarrow j} e^{-i \rightarrow k \rightarrow j} \tag{A.1}$$

and extracting the zero-momentum value at $\rightarrow k = 0$

$$M = \left\langle |\tilde{\psi}_0| \right\rangle . \tag{A.2}$$

They considered a quadratic lattice. The phase information in our lattice is on a triangular lattice, and the straightforward method of taking the computational fast Fourier transform on a 2D square grid is not possible. In [153], they adapted the fast Fourier transform (FFT) to a hexagonal grid, representing the position of the WS cells perfectly. The hexagonal fast Fourier transform (HFFT) algorithm they present is based on the hexagonal discrete Fourier transformation (HDFT) [154] and the array set addressing[155]. The hexagonal array is split into two separate arrays for odd and even rows. The coordinates are represented with three values instead of two, $(a, r, c) \in 0, 1 \times \mathcal{Z} \times \mathcal{Z}$. a is the array index, and r and c are the row and column indices of the two arrays. We transform the triangular lattice to the split array set, see figure A.1. We adapt the MATLAB code in [153] to Python and Fourier-transform the data (Fig A.2).

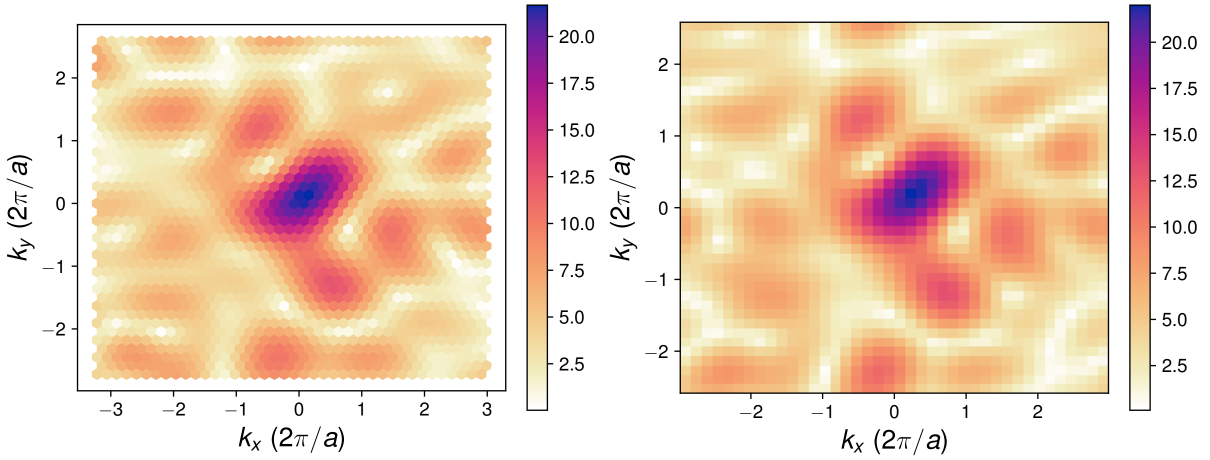

Figure A.2: Hexagonal fast Fourier transform. The left shows the HFFT performed on the split array and visualized on the triangular lattice again. On the right, we compare the HFFT with a standard FFT performed on the combined array in figure A.1. The close ensures the correct implementation of the algorithm, but the errors due to the wrong representation are expected. The lattice depth is at $V_0 = 3.1\ E_{\mathrm{rec}}$, i.e. close to the phase transition.

We obtain the magnetization in figure 5.16 by averaging over all 100 iterations per lattice depth and extracting the value at (0,0,0). We show a few exemplary HFFTs for different lattice depths and their averaged signals, see figure A.3.

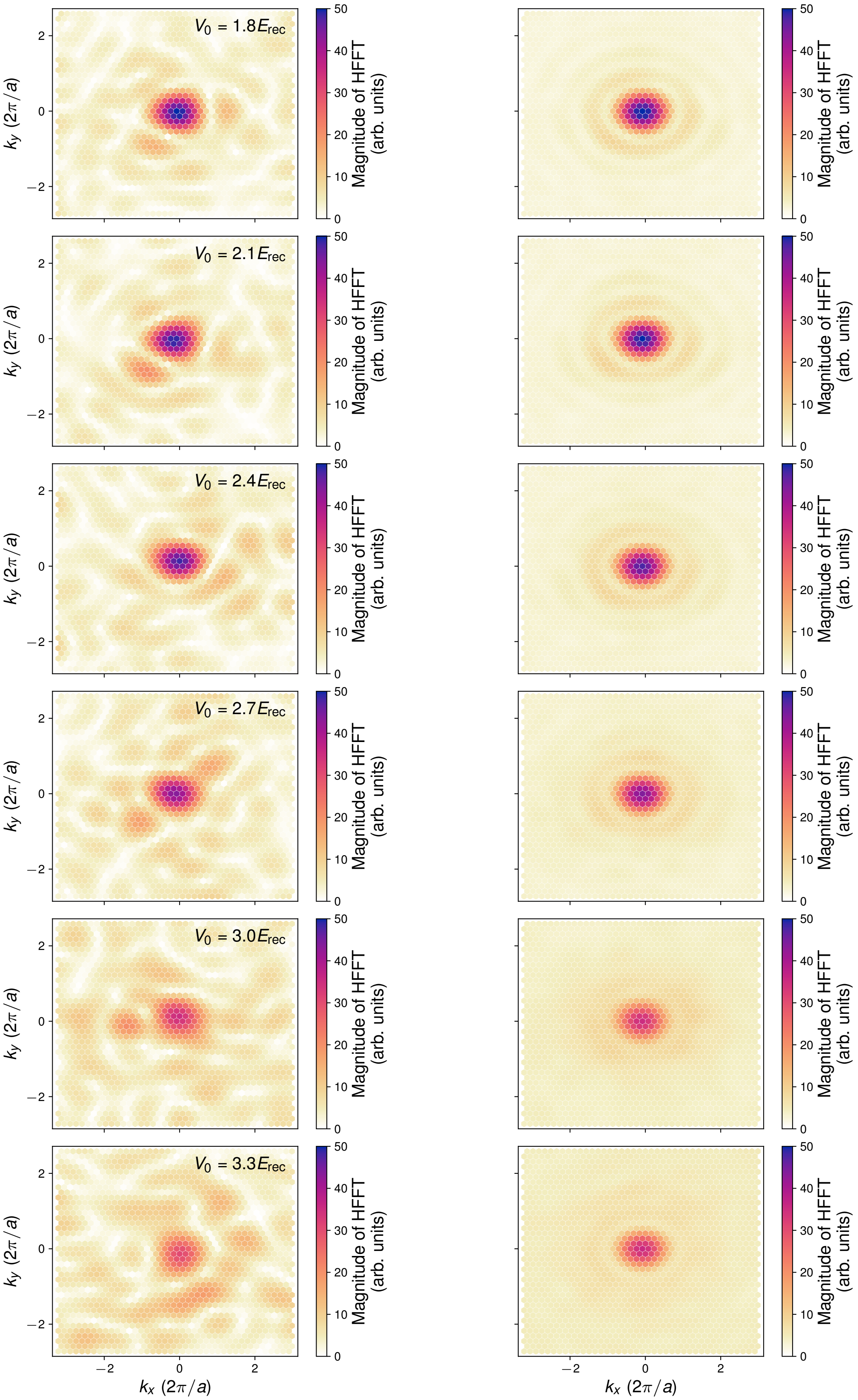

Figure A.3: HFFT for increasing lattice depth . (Left) Single shot HFFTs. (Right) Average of 100 iterations. HFFTs are performed on phase profiles with an inclusion radius of $r = 4$. We observe a decrease in the central peak intensity.

APPENDIX B

RIN spectra and EOM calibration

In figure B.1 the noise spectra for the beams L2 and L3 are shown. In figure B.2 we show the EOM calibration measurements.

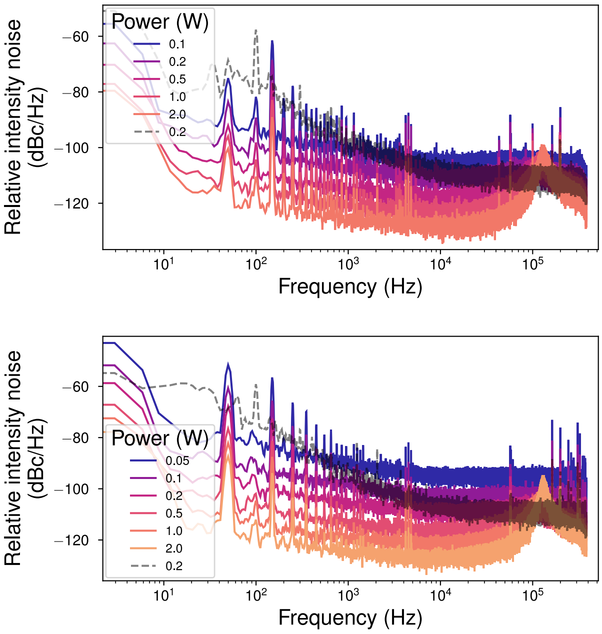

Figure B.1: RIN spectra of L2 and L3. (Top) RIN spectrum of L2. (Bottom) RIN spectrum of L3.

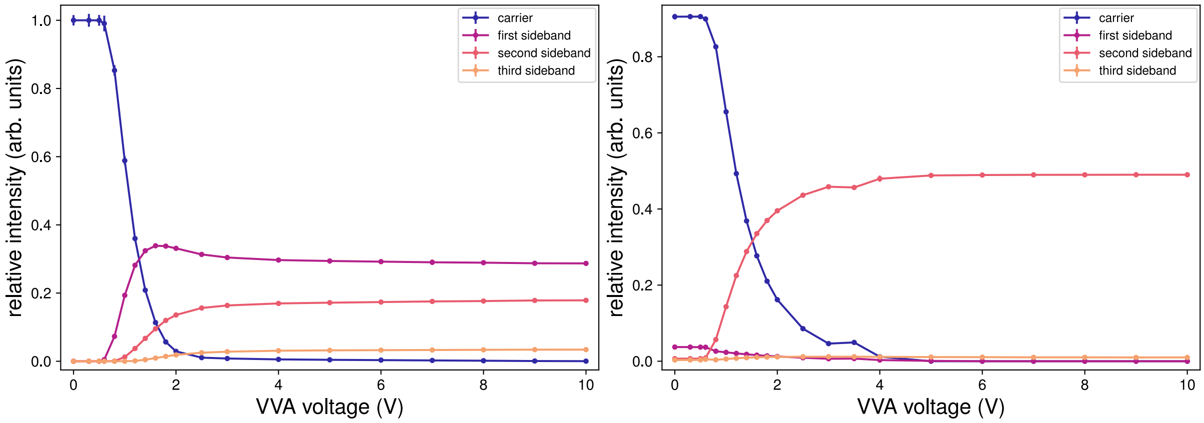

Figure B.2: EOM calibration for L2 and L3. The relative intensities carrier and the sidebands created by the EOMs. (Left: L2, right: L3)

Bibliography

[1] R. P. Feynman. “Simulating physics with computers”. In: *Int. J. Theor. Phys.* 21.6/7 (1982), pp. 467–488 (cit. on p. 1).

[2] I. Bloch, J. Dalibard, and S. Nascimbène. “Quantum simulations with ultracold quantum gases”. English. In: *Nature Physics* 8.4 (Apr. 2012), pp. 267–276. DOI: `10.1038/nphys2259` (cit. on p. 1).

[3] K. B. Davis, M. O. Mewes, M. R. Andrews, N. J. v. Druten, D. S. Durfee, D. M. Kurn, and W. Ketterle. “Bose-Einstein condensation in a gas of sodium atoms”. English. In: *Physical Review Letters* 75.22 (1995), pp. 3969–3973. DOI: `10.1103/physrevlett.75.3969` (cit. on pp. 1, 13).

[4] W. S. Bakr, J. I. Gillen, A. Peng, S. Fölling, and M. Greiner. “A quantum gas microscope for detecting single atoms in a Hubbard-regime optical lattice”. In: *Nature* 462.7269 (Nov. 2009), pp. 74–77. DOI: `10.1038/nature08482` (cit. on pp. 1, 8).

[5] J. F. Sherson, C. Weitenberg, M. Endres, M. Cheneau, I. Bloch, and S. Kuhr. “Single-atom-resolved fluorescence imaging of an atomic Mott insulator”. In: *Nature* 467.7311 (2010), pp. 68–72. ISSN: 1476-4687. DOI: `10.1038/nature09378` (cit. on pp. 1, 8).

[6] G. J. A. Edge, R. Anderson, D. Jervis, D. C. McKay, R. Day, S. Trotzky, and J. H. Thywissen. “Imaging and addressing of individual fermionic atoms in an optical lattice”. English. In: *Phys. Rev. A* 92.6 (Dec. 2015), pp. 063406–6. DOI: `10.1103/physreva.92.063406` (cit. on p. 1).

[7] A. Omran, M. Boll, T. A. Hilker, K. Kleinlein, G. Salomon, I. Bloch, and C. Gross. “Microscopic Observation of Pauli Blocking in Degenerate Fermionic Lattice Gases”. English. In: *Physical Review Letters* 115.26 (Dec. 2015), pp. 263001–5. DOI: `10.1103/physrevlett.115.263001` (cit. on p. 1).

[8] M. F. Parsons, F. Huber, A. Mazurenko, C. S. Chiu, W. Setiawan, K. Wooley-Brown, S. Blatt, and M. Greiner. “Site-Resolved Imaging of Fermionic Li6 in an Optical Lattice”. English. In: *Physical Review Letters* 114.21 (May 2015), pp. 213002–5. DOI: `10.1103/physrevlett.114.213002` (cit. on p. 1).

[9] E. Haller, J. Hudson, A. Kelly, D. A. Cotta, B. Peaudecerf, G. D. Bruce, and S. Kuhr. “Single-atom imaging of fermions in a quantum-gas microscope”. In: *Nature Physics* 11.9 (July 2015), pp. 738–742. DOI: `10.1038/nphys3403` (cit. on p. 1).

[10] L. W. Cheuk, M. A. Nichols, M. Okan, T. Gersdorf, V. V. Ramasesh, W. S. Bakr, T. Lompe, and M. W. Zwierlein. "Quantum-Gas Microscope for Fermionic Atoms". English. In: *Physical Review Letters* 114.19 (May 2015), p. 193001. DOI: `10.1103/physrevlett.114.193001` (cit. on p. 1).

[11] P. T. Brown, D. Mitra, E. Guardado-Sanchez, P. Schauß, S. S. Kondov, E. Khatami, T. Paiva, N. Trivedi, D. A. Huse, and W. S. Bakr. "Spin-imbalance in a 2D Fermi-Hubbard system". In: *Science* 357.6358 (2017), pp. 1385–1388. ISSN: 0036-8075. DOI: `10.1126/science.aam7838`. eprint: `1612.07746` (cit. on p. 1).

[12] C. Weitenberg, P. Schauß, T. Fukuhara, M. Cheneau, M. Endres, I. Bloch, and S. Kuhr. "Coherent Light Scattering from a Two-Dimensional Mott Insulator". In: *Phys. Rev. Lett.* 106 (2011), p. 215301. DOI: `10.1103/physrevlett.106.215301` (cit. on pp. 1, 47).

[13] W. S. Bakr, A. Peng, M. E. Tai, R. Ma, J. Simon, J. I. Gillen, S. Fölling, L. Pollet, and M. Greiner. "Probing the superfluid-to-Mott insulator transition at the single-atom level". In: *Science* 329.5991 (2010), pp. 547–550. ISSN: 00368075. DOI: `10.1126/science.1192368` (cit. on p. 1).

[14] A. Mazurenko, C. S. Chiu, G. Ji, M. F. Parsons, M. Kanász-Nagy, R. Schmidt, F. Grusdt, E. Demler, D. Greif, and M. Greiner. "A cold-atom Fermi–Hubbard antiferromagnet". In: *Nature* 545.7655 (Dec. 2017), pp. 462–466. ISSN: 0028-0836. DOI: `10.1038/nature22362`. eprint: `1612.08436` (cit. on p. 1).

[15] G. Salomon, J. Koepsell, J. Vijayan, T. A. Hilker, J. Nespolo, L. Pollet, I. Bloch, and C. Gross. "Direct observation of incommensurate magnetism in Hubbard chains". English. In: *Nature* 565.7737 (Jan. 2019), pp. 56–60. DOI: `10.1038/s41586-018-0778-7` (cit. on p. 1).

[16] J. Koepsell, J. Vijayan, P. Sompet, F. Grusdt, T. A. Hilker, E. Demler, G. Salomon, I. Bloch, and C. Gross. "Imaging magnetic polarons in the doped Fermi–Hubbard model". English. In: *Nature* 572.7769 (Aug. 2019), pp. 358–362. DOI: `10.1038/s41586-019-1463-1` (cit. on p. 1).

[17] J. Vijayan, P. Sompet, G. Salomon, J. Koepsell, S. Hirthe, A. Bohrdt, F. Grusdt, I. Bloch, and C. Gross. "Time-resolved observation of spin-charge deconfinement in fermionic Hubbard chains". In: *Science* 367.6474 (2020), pp. 186–189. ISSN: 0036-8075. DOI: `10.1126/science.aay2354`. eprint: `1905.13638` (cit. on p. 1).

[18] C. S. Chiu, G. Ji, A. Bohrdt, M. Xu, M. Knap, E. Demler, F. Grusdt, M. Greiner, and D. Greif. "String patterns in the doped Hubbard model". English. In: *Science* 365.6450 (2019), pp. 251–+. DOI: `10.1126/science.aav3587` (cit. on p. 1).

[19] G. Ji, M. Xu, L. H. Kendrick, C. S. Chiu, J. C. Brüggenjürgen, D. Greif, A. Bohrdt, F. Grusdt, E. Demler, M. Lebrat, and M. Greiner. "Coupling a Mobile Hole to an Antiferromagnetic Spin Background: Transient Dynamics of a Magnetic Polaron". In: *Physical Review X* 11.2 (2021), p. 021022. DOI: `10.1103/physrevx.11.021022`. eprint: `2006.06672` (cit. on p. 1).

[20] A. Impertro, S. Karch, J. F. Wienand, S. Huh, C. Schweizer, I. Bloch, and M. Aidelsburger. "Local Readout and Control of Current and Kinetic Energy Operators in Optical Lattices". In: *Phys. Rev. Lett.* 133 (2024), p. 063401. DOI: `10.1103/physrevlett.133.063401` (cit. on p. 1).

[21] L. Asteria, H. P. Zahn, M. N. Kosch, K. Sengstock, and C. Weitenberg. "Quantum gas magnifier for sub-lattice-resolved imaging of 3D quantum systems". In: *Nature* 599.7886 (2021), pp. 571–575. ISSN: 14764687. DOI: `10.1038/s41586-021-04011-2`. eprint: `2104.10089` (cit. on pp. 2, 5, 30, 35, 36, 38, 54, 73, 84).

[22] S. Brandstetter, C. Heintze, K. Subramanian, P. Hill, P. M. Preiss, M. Gałka, and S. Jochim. "Magnifying the Wave Function of Interacting Fermionic Atoms". In: *arXiv* (2024). DOI: `10.48550/arxiv.2409.18954`. eprint: `2409.18954` (cit. on pp. 2, 35, 39, 84).

[23] J. C. Brüggenjürgen, M. S. Fischer, and C. Weitenberg. "A phase microscope for quantum gases". In: *arXiv* (2024). eprint: `2410.10611` (cit. on pp. 2, 3, 5, 35, 57).

[24] M. R. Andrews, C. G. Townsend, H.-J. Miesner, D. S. Durfee, D. M. Kurn, and W. Ketterle. "Observation of Interference Between Two Bose Condensates". In: *Science* 275.5300 (1997), pp. 637–641. DOI: `10.1126/science.275.5300.637` (cit. on pp. 2, 35).

[25] I. Bloch. "Ultracold quantum gases in optical lattices". English. In: *Nature Physics* 1.1 (Oct. 2005), pp. 23–30. DOI: `10.1038/nphys138` (cit. on p. 2).

[26] H. Talbot. "LXXVI. Facts relating to optical science. No. IV". In: *The London, Edinburgh, and Dublin Philosophical Magazine and Journal of Science* 9.56 (1836), pp. 401–407. ISSN: 1941-5966. DOI: `10.1080/14786443608649032` (cit. on pp. 2, 35, 41).

[27] J. F. Clauser and S. Li. "Talbot-vonLau atom interferometry with cold slow potassium". In: *Phys. Rev. A* 49.4 (1994), R2213–R2216. ISSN: 1050-2947. DOI: `10.1103/physreva.49.r2213` (cit. on pp. 2, 41).

[28] M. S. Chapman, C. R. Ekstrom, T. D. Hammond, J. Schmiedmayer, B. E. Tannian, S. Wehinger, and D. E. Pritchard. "Near-field imaging of atom diffraction gratings: The atomic Talbot effect". In: *Phys. Rev. A* 51.1 (1995), R14–R17. ISSN: 1050-2947. DOI: `10.1103/physreva.51.r14` (cit. on pp. 2, 41).

[29] B. J. McMorran and A. D. Cronin. "An electron Talbot interferometer". In: *New Journal of Physics* 11.3 (2009), p. 033021. DOI: `10.1088/1367-2630/11/3/033021`. eprint: `0812.4566` (cit. on pp. 2, 41).

[30] S. Gerlich, S. Eibenberger, M. Tomandl, S. Nimmrichter, K. Hornberger, P. J. Fagan, J. Tüxen, M. Mayor, and M. Arndt. "Quantum interference of large organic molecules". In: *Nature Communications* 2.1 (2011), p. 263. ISSN: 20411723. DOI: `10.1038/ncomms1263` (cit. on pp. 2, 41).

[31] T. Gao, E. Estrecho, G. Li, O. A. Egorov, X. Ma, K. Winkler, M. Kamp, C. Schneider, S. Höfling, A. G. Truscott, and E. A. Ostrovskaya. "Talbot Effect for Exciton Polaritons". In: *Physical Review Letters* 117.9 (2016), p. 097403. ISSN: 0031-9007. DOI: `10.1103/physrevlett.117.097403`. eprint: `1603.05056` (cit. on pp. 2, 41).

[32] Z. Hadzibabic, P. Krüger, M. Cheneau, B. Battelier, and J. Dalibard. "Berezinskii-Kosterlitz-Thouless crossover in a trapped atomic gas". In: *Nature* 441.7097 (2006), pp. 1118–1121. ISSN: 14764687. DOI: `10.1038/nature04851`. eprint: `cond-mat/0605291` (cit. on pp. 2, 35, 49, 62).

[33] V. L. Berezinskii. "Destruction Of Long-Range Order In One-Dimensional And Two-Dimensionalsystems Possessing A Continuous Symmetry Group. Ii. Quantum Systems". In: *Soviet Physics JETP* (1972) (cit. on pp. 2, 35, 57).

[34] J. M. Kosterlitz and D. J. Thouless. "Ordering, metastability and phase transitions in two-dimensional systems". In: *Journal of Physics C: Solid State Physics* 6.7 (1973), p. 1181. ISSN: 0022-3719. DOI: `10.1088/0022-3719/6/7/010` (cit. on pp. 2, 35, 57).

[35] A. Bohrdt, L. Homeier, C. Reinmoser, E. Demler, and F. Grusdt. "Exploration of doped quantum magnets with ultracold atoms". In: *Annals of Physics* 435 (2021), p. 168651. ISSN: 0003-4916. DOI: `10.1016/j.aop.2021.168651`. eprint: `2107.08043` (cit. on p. 2).

[36] M. Fischer. "A Matter-Wave Microscope for Lithium Atomsin a Tunable Optical Lattice". In: (2023). PhD - Weitenberg/Sengstock Group (cit. on pp. 5, 7–11, 13, 19, 20, 35, 36).

[37] C. C. Bradley, C. A. Sackett, J. J. Tollett, and R. G. Hulet. "Evidence of Bose-Einstein Condensation in an Atomic Gas with Attractive Interactions". English. In: *Physical Review Letters* 75.9 (Aug. 1995), pp. 1687–1690. DOI: `10.1103/physrevlett.75.1687` (cit. on p. 5).

[38] A. G. Truscott, K. E. Strecker, W. I. McAlexander, G. B. Partridge, and R. G. Hulet. "Observation of Fermi pressure in a gas of trapped atoms". In: *Science* 291.5513 (2001), pp. 2570–2572. ISSN: 0036-8075. DOI: `10.1126/science.1059318` (cit. on p. 5).

[39] S. E. Pollack, D. Dries, and R. G. Hulet. "Universality in Three- and Four-Body Bound States of Ultracold Atoms". In: *Science* 326.5960 (2009), pp. 1683–1685. ISSN: 0036-8075. DOI: `10.1126/science.1182840`. eprint: `0911.0893` (cit. on pp. 5, 6).

[40] R. G. Hulet, J. H. V. Nguyen, and R. Senaratne. "Methods for preparing quantum gases of lithium". In: *Review of Scientific Instruments* 91.1 (2020), p. 011101. ISSN: 0034-6748. DOI: `10.1063/1.5131023`. eprint: `1910.07041` (cit. on pp. 5, 6, 53).

[41] E. R. I. Abraham, W. I. McAlexander, J. M. Gerton, R. G. Hulet, R. Côté, and A. Dalgarno. "Triplet s-wave resonance in Li6 collisions and scattering lengths of Li6 and Li7". In: *Physical Review A* 55.5 (1997), R3299–R3302. ISSN: 1050-2947. DOI: `10.1103/physreva.55.r3299` (cit. on p. 5).

[42] J. M. Gerton, C. A. Sackett, B. J. Frew, and R. G. Hulet. "Dipolar relaxation collisions in magnetically trapped 7Li". In: *Physical Review A* 59.2 (1999), pp. 1514–1516. ISSN: 1050-2947. DOI: `10.1103/physreva.59.1514` (cit. on p. 6).

[43] E. A. Burt, R. W. Ghrist, C. J. Myatt, M. J. Holland, E. A. Cornell, and C. E. Wieman. "Coherence, Correlations, and Collisions: What One Learns about Bose-Einstein Condensates from Their Decay". In: *Physical Review Letters* 79.3 (1997), pp. 337–340. ISSN: 0031-9007. DOI: `10.1103/physrevlett.79.337` (cit. on p. 6).

[44] D. M. Stamper-Kurn, M. R. Andrews, A. P. Chikkatur, S. Inouye, H.-J. Miesner, J. Stenger, and W. Ketterle. “Optical Confinement of a Bose-Einstein Condensate”. In: *Physical Review Letters* 80.10 (1998), pp. 2027–2030. ISSN: 0031-9007. DOI: `10.1103/physrevlett.80.2027`. eprint: `cond-mat/9711273` (cit. on p. 6).

[45] A. Kerkmann. “A novel Apparatus for Quantum Gas Microscopy of Lithium Atoms”. PhD - Sengstock Group. PhD thesis. 2019 (cit. on pp. 7, 9, 11, 84).

[46] M. Hagemann. “A setup for high-resolution imaging of ultracold Lithium atoms”. In: (2020). PhD - Sengstock Group (cit. on pp. 7, 9, 11, 14).

[47] A. Kerkmann. “Ein Lasersystem zum Fangen und Kühlen von bosonischem und fermionischem Lithium”. Master - Sengstock Group. Master’s Thesis. 2016 (cit. on p. 8).

[48] T. G. Tiecke, S. D. Gensemer, A. Ludewig, and J. T. M. Walraven. “High-flux two-dimensional magneto-optical-trap source for cold lithium atoms”. In: *Physical Review A* 80.1 (2009), p. 013409. ISSN: 1050-2947. DOI: `10.1103/physreva.80.013409` (cit. on p. 10).

[49] K. Li, D. Zhang, T. Gao, S.-G. Peng, and K. Jiang. “Enhanced trapping of cold Li6 using multiple-sideband cooling in a two-dimensional magneto-optical trap”. In: *Physical Review A* 92.1 (2015), p. 013419. ISSN: 1050-2947. DOI: `10.1103/physreva.92.013419` (cit. on p. 11).

[50] J. H. Lee and J. Mun. “Optimized atomic flux from a frequency-modulated two-dimensional magneto-optical trap for cold fermionic potassium atoms”. In: *Journal of the Optical Society of America B* 34.7 (2017), p. 1415. ISSN: 0740-3224. DOI: `10.1364/josab.34.001415` (cit. on p. 11).

[51] D. R. Fernandes, F. Sievers, N. Kretzschmar, S. Wu, C. Salomon, and F. Chevy. “Sub-Doppler laser cooling of fermionic 40K atoms in three-dimensional gray optical molasses”. In: *Europhysics Letters* 100.6 (2012), p. 63001. ISSN: 0295-5075. DOI: `10.1209/0295-5075/100/63001`. eprint: `1210.1310` (cit. on p. 12).

[52] A. T. Grier, I. Ferrier-Barbut, B. S. Rem, M. Delehaye, L. Khaykovich, F. Chevy, and C. Salomon. “Λ-enhanced sub-Doppler cooling of lithium atoms in D1 gray molasses”. In: *Physical Review A* 87.6 (2013), p. 063411. ISSN: 1050-2947. DOI: `10.1103/physreva.87.063411`. eprint: `1304.6971` (cit. on p. 12).

[53] F. Sievers, N. Kretzschmar, D. R. Fernandes, D. Suchet, M. Rabinovic, S. Wu, C. V. Parker, L. Khaykovich, C. Salomon, and F. Chevy. “Simultaneous sub-Doppler laser cooling of fermionic Li6and K40on the D1line: Theory and experiment”. English. In: *Phys. Rev. A* 91.2 (Feb. 2015), pp. 023426–11. DOI: `10.1103/physreva.91.023426` (cit. on p. 12).

[54] N. Gross and L. Khaykovich. “All-optical production of L7i Bose-Einstein condensation using Feshbach resonances”. In: *Physical Review A* 77.2 (2008), p. 023604. ISSN: 1050-2947. DOI: `10.1103/physreva.77.023604`. eprint: `0712.0717` (cit. on p. 12).

[55] I. Dimitrova, W. Lunden, J. Amato-Grill, N. Jepsen, Y. Yu, M. Messer, T. Rigaldo, G. Puentes, D. Weld, and W. Ketterle. "Observation of two-beam collective scattering phenomena in a Bose-Einstein condensate". In: *Physical Review A* 96.5 (2017). Inititial publication Li-Exp Ketterle group, p. 051603. ISSN: 2469-9926. DOI: `10.1103/physreva.96.051603`. eprint: `1709.02028` (cit. on pp. 12, 13).

[56] Z. A. Geiger, K. M. Fujiwara, K. Singh, R. Senaratne, S. V. Rajagopal, M. Lipatov, T. Shimasaki, R. Driben, V. V. Konotop, T. Meier, and D. M. Weld. "Observation and Uses of Position-Space Bloch Oscillations in an Ultracold Gas". In: *Physical Review Letters* 120.21 (2018), p. 213201. ISSN: 0031-9007. DOI: `10.1103/physrevlett.120.213201`. eprint: `1803.02456` (cit. on pp. 12, 13).

[57] K. Kim, S. Huh, K. Kwon, and J.-y. Choi. "Rapid production of large Li7 Bose-Einstein condensates using D1 gray molasses". In: *Physical Review A* 99.5 (2019). ISSN: 2469-9926. DOI: `10.1103/physreva.99.053604` (cit. on pp. 12, 13).

[58] A. Beckmann, K. D. Böklen, and D. Elke. "Precision measurements of the nuclear magnetic dipole moments of6Li,7Li,23Na,39K and41K". In: *Zeitschrift für Physik* 270.3 (1974), pp. 173–186. ISSN: 0044-3328. DOI: `10.1007/bf01680407` (cit. on p. 12).

[59] E. Arimondo, M. Inguscio, and P. Violino. "Experimental determinations of the hyperfine structure in the alkali atoms". In: *Reviews of Modern Physics* 49.1 (1977), pp. 31–75. ISSN: 0034-6861. DOI: `10.1103/revmodphys.49.31` (cit. on p. 12).

[60] S. P. Ram, S. R. Mishra, S. K. Tiwari, and H. S. Rawat. "Temperature and phase-space density of a cold atom cloud in a quadrupole magnetic trap". In: *Journal of the Korean Physical Society* 65.4 (2014), pp. 462–470. ISSN: 0374-4884. DOI: `10.3938/jkps.65.462`. eprint: `1401.7165` (cit. on p. 13).

[61] E. Majorana. "Atomi orientati in campo magnetico variabile". In: *Il Nuovo Cimento (1924-1942)* 9.2 (1932), pp. 43–50. ISSN: 0029-6341. DOI: `10.1007/bf02960953` (cit. on p. 13).

[62] W. Ketterle, D. S. Durfee, and D. M. Stamper-Kurn. "Making, probing and understanding Bose-Einstein condensates". In: (1999). eprint: `cond-mat/9904034` (cit. on pp. 13, 15, 57, 64).

[63] W. Petrich, M. H. Anderson, J. R. Ensher, and E. A. Cornell. "Stable, Tightly Confining Magnetic Trap for Evaporative Cooling of Neutral Atoms". In: *Physical Review Letters* 74.17 (1995), pp. 3352–3355. ISSN: 0031-9007. DOI: `10.1103/physrevlett.74.3352` (cit. on p. 13).

[64] C. C. Bradley, C. A. Sackett, and R. G. Hulet. "Bose-Einstein Condensation of Lithium: Observation of Limited Condensate Number". In: *Physical Review Letters* 78.6 (1997), pp. 985–989. ISSN: 0031-9007. DOI: `10.1103/physrevlett.78.985` (cit. on p. 14).

[65] R. U. H. v. Wurmb. "About a symmetry problem of Helmholtz coils and their corresponding magnetic fields". Bachelor's Thesis. 2023 (cit. on p. 14).

[66] W. Ketterle and N. J. v. Druten. "Bose-Einstein condensation of a finite number of particles trapped in one or three dimensions". In: *Physical Review A* 54.1 (1996), pp. 656–660. ISSN: 1050-2947. DOI: `10.1103/physreva.54.656` (cit. on p. 17).

[67] M. A. Kristensen, M. B. Christensen, M. Gajdacz, M. Iglicki, K. Pawłowski, C. Klempt, J. F. Sherson, K. Rzążewski, A. J. Hilliard, and J. J. Arlt. "Observation of Atom Number Fluctuations in a Bose-Einstein Condensate". In: *Physical Review Letters* 122.16 (2019), p. 163601. ISSN: 0031-9007. DOI: `10.1103/physrevlett.122.163601`. eprint: `1812.03064` (cit. on p. 17).

[68] M. B. Christensen, T. Vibel, A. J. Hilliard, M. B. Kruk, K. Pawłowski, D. Hryniuk, K. Rzążewski, M. A. Kristensen, and J. J. Arlt. "Observation of Microcanonical Atom Number Fluctuations in a Bose-Einstein Condensate". In: *Physical Review Letters* 126.15 (2021), p. 153601. ISSN: 0031-9007. DOI: `10.1103/physrevlett.126.153601`. eprint: `2011.08736` (cit. on p. 17).

[69] J. Bracker. "Studying multifrequency quasicrystal and 3D optical lattices for quantum simulation". Master's Thesis. 2024 (cit. on p. 18).

[70] M. N. Kosch, L. Asteria, H. P. Zahn, K. Sengstock, and C. Weitenberg. "Multifrequency optical lattice for dynamic lattice-geometry control". In: *Phys. Rev. Res.* 4.4 (2022), p. 043083. DOI: `10.1103/physrevresearch.4.043083`. eprint: `2207.03811` (cit. on pp. 19, 29, 84).

[71] R. Grimm, M. Weidemüller, and Y. B. Ovchinnikov. "Optical dipole traps for neutral atoms". In: *Advances In Atomic, Molecular, and Optical Physics* 42 (2000), pp. 95–170. ISSN: 1049-250X. DOI: `10.1016/s1049-250x(08)60186-x` (cit. on p. 22).

[72] E. Hecht. *Optik*. Walter de Gruyter. Wien-München: Oldenbourg, 2005. ISBN: 9783110347968 (cit. on p. 22).

[73] N. Fläschner. "Ultracold Fermions in Tunable HexagonalLattices: From High-PrecisionSpectroscopy to the Measurement ofBerry Curvature". PhD - Sengstock group. PhD thesis. 2016 (cit. on pp. 25, 33).

[74] P. L. Kapitza and P. A. M. Dirac. "The reflection of electrons from standing light waves". In: *Mathematical Proceedings of the Cambridge Philosophical Society* 29.2 (1933), pp. 297–300. ISSN: 0305-0041. DOI: `10.1017/s0305004100011105` (cit. on p. 27).

[75] Y. B. Ovchinnikov, J. H. Müller, M. R. Doery, E. J. D. Vredenbregt, K. Helmerson, S. L. Rolston, and W. D. Phillips. "Diffraction of a Released Bose-Einstein Condensate by a Pulsed Standing Light Wave". In: *Physical Review Letters* 83.2 (1999), pp. 284–287. ISSN: 0031-9007. DOI: `10.1103/physrevlett.83.284` (cit. on p. 27).

[76] J. H. Denschlag, J. E. Simsarian, H. Häffner, C. McKenzie, A. Browaeys, D. Cho, K. Helmerson, S. L. Rolston, and W. D. Phillips. "A Bose-Einstein condensate in an optical lattice". In: *Journal of Physics B: Atomic, Molecular and Optical Physics* 35.14 (2002), p. 3095. ISSN: 0953-4075. DOI: `10.1088/0953-4075/35/14/307`. eprint: `cond-mat/0206063` (cit. on p. 28).

[77] H. Zahn. “Observation of spontaneous density-wave patterns using a quantum gas magnifier”. PhD - Sengstock Group. PhD thesis. 2022 (cit. on pp. 30, 31).

[78] F. Bloch. “Über die Quantenmechanik der Elektronen in Kristallgittern”. In: *Zeitschrift für Physik* 52.7-8 (1929), pp. 555–600. ISSN: 0044-3328. DOI: `10.1007/bf01339455` (cit. on p. 32).

[79] X. Q. Wang, G. Q. Luo, J. Y. Liu, W. V. Liu, A. Hemmerich, and Z. F. Xu. “Evidence for an atomic chiral superfluid with topological excitations”. In: *Nature* 596.7871 (2021), pp. 227–231. ISSN: 14764687. DOI: `10.1038/s41586-021-03702-0` (cit. on pp. 33, 84).

[80] B. Santra, C. Baals, R. Labouvie, A. B. Bhattacherjee, A. Pelster, and H. Ott. “Measuring finite-range phase coherence in an optical lattice using Talbot interferometry”. In: *Nature Communications* 8.1 (2017), pp. 1–8. ISSN: 20411723. DOI: `10.1038/ncomms15601`. eprint: `1611.08430` (cit. on pp. 35, 41–43, 51, 54, 57).

[81] P. A. Murthy, D. Kedar, T. Lompe, M. Neidig, M. G. Ries, A. N. Wenz, G. Zürn, and S. Jochim. “Matter-wave Fourier optics with a strongly interacting two-dimensional Fermi gas”. In: *Physical Review A* 90.4 (2014), p. 043611. ISSN: 1050-2947. DOI: `10.1103/physreva.90.043611`. eprint: `1408.4680` (cit. on p. 36).

[82] K. Hueck, N. Luick, L. Sobirey, J. Siegl, T. Lompe, and H. Moritz. “Two-Dimensional Homogeneous Fermi Gases”. In: *Physical Review Letters* 120.6 (2018), p. 060402. ISSN: 0031-9007. DOI: `10.1103/physrevlett.120.060402`. eprint: `1704.06315` (cit. on p. 36).

[83] I. Bloch, J. Dalibard, and W. Zwerger. “Many-body physics with ultracold gases”. English. In: *Reviews of Modern Physics* 80.3 (July 2008), pp. 885–964. DOI: `10.1103/revmodphys.80.885` (cit. on p. 36).

[84] L. Asteria. “Quantum Gas Magnifier for imaging of ultracold Atoms in highly tunable optical Lattices”. In: (2022). PhD - Sengstock Group (cit. on pp. 40, 72).

[85] L. Rayleigh. “XXV. On copying diffraction-gratings, and on some phenomena connected therewith”. In: *Philosophical Magazine Series 5* 11.67 (1881), pp. 196–205. ISSN: 1941-5982. DOI: `10.1080/14786448108626995` (cit. on p. 41).

[86] S. Nowak, C. Kurtsiefer, T. Pfau, and C. David. “High-order Talbot fringes for atomic matter waves”. In: *Opt. Lett.* 22.18 (1997), pp. 1430–1432. ISSN: 0146-9592. DOI: `10.1364/ol.22.001430` (cit. on p. 41).

[87] H. Miyake, G. A. Siviloglou, G. Puentes, D. E. Pritchard, W. Ketterle, and D. M. Weld. “Bragg Scattering as a Probe of Atomic Wave Functions and Quantum Phase Transitions in Optical Lattices”. In: *Phys. Rev. Lett.* 107.17 (2011), p. 175302. ISSN: 0031-9007. DOI: `10.1103/physrevlett.107.175302`. eprint: `1108.5408` (cit. on p. 41).

[88] P. Höllmer, J.-S. Bernier, C. Kollath, C. Baals, B. Santra, and H. Ott. “Talbot effect in the presence of interactions”. In: *Phys. Rev. A* 100.6 (2019), p. 063613. ISSN: 2469-9926. DOI: `10.1103/physreva.100.063613`. eprint: `1906.05615` (cit. on pp. 41, 54).

[89] V. B. Makhalov and A. V. Turlapov. "Quantum Talbot Effect for a Chain of Partially Correlated Bose—Einstein Condensates". In: *JETP Letters* 109.8 (2019), pp. 552–557. ISSN: 0021-3640. DOI: `10.1134/s0021364019080083`. eprint: `1907.02833` (cit. on pp. 41, 53).

[90] L. Deng, E. W. Hagley, J. Denschlag, J. E. Simsarian, M. Edwards, C. W. Clark, K. Helmerson, S. L. Rolston, and W. D. Phillips. "Temporal, Matter-Wave-Dispersion Talbot Effect". In: *Phys. Rev. Lett.* 83.26 (1999), pp. 5407–5411. ISSN: 0031-9007. DOI: `10.1103/physrevlett.83.5407` (cit. on p. 42).

[91] Y. Zhai, C. H. Carson, V. A. Henderson, P. F. Griffin, E. Riis, and A. S. Arnold. "Talbot-enhanced, maximum-visibility imaging of condensate interference". In: *Optica* 5.1 (2018), pp. 80–85. DOI: `10.1364/optica.5.000080`. eprint: `1707.08088` (cit. on p. 47).

[92] C. Li, T. Zhou, Y. Zhai, X. Yue, J. Xiang, S. Yang, W. Xiong, and X. Chen. "Optical Talbot carpet with atomic density gratings obtained by standing-wave manipulation". In: *Physical Review A* 95.3 (2017), p. 033821. ISSN: 2469-9926. DOI: `10.1103/physreva.95.033821` (cit. on p. 47).

[93] A. Trombettoni, A. Smerzi, and P. Sodano. "Observable signature of the Berezinskii–Kosterlitz–Thouless transition in a planar lattice of Bose–Einstein condensates". In: *New Journal of Physics* 7.1 (2005), p. 57. DOI: `10.1088/1367-2630/7/1/057`. eprint: `cond-mat/0404381` (cit. on pp. 49, 63, 81, 85).

[94] V. Schweikhard, S. Tung, and E. A. Cornell. "Vortex Proliferation in the Berezinskii-Kosterlitz-Thouless Regime on a Two-Dimensional Lattice of Bose-Einstein Condensates". In: *Phys. Rev. Lett.* 99.3 (2007), p. 030401. ISSN: 0031-9007. DOI: `10.1103/physrevlett.99.030401`. eprint: `0704.0289` (cit. on pp. 49, 62, 63, 77).

[95] K. Yamashita, K. Hanasaki, A. Ando, and T. Kinoshita. "Phase coherence of a Bose-Einstein condensate in an optical antidot lattice". In: *Phys. Rev. A* 100 (2019), p. 063611. DOI: `10.1103/physreva.100.063611` (cit. on pp. 49, 63).

[96] C.-L. Hung, X. Zhang, L.-C. Ha, S.-K. Tung, N. Gemelke, and C. Chin. "Extracting density–density correlations from in situ images of atomic quantum gases". In: *New Journal of Physics* 13.7 (2011), p. 075019. DOI: `10.1088/1367-2630/13/7/075019`. eprint: `1105.0030` (cit. on p. 49).

[97] R. Desbuquois, L. Chomaz, T. Yefsah, J. Ĺeonard, J. Beugnon, C. Weitenberg, and J. Dalibard. "Superfluid behaviour of a two-dimensional Bose gas". In: *Nature Physics* 8.9 (2012), pp. 645–648. ISSN: 17452481. DOI: `10.1038/nphys2378` (cit. on pp. 49, 62).

[98] S. W. Seo, J.-y. Choi, and Y.-i. Shin. "Scaling behavior of density fluctuations in an expanding quasi-two-dimensional degenerate Bose gas". In: *Phys. Rev. A* 89 (2014), p. 043606. DOI: `10.1103/physreva.89.043606` (cit. on pp. 49, 57).

[99] P. A. Murthy, I. Boettcher, L. Bayha, M. Holzmann, D. Kedar, M. Neidig, M. G. Ries, A. N. Wenz, G. Zürn, and S. Jochim. "Observation of the Berezinskii-Kosterlitz-Thouless Phase Transition in an Ultracold Fermi Gas". In: *Phys. Rev. Lett.* 115.1 (2015), p. 010401. ISSN:

0031-9007. DOI: `10.1103/physrevlett.115.010401`. eprint: `1505.02123` (cit. on pp. 49, 62, 78, 80).

[100] S. Sunami, V. P. Singh, D. Garrick, A. Beregi, A. J. Barker, K. Luksch, E. Bentine, L. Mathey, and C. J. Foot. "Observation of the Berezinskii-Kosterlitz-Thouless Transition in a Two-Dimensional Bose Gas via Matter-Wave Interferometry". In: *Phys. Rev. Lett.* 128.25 (2022), p. 250402. ISSN: 0031-9007. DOI: `10.1103/physrevlett.128.250402`. eprint: `2108.08840` (cit. on pp. 49, 62, 78, 80).

[101] S. Sunami, V. P. Singh, E. Rydow, A. Beregi, E. Chang, L. Mathey, and C. J. Foot. "Detecting Phase Coherence of 2D Bose Gases via Noise Correlations". In: *arXiv* (2024). DOI: `10.48550/arxiv.2406.03491`. eprint: `2406.03491` (cit. on pp. 49, 57, 62, 78).

[102] A. Smerzi, P. Sodano, and A. Trombettoni. "Finite-temperature renormalization group analysis of interaction effects in 2D lattices of Bose–Einstein condensates". In: *Journal of Physics B: Atomic, Molecular and Optical Physics* 37.7 (2004), S265. DOI: `10.1088/0953-4075/37/7/071` (cit. on pp. 54, 64).

[103] R. W. Gerchberg and W. O. Saxton. "A practical algorithm for the determination of phase from image and diffraction plane pictures". In: *Optik* (1972) (cit. on p. 54).

[104] P. A. Murthy and S. Jochim. "Direct imaging of the order parameter of an atomic superfluid using matterwave optics". In: *arXiv* (2019). DOI: `10.48550/arxiv.1911.10824`. eprint: `1911.10824` (cit. on pp. 57, 67).

[105] D. Caputo, D. Ballarini, G. Dagvadorj, C. S. Muñoz, M. D. Giorgi, L. Dominici, K. West, L. N. Pfeiffer, G. Gigli, F. P. Laussy, M. H. Szymanska, and D. Sanvitto. "Topological order and thermal equilibrium in polariton condensates". In: *Nature Materials* 17.2 (2018), pp. 145–151. ISSN: 14764660. DOI: `10.1038/nmat5039` (cit. on p. 57).

[106] J. J. Axelrod, J. T. Zhang, P. N. Petrov, R. M. Glaeser, and H. Müller. "Modern approaches to improving phase contrast electron microscopy". In: *Current Opinion in Structural Biology* 86 (2024), p. 102805. ISSN: 0959-440X. DOI: `10.1016/j.sbi.2024.102805` (cit. on p. 57).

[107] S. Dettmer, D. Hellweg, P. Ryytty, J. J. Arlt, W. Ertmer, K. Sengstock, D. S. Petrov, G. V. Shlyapnikov, H. Kreutzmann, L. Santos, and M. Lewenstein. "Observation of Phase Fluctuations in Elongated Bose-Einstein Condensates". In: *Phys. Rev. Lett.* 87.16 (2001), p. 160406. ISSN: 0031-9007. DOI: `10.1103/physrevlett.87.160406`. eprint: `cond-mat/0105525` (cit. on p. 57).

[108] A. Imambekov, I. E. Mazets, D. S. Petrov, V. Gritsev, S. Manz, S. Hofferberth, T. Schumm, E. Demler, and J. Schmiedmayer. "Density ripples in expanding low-dimensional gases as a probe of correlations". In: *Phys. Rev. A* 80.3 (2009), p. 033604. ISSN: 1050-2947. DOI: `10.1103/physreva.80.033604`. eprint: `0904.1723` (cit. on p. 57).

[109] V. P. Singh and L. Mathey. "Noise correlations of two-dimensional Bose gases". In: *Phys. Rev. A* 89.5 (2014), p. 053612. ISSN: 1050-2947. DOI: `10.1103/physreva.89.053612`. eprint: `1403.4233` (cit. on pp. 57, 62).

[110] C.-A. Chen, S. Khlebnikov, and C.-L. Hung. "Observation of Quasiparticle Pair Production and Quantum Entanglement in Atomic Quantum Gases Quenched to an Attractive Interaction". In: *Phys. Rev. Lett.* 127 (2021), p. 060404. DOI: `10.1103/physrevlett.127.060404` (cit. on p. 57).

[111] Z. Hadzibabic and J. Dalibard. "Two-dimensional Bose fluids: An atomic physics perspective". In: *Rivista del Nuovo Cimento* 34.6 (2011), pp. 389–434. ISSN: 0393697X. DOI: `10.1393/ncr/i2011-10066-3`. eprint: `0912.1490` (cit. on pp. 58, 78).

[112] R. Peierls. "Remarks on Transition Temperatures". In: 7 (1934). DOI: `10.1142/9789812795779\_0014` (cit. on p. 58).

[113] R. Peierls. "Quelques propriétés typiques des corps solides". In: *Annales de l'I. H. P.* 5.3 (1935) (cit. on p. 58).

[114] N. Bogolubov. "On some problems of the theory of superconductivity". In: *Physica* 26 (1960), S1–S16. ISSN: 0031-8914. DOI: `10.1016/0031-8914(60)90196-8` (cit. on p. 58).

[115] P. C. Hohenberg. "Existence of Long-Range Order in One and Two Dimensions". In: *Physical Review* 158.2 (1967), pp. 383–386. ISSN: 0031-899X. DOI: `10.1103/physrev.158.383` (cit. on p. 58).

[116] N. D. Mermin and H. Wagner. "Absence of Ferromagnetism or Antiferromagnetism in One- or Two-Dimensional Isotropic Heisenberg Models". In: *Physical Review Letters* 17.22 (1966), pp. 1133–1136. ISSN: 0031-9007. DOI: `10.1103/physrevlett.17.1133` (cit. on p. 58).

[117] D. R. Nelson and J. M. Kosterlitz. "Universal Jump in the Superfluid Density of Two-Dimensional Superfluids". In: *Phys. Rev. Lett.* 39 (1977), pp. 1201–1205. DOI: `10.1103/physrevlett.39.1201` (cit. on pp. 61, 78).

[118] D. J. Bishop and J. D. Reppy. "Study of the Superfluid Transition in Two-Dimensional He4 Films". In: *Physical Review Letters* 40.26 (1978), pp. 1727–1730. ISSN: 0031-9007. DOI: `10.1103/physrevlett.40.1727` (cit. on p. 61).

[119] J. D. Siegl. "Probing coherence propertiesof strongly interacting Bosegases". PhD thesis. 2018 (cit. on p. 62).

[120] N. Luick. "Local probing of the Berezinskii–Kosterlitz–Thouless transition in a two-dimensional Bose gas". Master's Thesis. 2014 (cit. on p. 62).

[121] S. Tung, G. Lamporesi, D. Lobser, L. Xia, and E. A. Cornell. "Observation of the Presuperfluid Regime in a Two-Dimensional Bose Gas". In: *Physical Review Letters* 105.23 (2010), p. 230408. ISSN: 0031-9007. DOI: `10.1103/physrevlett.105.230408`. eprint: `1009.2475` (cit. on p. 62).

[122] R. J. Fletcher, M. Robert-de-Saint-Vincent, J. Man, N. Navon, R. P. Smith, K. G. H. Viebahn, and Z. Hadzibabic. "Connecting Berezinskii-Kosterlitz-Thouless and BEC Phase Transitions by Tuning Interactions in a Trapped Gas". In: *Physical Review Letters* 114.25 (2015), p. 255302. ISSN: 0031-9007. DOI: `10.1103/physrevlett.114.255302`. eprint: `1501.02262` (cit. on p. 62).

[123] I. Boettcher and M. Holzmann. "Quasi-long-range order in trapped two-dimensional Bose gases". In: *Phys. Rev. A* 94 (2016), p. 011602. DOI: `10.1103/physreva.94.011602` (cit. on pp. 62, 78, 80, 82).

[124] J.-y. Choi, S. W. Seo, and Y.-i. Shin. "Observation of Thermally Activated Vortex Pairs in a Quasi-2D Bose Gas". In: *Physical Review Letters* 110.17 (2013), p. 175302. ISSN: 0031-9007. DOI: `10.1103/physrevlett.110.175302`. eprint: `1211.5649` (cit. on p. 62).

[125] W. Weimer, K. Morgener, V. P. Singh, J. Siegl, K. Hueck, N. Luick, L. Mathey, and H. Moritz. "Critical Velocity in the BEC-BCS Crossover". In: *Physical Review Letters* 114.9 (2015), p. 095301. ISSN: 0031-9007. DOI: `10.1103/physrevlett.114.095301`. eprint: `1408.5239` (cit. on p. 62).

[126] R. Gupta, J. DeLapp, G. G. Batrouni, G. C. Fox, C. F. Baillie, and J. Apostolakis. "Phase Transition in the 2D XY Model". In: *Phys. Rev. Lett.* 61 (1988), pp. 1996–1999. DOI: `10.1103/physrevlett.61.1996` (cit. on pp. 62, 77).

[127] S. T. Bramwell and P. C. W. Holdsworth. "Magnetization: A characteristic of the Kosterlitz-Thouless-Berezinskii transition". In: *Physical Review B* 49.13 (1994), pp. 8811–8814. ISSN: 1098-0121. DOI: `10.1103/physrevb.49.8811` (cit. on pp. 63, 81, 82).

[128] M. R. Beasley, J. E. Mooij, and T. P. Orlando. "Possibility of Vortex-Antivortex Pair Dissociation in Two-Dimensional Superconductors". In: *Physical Review Letters* 42.17 (1979), pp. 1165–1168. ISSN: 0031-9007. DOI: `10.1103/physrevlett.42.1165` (cit. on p. 63).

[129] D. J. Resnick, J. C. Garland, J. T. Boyd, S. Shoemaker, and R. S. Newrock. "Kosterlitz-Thouless Transition in Proximity-Coupled Superconducting Arrays". In: *Physical Review Letters* 47.21 (1981), pp. 1542–1545. ISSN: 0031-9007. DOI: `10.1103/physrevlett.47.1542` (cit. on p. 63).

[130] R. H. Leonard and C. A. Sackett. "Effect of trap anharmonicity on a free-oscillation atom interferometer". In: *Phys. Rev. A* 86.4 (2012), p. 043613. ISSN: 1050-2947. DOI: `10.1103/physreva.86.043613`. eprint: `1209.4127` (cit. on p. 64).

[131] C. Becker, S. Stellmer, P. Soltan-Panahi, S. Dörscher, M. Baumert, E.-M. Richter, J. Kronjäger, K. Bongs, and K. Sengstock. "Oscillations and interactions of dark and dark–bright solitons in Bose–Einstein condensates". In: *Nature Physics* 4.6 (2008), pp. 496–501. ISSN: 1745-2473. DOI: `10.1038/nphys962`. eprint: `0804.0544` (cit. on p. 69).

[132] E. P. Gross. "Structure of a quantized vortex in boson systems". In: *Il Nuovo Cimento (1955-1965)* 20.3 (1961), pp. 454–477. ISSN: 0029-6341. DOI: `10.1007/bf02731494` (cit. on p. 70).

[133] L. Pitaevskii. "Vortex Lines in an Imperfect Bose Gas". In: *Journal of Experimental and Theoretical Physics* 13 (1961) (cit. on p. 70).

[134] J. Schloss. *Split-Operator Method · Arcane Algorithm Archive*. 2018 (cit. on p. 70).

[135] R. Gati, B. Hemmerling, J. Fölling, M. Albiez, and M. K. Oberthaler. "Noise Thermometry with Two Weakly Coupled Bose-Einstein Condensates". In: *Phys. Rev. Lett.* 96.13 (2006), p. 130404. ISSN: 0031-9007. DOI: `10.1103/physrevlett.96.130404`. eprint: `cond-mat/0601392` (cit. on pp. 73, 76).

[136] L. Pitaevskii and S. Stringari. “Thermal vs Quantum Decoherence in Double Well Trapped Bose-Einstein Condensates”. In: *Phys. Rev. Lett.* 87 (2001), p. 180402. DOI: `10.1103/physrevlett.87.180402` (cit. on pp. 76, 77).

[137] P. B. Blakie and J. V. Porto. “Adiabatic loading of bosons into optical lattices”. In: *Phys. Rev. A* 69.1 (2004), p. 013603. ISSN: 1050-2947. DOI: `10.1103/physreva.69.013603`. eprint: `cond-mat/0307655` (cit. on p. 77).

[138] H. Weber and P. Minnhagen. “Monte Carlo determination of the critical temperature for the two-dimensional XY model”. In: *Phys. Rev. B* 37 (1988), pp. 5986–5989. DOI: `10.1103/physrevb.37.5986` (cit. on p. 80).

[139] G. Carleo, I. Cirac, K. Cranmer, L. Daudet, M. Schuld, N. Tishby, L. Vogt-Maranto, and L. Zdeborová. “Machine learning and the physical sciences”. In: *Rev. Mod. Phys.* 91 (2019), p. 045002. DOI: `10.1103/revmodphys.91.045002` (cit. on p. 83).

[140] M. Holten, L. Bayha, K. Subramanian, S. Brandstetter, C. Heintze, P. Lunt, P. M. Preiss, and S. Jochim. “Observation of Cooper pairs in a mesoscopic two-dimensional Fermi gas”. In: *Nature* 606.7913 (2022), pp. 287–291. ISSN: 14764687. DOI: `10.1038/s41586-022-04678-1` (cit. on p. 84).

[141] R. Bücker, A. Perrin, S. Manz, T. Betz, C. Koller, T. Plisson, J. Rottmann, T. Schumm, and J. Schmiedmayer. “Single-particle-sensitive imaging of freely propagating ultracold atoms”. In: *New Journal of Physics* 11.10 (2009), p. 103039. DOI: `10.1088/1367-2630/11/10/103039`. eprint: `0907.0674` (cit. on p. 84).

[142] A. Fuhrmanek, A. M. Lance, C. Tuchendler, P. Grangier, Y. R. P. Sortais, and A. Browaeys. “Imaging a single atom in a time-of-flight experiment”. In: *New Journal of Physics* 12.5 (2010), p. 053028. DOI: `10.1088/1367-2630/12/5/053028`. eprint: `1002.2311` (cit. on p. 84).

[143] C. J. Picken, R. Legaie, and J. D. Pritchard. “Single atom imaging with an sCMOS camera”. In: *Applied Physics Letters* 111.16 (2017), p. 164102. ISSN: 0003-6951. DOI: `10.1063/1.5003304`. eprint: `1709.00946` (cit. on p. 84).

[144] A. Bergschneider, V. M. Klinkhamer, J. H. Becher, R. Klemt, G. Zürn, P. M. Preiss, and S. Jochim. “Spin-resolved single-atom imaging of Li6 in free space”. In: *Physical Review A* 97.6 (2018), p. 063613. ISSN: 2469-9926. DOI: `10.1103/physreva.97.063613`. eprint: `1804.04871` (cit. on p. 84).

[145] N. Bidzinski. “Customized optical fiber inside an objective for a compact quantum gas setup”. Master’s Thesis. 2023 (cit. on p. 84).

[146] S. G. Söyler, M. Kiselev, N. V. Prokof’ev, and B. V. Svistunov. “Phase Diagram of the Commensurate Two-Dimensional Disordered Bose-Hubbard Model”. In: *Phys. Rev. Lett.* 107 (2011), p. 185301. DOI: `10.1103/physrevlett.107.185301` (cit. on p. 84).

[147] T. H. Barter, T.-H. Leung, M. Okano, M. Block, N. Y. Yao, and D. M. Stamper-Kurn. “Spatial coherence of a strongly interacting Bose gas in the trimerized kagome lattice”. In: *Phys. Rev. A* 101 (2020), p. 011601. DOI: `10.1103/physreva.101.011601` (cit. on p. 84).

[148] W. D. Roeck and F. Huveneers. “Stability and instability towards delocalization in many-body localization systems”. In: *Phys. Rev. B* 95 (2017), p. 155129. DOI: `10.1103/physrevb.95.155129` (cit. on p. 84).

[149] J. Struck, C. Ölschläger, R. L. Targat, P. Soltan-Panahi, A. Eckardt, M. Lewenstein, P. Windpassinger, and K. Sengstock. “Quantum simulation of frustrated classical magnetism in triangular optical lattices”. In: *Science* 333.6045 (2011), pp. 996–999. ISSN: 00368075. DOI: `10.1126/science.1207239`. eprint: `1103.5944` (cit. on p. 84).

[150] H. Ozawa, R. Yamamoto, and T. Fukuhara. “Observation of chiral-mode domains in a frustrated XY model on optical triangular lattices”. In: *Phys. Rev. Res.* 5 (2023), p. L042026. DOI: `10.1103/physrevresearch.5.l042026` (cit. on p. 84).

[151] H. P. Zahn, V. P. Singh, M. N. Kosch, L. Asteria, L. Freystatzky, K. Sengstock, L. Mathey, and C. Weitenberg. “Formation of Spontaneous Density-Wave Patterns in dc Driven Lattices”. In: *Phys. Rev. X* 12.2 (2022), p. 021014. DOI: `10.1103/physrevx.12.021014`. eprint: `2108.11917` (cit. on p. 84).

[152] D. A. Ikonnikov, S. A. Myslivets, M. N. Volochaev, V. G. Arkhipkin, and A. M. Vyunishev. “Two-dimensional Talbot effect of the optical vortices and their spatial evolution”. In: *Scientific Reports* 10.1 (2020), pp. 1–10. ISSN: 20452322. DOI: `10.1038/s41598-020-77418-y` (cit. on p. 84).

[153] J. B. Birdsong and N. I. Rummelt. “The Hexagonal Fast Fourier Transform”. In: *2016 IEEE International Conference on Image Processing (ICIP)* (2016), pp. 1809–1812. DOI: `10.1109/icip.2016.7532670` (cit. on pp. 85, 86).

[154] R. Mersereau. “The processing of hexagonally sampled two-dimensional signals”. In: *Proceedings of the IEEE* 67.6 (1979), pp. 930–949. ISSN: 0018-9219. DOI: `10.1109/proc.1979.11356` (cit. on p. 86).

[155] N. I. Rummelt. “Array Set Addressing: Enabling Efficient Hexagonally Sampledimage Processing”. PhD thesis. 2010 (cit. on p. 86).

Acknowledgements

Here I like to thank all people who made this thesis possible, took part in this journey, and supported me throughout the last years.

First of all, I would like to thank Christof for leading this project and allowing me to take part in it. You've been an excellent teacher, supervisor, and sparring partner in scientific discussion for the better part of my scientific development. Thank you for your input, your motivation, your many ideas, and the chance to develop my own. Thank you for your support.

I would like to thank Henning not only for agreeing to review my thesis but also for your part in sparking my interest in cold atoms. I remember vividly and fondly your lectures. Additionally, I thank you for your encouragement to organize the lunch talk events. Also, I would like to thank Klaus equally for his part in enabling the path to this thesis with lectures, supervision of my Bachelor and Master thesis, and numerous discussions on problems and ideas. Your group has been a scientific home to me for almost a decade now. I would like to thank Ludwig and Roman for being part of my committee and your excellent lectures.

A special thanks is owed to my PhD colleague Mathis. Spending most of the waking hours of the last years with you in the lab has been enlightening, joyful, demanding, frustrating, exciting, and it has always been a good time. Thank you for your trust, support, and lending me your memory when mine was elusive. I wouldn't have, couldn't have done it without you. Thank you for your friendship.

A big thanks goes out to all other former members of the Lithium team. Benno, Andi, Michael, you taught me so much during our common time in the team. Thank you for your tremendous initial work on this experiment. These results wouldn't have been possible without you. Niklas, thank you for all the vivid discussions, on physics and on every other topic. Organizing the group retreat with you was a great pleasure. Without your IT projects, analyzing wouldn't have been as much fun and thank you for this nice thesis layout. To all the Bachelor and Master students, thank you for your trust and your experimental work, Tobi, Nora, Jonathan, Marco, Mara, Tom, Julius, Richard, and Steven.

Furthermore, I would like to thank everybody in the Sengstock research group for creating a friendly, productive, and motivated scientific home. Special thanks to the BFM team for your close collaboration, Luca, Henrik, and Marcel, to Ortwin for support in optically demanding ideas, to Ellen for your daily help, and to Reinhard and Finn for keeping the whole institute running.

Yann and Jakob, thank you for your close friendship and discussing physics with you while climbing had a major motivating impact in the last years. Max, thank you for many helpful discussions.

Last but not least, I would like to thank my family and friends. Thank you for your support and diverting my thoughts away from work, now and then. A special thanks to my parents, your support through my whole life, your encouragement to pursue my interests, and well-placed portion of pressure enabled me to get this far.

There is one more person to whom I owe tremendous thanks. Jojo, my partner, my wife, my base. Thank you for holding me up through the tough times, especially looking back over the last weeks. Your support kept me pushing forward. You make every moment more joyful.